ROTORDYNAMIC AND EROSION STUDY OF BEARINGS IN ELECTRICAL SUBMERSIBLE PUMPS

A Dissertation

by

CHANGRUI BAI

Submitted to the Office of Graduate and Professional Studies of Texas A&M University
in partial fulfillment of the requirements for the degree of

DOCTOR OF PHILOSOPHY

Chair of Committee,	Gerald L. Morrison
Committee Members,	Alan Palazzolo
	Andrea Strzelec
	Robert Randall
Head of Department,	Andreas A. Polycarpou

May 2017

Major Subject: Mechanical Engineering

ABSTRACT

Electrical Submersible Pumps (ESPs) are widely used for oil production. Reliability studies of ESPs are important to increase their life span, thus improving profits. Experimental data of a 185-hour erosion on a WJE-1000 ESP has been analyzed. The eroded bearings are inspected in micron scale with a certain time interval. It shows that bearings and seals in the ESPs are the main factors causing vibrations and failure of the ESP systems. To better understand the rotordynamic behavior and material fatigue of the bearings/seals in ESPs, a vertical bearing/seal test rig is built. The test rig simulates the motion of rotating components in a WJE-1000 ESP and conducts multi-phase erosion experiments efficiently with water, air and sand. Experiments on plain journal bearings with different radial clearances, mass imbalances, and multi-phase flows are conducted using the bearing/seal test rig.

Computational Fluid Dynamics (CFD) simulations are performed to study the fluid zone in the journal bearings. A Fluid Structure Interaction (FSI) simulation based on Fluent and MATLAB is proposed. It predicts the transient motions of the rotor-bearing system, which provides essential information needed for the design of rotor-bearing systems. In addition, an optimized FSI simulation using pre-built bearing model and Timoshenko beam model is proposed to improve the time efficiency of the FSI simulation further.

This study provides an efficient way to study the bearings/seals in the field of rotordynamics and material, which is important for the reliability study of ESPs.

Meanwhile, the FSI simulations predict the transient behaviors of the rotor-bearing system, providing important reference for the design and modification of bearings/seals.

ACKNOWLEDGEMENTS

I would like to appreciate my committee chair, Dr. Gerald L. Morrison, who expertly guided me through my graduate study. Without his guidance and support this thesis would not have been possible. I also would like to thank my committee members, Dr. Alan Palazzolo, Dr. Andrea Strzelec, and Dr. Robert Randall for their guidance and support.

Thanks also go to my friends and colleagues at the Turbomachinery Lab and the department faculty and staff for making my time at Texas A&M University a great experience. My appreciation also extends to Shell, which funded my research.

Finally, thanks to my mother and father for their encouragement and to my girlfriend for her patience and love.

NOMENCLATURE

AC	Alternating Current
BEP	Best Efficiency Point
BHP	Break Horse Power
BPD	Barrels per Day
CFD	Computational Fluid Dynamics
DC	Direct Current
ESP	Electrical Submersible Pump
FEM	Finite Element Method
FSI	Fluid Structure Interaction
GPM	Gallons per Minute
H	Pump Head
HP	Horse Power
Hz	Hertz
UDF	User Defined Function
P&ID	Piping and Instrumentation Diagram
PID	Proportion -Integral-Derivative Controller
PSI	Pressure Square Inch
PSIG	Pressure Square Inch Gauge
RPM	Rotation per Minute
rpm	Rotation per Minute
VFD	Variable Frequency Drive

C_D	Drag Coefficient
F_D	Drag Force
F_B	Buoyancy Force
G_s	Gravity of Sand Particle
I_p	Moment of Momentum
M_f	Friction Moment.
N	Spin Speed
N_R	Power Loss of the Roller Bearing
Q	Flow Rate
S/s	Samples/Second
T	Torque
V	Velocity
mA	Milliampere
g	Gravity Acceleration Constant
t	Time
η	Efficiency
ρ	Density
v	Kinetic Viscosity
μ	Dynamic Viscosity
ε	Eccentricity Ratio

ω	Angular Velocity
Δp	Differential Pressure
θ	Rotation Angle

CONTRIBUTORS AND FUNDING SOURCES

Contributors

This work was supported by a dissertation committee consisting of Professor Gerald L. Morrison [advisor], Alan Palazzolo, Andrea Strzelec of the Department of Mechanical Engineering and Professor Robert Randall of the Department of Ocean Engineering.

The erosion experiments in section 2.1 were conducted by Dezhi(Daniel) Zheng and Yi Chen. The design of the test rig in section 2.2 was implemented in collaboration with Andrew William Johnson.

All other work conducted for the dissertation was completed by the student independently.

Funding Sources

This work was made possible in part by Shell oil company.

Its contents are solely the responsibility of the authors and do not necessarily represent the official views of the Shell oil company.

TABLE OF CONTENTS

Page

LIST OF FIGURES

Page

LIST OF TABLES

Page

1. INTRODUCTION

1.1 Electrical Submersible Pump

More than 60% of producing oil wells require assisted lift technologies to pump the oil to the surface and maintain production [1]. The lift systems include sucker rod pumping (beam pumping), gas lift, electrical submersible pumping, hydraulic piston pumping, hydraulic jet pumping, plunger piston pumping, hydraulic jet pumping and plunger (free-piston) lift [2]. The Electrical Submersible Pump (ESP) is a highly efficient and reliable artificial-lift method for lifting production fluids from wellbores [3]. The first ESP was invented and developed by a Russian named Armais Arutunoff in the 1910s. The first ESP installation was successfully operated in the El Dorado field in Kansas in 1926. So far, approximately 15% to 20% of wells throughout the world utilize ESPs.

ESPs consist of multiple centrifugal pump stages mounted in series operating in a vertical position. ESPs impart kinetic energy to the fluid by centrifugal force and then convert that to potential energy in the form of pressure. As the typical ESP system shown in Figure 1-1, the downhole components of an ESP system include centrifugal pump, motor, gas handling equipment, seals, downhole sensors, and power cables. The surface components of an ESP system include motor speed controller and drive, electrical supply system, pipes, and containers [4].

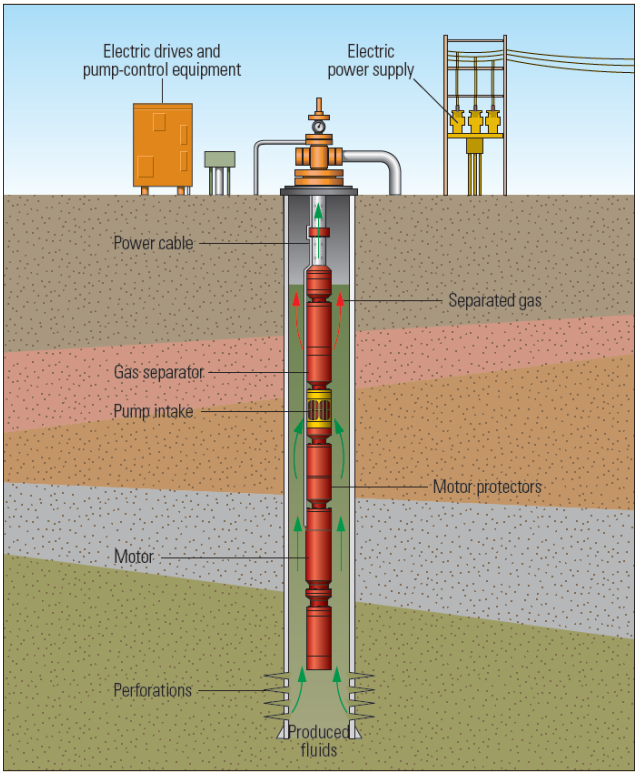

Figure 1-1 A typical ESP system [4].

The motor of the ESP system is mounted on the bottom, so it is submerged in fluid to enhance cooling. The thrust bearing that carries the axial thrust developed by the pump is mounted between the pump intake and the motor. A seal section is also located there to isolate and protect the motor from well fluids and equalizes the pressure in the wellbore with the pressure inside the motor. A gas separator is generally installed at the intake of the pump to separate the gas from the well fluid before it enters the pump. Downhole sensors are installed to acquire real-time operation data including pump intake and discharge pressure, temperature, vibration, and current leakage rate. Power is supplied through a specially designed three-phase electric cable from the surface. The speed of the downhole motor is controlled by a variable speed drive (VSD) on the surface. The VSD

analyzes the data from the downhole sensors and balances the pump efficiency and production rate through controlling the speed of the motor [3].

ESPs are widely used because of the high liquid volumes, relatively high energy efficiency, and low-maintenance requirements. It requires a smaller surface footprint than that of other artificial lift systems. Meanwhile, it also has some disadvantages. The gas, sand or other solids in well fluids increase the erosion process of the equipment dramatically, which decreases the reliability resulting in system failure. The repair or replacement of an ESP costs of money and time [5].

1.1.1 ESP Classification

Generally, centrifugal pumps are classified into radial, axial, and mixed flow groups. The classification based on the direction of the impeller's discharge. Radial flow and mixed flow pumps are primarily used in ESP systems. The radial flow centrifugal pumps are used for smaller capacity pumps producing less than 3000 BPD liquid. The mixed flow pumps are used at higher flow rates [5]. One stage of a radial flow pump and a mixed flow pump are shown in Figure 1-2 respectively [5]. They both consist of an impeller and a diffuser.

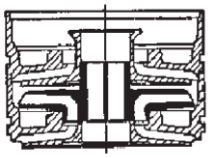

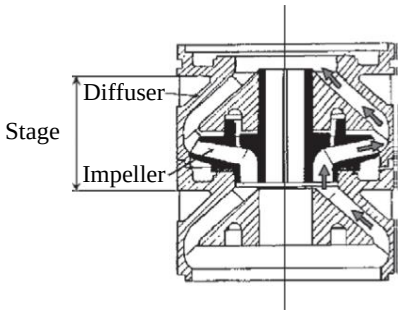

(a) Radial Flow Stage (b) Mixed Flow Stage

Figure 1-2 Single stage of two types of centrifugal pumps [5].

The shaft is driven by a motor while the impeller is fixed to the shaft and rotates along with the shaft. The diffuser is a stationary part. The arrows in the mixed flow stage show that the flow from the previous stage firstly passes through the impeller and then enters the diffuser. The liquid is accelerated by vanes of impeller where kinetic energy is transferred from the impeller to the liquid. When the liquid enters diffuser, the kinetic energy is converted to pressure energy, and the velocity of the liquid is decreased. Thus, the pressure in the outlet of diffuser is higher than that at the inlet of the impeller.

1.1.2 ESP Performance

The ESP transfers mechanical energy of the impeller to the kinetic energy of the fluid. The head of an ESP system is defined as the pressure produced by the pump divided by the fluid density. It is a key indicator for a pump's performance, and it is a constant for a certain pump at a certain liquid rate. Theoretically, the head is related to the liquid rate inversely and related to the Euler Equation linearly [6]. However, due to the hydraulic losses, shock losses, leakage losses, and mechanical losses, the real head developed by a

pump is usually less than the theoretical one. A real pump performance curve is shown in Figure 1-3 [5].

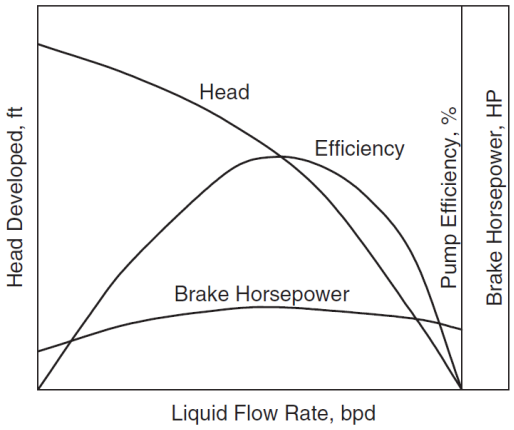

Figure 1-3 Typical pump performance curve [5].

In Figure 1-3:

Brake Horsepower: The total power required to drive the pump.

$$\text{Efficiency}=\frac{\text{Hydraulic Power}}{\text{Brake Horsepower}}.$$

Hydraulic Power: The power exerted by the pump to lift a given amount of liquid against the operating head. It is calculated by Equation (1.1).

$$\text{Hydraulic Power} = 7.368\times10^{-6} Hq\gamma \tag{1.1}$$

where:

H is the head generated by the pump (ft);

q is the pumping rate (bpd);

γ is the specific gravity of the fluid.

The running point with the maximum efficiency is called the Best Efficiency Point (BEP), which is the point pumps usually run nearby.

1.2 Erosion of ESPs and Bearings

The ESP is a high-speed rotating device with its stationary and rotating parts lubricated by the fluid pumped (e.g. Oil). The rotating parts of ESP can be easily damaged by the solid particles (e.g. sands) in oil well fluids. The particles may enter the clearances of different kinds of bearings (radial and axial) in an ESP, and cause abrasion or erosion of the bearings or seals. The abrasion and erosion dramatically affect the rotordynamic behavior of the bearings. In addition, the metal loss of the ESP components leads to mass imbalances, which increase the imbalance forces resulting in increased vibrations. These two main effects may lead to the failure of the ESP. The damages caused by the abrasive material are mainly classified into two types:

1) Abrasion: The mechanical rubbing wear between two surfaces accentuated by the presence of abrasive materials. It is similar to sanding.
2) Erosion: A metal surface is hit by the abrasive materials causing metal loss. It is similar to sand blasting.

Although solids other than sand may cause abrasion in centrifugal pumps, most of the abrasion/erosion problems are caused by the sand along with well liquids. The main component of sand is quartz. Based on the Mohs scale of mineral hardness, the hardness of quartz is larger than most of common metals. Thus, the base material of the ESP should be selected carefully. Coatings with harder materials are usually used in ESP to reduce the damage of abrasive materials. The extent of wear is related to the size and roughness of sand particles as well as the velocity of the liquid. Large and rough sands can cause more serious wear than the small and smooth ones. And since kinetic energy is proportional to

square of flow velocity, sand in the flow with higher spin speeds result in more serious wear. Sand concentration is also a key factor of erosion progresses in ESP. The usual classification of sand production is presented in Table 1-1 [5].

Table 1-1 Classification of sand production

Concentration (mg/liter)	Definition
Less than 10	Light
11–50	Moderate
51–200	Heavy
More than 200	Severe

Possible wear positions in ESP can be classified as:

1) Pump stages (impellers, and diffusers).

2) Bearings and seals.

Besides the impellers and diffusers in an ESP, bearings are also affected by sand erosion. Typically, ESP uses plain journal bearings to carry radial loads. The plain journal bearing consists of two pieces: sleeve (journal) and bushing (bearing). The sleeve is a rotating piece spinning with the rotor, while the bushing is a stationary part. There is a clearance between sleeve and bushing to let the lubricant (usually the liquid pumped by the ESP) to flow in. Although the clearance seems small, it is still large enough to let some sand particles pass through. Erosion of bearings causes growth of the clearance. This decreases the flow rate of ESP firstly, since more fluid can flow back through the clearance to the pump inlet. It also decreases the load capacity of the journal bearing, and leads the shaft rotating eccentrically, which in turn further accelerates the erosion. Moreover, the increase of bearing clearances also decreased the rotordynamic parameters of stiffness and

damping ratio. This results in increased vibration, which can destroy other pump components, such as seals, the motor, and separators.

Several studies of the pump performance under 2-phase flow (water and air) using flow visualization have been conducted [7-10]. The erosion of pump components is altered when air and solid particles are present. The air also affects the performance and dynamic behavior of the pump. This can result in increased wear causing accelerated weight loss, and deformation of the shaft, which may lead to failure of the entire system. Thus, many articles have focused on the erosion of the pump [11-14]. Among all the components in ESP, the hydrodynamic plain journal bearings, which are used to support the rotating components, play an important role in affecting the dynamic behavior as well as the stability of the system. Gertzos et al. simulated the wear of a plain journal bearing and presented a graphical detection method to identify the wear depth associated with the measured dynamic bearing characteristics [15]. Adams et al. provided some parameters which can help to decide of the proper abrasive resistant trim for an ESP [16]. The parameters would allow a more expeditious selection of replacement equipment. Ligterink and De Gee investigated the measurement of wear in radial journal bearings [17]. Papadopoulos et al. presented an identification method for the bearing radial clearances using response measurements of the rotor at a certain point [18]. Wang et al. analyzed the nonlinear dynamics of a rub-impact rotor system supported by oil film bearings [19]. The analysis revealed the complex dynamic behavior comprising periodic, multi-periodic, chaotic, and quasi-periodic response.

1.3 Rotordynamic Analysis of ESP

Rotor dynamics is a specialized branch of engineering concerned with the dynamic behavior of rotating structures. It studies the lateral and torsional vibrations of rotating shafts with the objective of predicting the rotor vibrations and containing the vibration level under an acceptable limit [20]. A rotor-dynamic system, such as the ESP system, mainly consists of a shaft with rotating components (e.g. impellers), bearings, and seals. The shaft is used to support the blades, impellers, armatures. And in turn it is supported by bearings. It is typically made of some type of high strength steel alloy, and it usually has a long and thin geometry. The spin speed of an ESP is high to maximize the power output. The bearings in ESP are usually hydrodynamic fluid film bearings, and characterized by stiffness and damping terms. The seals prevent leakage of the liquids pumped between stages.

The basic equation of motion for an axially symmetric rotor rotating at a constant spin speed Ω is:

$$\mathbf{M}\ddot{\mathbf{q}}(t) + (\mathbf{C} + \mathbf{G})\dot{\mathbf{q}}(t) + \mathbf{K}\mathbf{q}(t) = \mathbf{f}(t) \tag{1.2}$$

where:

M is the symmetric mass matrix;

C is the symmetric damping matrix;

G is the skew-symmetric gyroscopic matrix;

K is the symmetric bearing or seal stiffness matrix;

q is the generalized coordinates of the rotor in inertial coordinates;

f is the generalized force.

The gyroscopic matrix **G** is proportional to the spin speed Ω. The off-diagonal terms of stiffness, damping, and mass are called cross-coupled stiffness, cross-coupled damping, and cross-coupled mass respectively. When there is a cross-coupled stiffness, a deflection will cause two reaction forces, one of them is opposite to the load force, and the other one is perpendicular to the load force. The perpendicular force causes whirling. Whirling refers to the movement of the center of mass of the deflected rotor in a plane perpendicular to the bearing axis. And depending on the positive or negative cross-coupled stiffness, the whirling is classified as positive or negative whirl. A simple rotor-bearing system is shown in Figure 1-4 [21]:

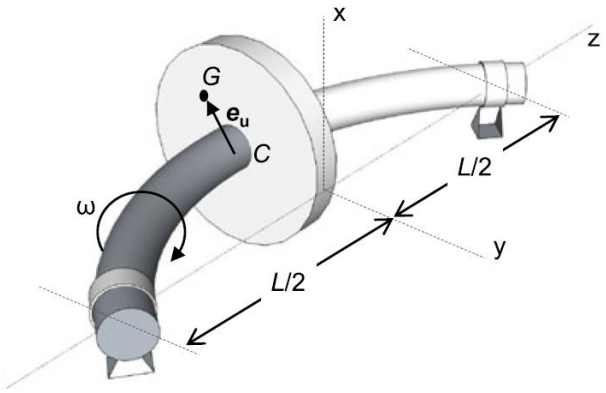

Figure 1-4 A simple rotor-bearing system [21].

In Figure 1-4, a rotor is support by two bearings at both ends, and an eccentric disk is mounted in the middle. The rotor is bent due to the imbalance forces of the disk and it rotates along its center line in axial direction. Meanwhile, the rotor-disk system whirls in a plane perpendicular to the bearing axis. When the direction of whirl is same as the direction of rotation, it is called positive whirl. Otherwise, the whirl is called negative whirl.

Due to the gyroscopic effects and the variable hydrodynamic conditions in fluid bearings, the parameters in the equation of a rotor-bearing system depend on the spin speed of the system. Setting the forcing item to be zero in Equation (1.2) presents the natural frequencies and mode shapes of the system respectively. When the natural frequency and the spin speed are equal at a certain spin speed, the spin speed is called critical speed. A resonant happens at the critical speed and usually a 15% safety margin is used in industry to avoid the critical speed points. A Campbell diagram is usually used to identify the critical speeds of a rotor-bearing system. An example of Campbell diagram in shown in Figure 1-5.

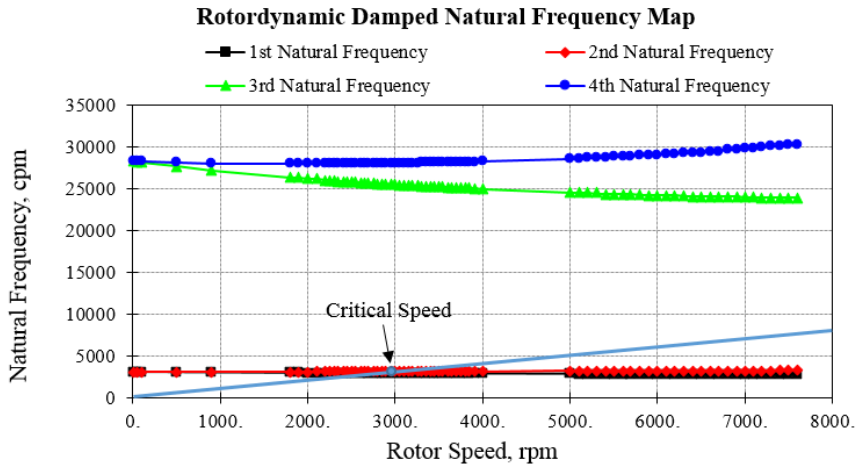

Figure 1-5 Example of a Campbell diagram.

In Figure 1-5, the x axis is the rotor speed while the y axis is the natural frequency related to the certain spin speed. Then, a straight line ($y = x$) is drawn, and its points of intersection with the lines of natural frequencies show the critical speed points.

Rankine performed the first analysis of a spinning shaft in 1869 [21]. Although his model was not adequate and predicted that supercritical speeds could not be attained, he

added the word whirling to the rotor dynamics vocabulary. Dunkerley found, because of numerous measurements, the first critical speed can be calculated, even for complicated cases [22]. Then, Jeffcott proposed the first recorded fundamental theory of rotor dynamics in 1919 [23]. Now, a flexible shaft of negligible mass with a rigid disk at the middle is called a Jeffcott rotor as shown in Figure 1-4. In 1924, Stodola published a book where he showed that the supercritical solutions were stabilized by Coriolis accelerations, which eventually produces gyroscopic effects [24].

As the rotational speed increases above the first critical speed, the large amount of kinetic energy stored in the rigid-body rotational mode of a high-speed rotor is available to fuel a wide variety of possible self-excited vibration mechanisms [25]. Newkirk and Taylor named the oil whip, which is used to describe an instability caused by the nonlinear action of the oil in a journal bearing [26]. Other instabilities due to the cross-coupling stiffness in bearings and seals were also discovered. Hori investigated the pressure forces due to oil films in bearings and explained the fundamental characteristics of oil whip [27]. Then, the nonlinear resonances at subharmonic frequencies (1/2X, 1/3X of harmonic frequency, etc.) occurs as rotors became lighter and rotational speeds became higher. Tondl researched the nonlinear resonances due to oil films in journal bearings [28]. Ehrich found that squeezed-film dampers induced subharmonic resonances in an aircraft gas turbine [29]. Since the fluid-film seems like the main reasons for the subharmonic vibrations, studies were focused on the rotor dynamic behaviors of fluid-film bearings. Tiwari et al. and Someya studied the dynamic parameters of fluid film bearings respectively [30-31]. Besides fluid-film bearings, seals in rotor-bearing system also have

the similar effect of bearings. Childs analyzed the rotordynamic coefficients of turbulent annular seals with different, directionally-homogeneous surface-roughness treatment for rotor and stator elements in 1985 [32-33].

Different analysis tools were developed to analyze the rotordynamic behaviors, Stodola studied the simple continuous rotor-bearing model corresponding to an Euler beam model [26]. Eshleman derived more general equations of motion considering the effects of rotary inertia, shear deformation and gyroscopic moment in 1969 [34]. Then the commonly used Transfer Matrix Method (TMM) was derived by Prohl Myklestad [35-36]. The TMM method has developed rapidly since the 1960s. Along with the development of finite element methods, it is also widely used in the analysis of rotordynamics. Taplak et al. evaluated the gas turbine rotor dynamic analysis using finite element method [37].

1.4 Fluid Structure Interaction Simulation

Fluid Structure Interaction (FSI) is the interaction of a movable or deformable structure with an internal or surrounding fluid flow [38]. FSI is useful in scientific and engineering fields including the sedimentation, aerodynamics, complex flows in irregular domains, bio-mechanics, fluid dynamics, electro-hydrodynamics, and rotordynamics [39-40]. But the comprehensive study of FSI problems remains a challenge due to their strong nonlinearity and multidisciplinary nature [41].

The procedures to solve FSI problems can be broadly classified into two approaches: (1) monolithic approach, and (2) partitioned approach. It is based on the way they treat the system models. In addition, based on the treatment of meshes, there is

another classification method for FSI solution procedures: (1) conforming mesh methods, and (2) non-conforming mesh methods. The classification of FSI solution procedures is shown in the figure below.

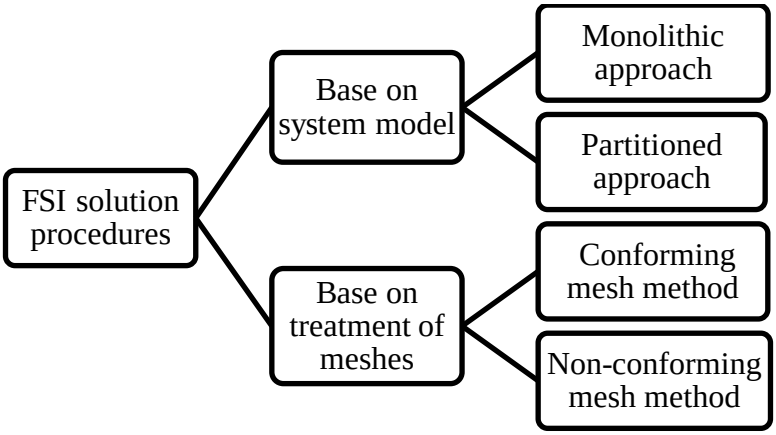

Figure 1-6 Classification of FSI solution procedures.

The monolithic approach combines the fluid and structure dynamics into a same mathematical framework, and forms a single system equation. Then the equations of fluid and structure dynamics can be solved simultaneously [42]. Although the monolithic approach can potentially achieve better accuracy for a multidisciplinary problem, it requires more resources and expertise to develop. On the contrary, the partitioned approach treats the fluid and structure as two separated computational fields which can be solved separately with their own mesh and algorithm. In this way, the existing methods can be used to solve the fluid and structure problems separately. But in this approach, the interface location that divides the fluid and the structure domains is not known as a priori and usually changes in real time. Thus, the partitioned approach requires the tracking of the new interface location and its related quantities, which can be cumbersome and error-prone [43].

The conforming mesh method treats the interfaces as boundary conditions. It requires meshes conform to the interface because the interface location is treated as part of the solution. Re-meshing is then needed as the solution is advanced. On the contrary, the non-conforming mesh methods treat the boundary location and the related interface conditions as constraints imposed on the model equations. Thus, the fluid and solid equations can be conveniently solved independently from each other with their respective grids, and re-meshing is not necessary [44].

With the advance in computer technology, more and more researchers are focusing on FSI simulations. Morand and Ohayon summarized numerous numerical methods of modeling linear vibrations of elastic structures coupled with internal fluids [45]. Shyy, and Wei et al. presented several computational methods for general moving boundary problems in fluid dynamics for FSI applications [45]. Based on the partitioned approach, Khonsari and Wang conducted the thermo-elasto-hydro-dynamic (TEHD) analysis of journal bearings using ANSYS [46]. Meruane and Pascual identified the dynamic coefficients of rigid plain bearings using CFD and partitioned FSI method [47]. Due to the advantages of the partitioned approach of FSI, the combination of existing mature algorithms as well as commercial codes in the FSI approach is relative easy. FSI approach using ANSYS Fluent and MATLAB is proposed and presented in the following sections.

1.5 Contributions

Previous three-phase erosion experiments on a WJE-1000 ESP system show that subharmonic vibrations occurred and finally dominated the shaft motion after a 185 hour of erosion. The bearings and seals in the ESP experienced the worst erosion. The

clearances of bearings were increased and the fatigue of materials was also shown on the surface of the bearings (e.g. heat checking). It shows that the erosion of the bearings and seals in the ESP are the main factors to cause vibrations and even failure of ESP systems. Since erosion experiments on one ESP system is expensive and takes several months, this study has two objectives: (1) Conduct the experiments on bearings and seals efficiently. (2) Study the rotordynamic behaviors of bearings/seals using numerical simulation, which can provide reference for the design of bearings/seals, and ESP systems. The main contributions of this study are as follows:

1) Built a vertical bearing/seal test rig to research the rotordynamic behaviors, and material fatigue of bearings/seals in ESPs. The test rig has the capacity to simulate the motions of rotating components in an ESP and conduct multi-phase (water, air and sand) erosion experiments efficiently.
2) Conducted multi-phase experiments on plain journal bearings and analyzed the experimental data.
3) Proposed a FSI simulation method based on Fluent and MATLAB to predict the transient motion of the vertical rotor-bearing system.
4) Proposed an optimized FSI simulation method based on CFD quasi-steady simulation and Timoshenko beam model, which could conduct the FSI simulation efficiently.

2. EXPERIMENT CONFIGURATION

Since the erosion experimental result of a WJE-100 ESP system is the direct motivation of this research, the experiments are introduced and the experimental data is analyzed in this chapter. Then, the mechanical and data acquisition system design of a vertical bearing/seal test rig is presented.

2.1 Erosion of a WJE-1000 ESP

A mixed flow WJE-1000 ESP was subjected to a 185 hours of erosion test. The ESP was custom-made for the laboratory environment and has three stages due to space and power limitation in the laboratory. An initial 117-hour two-phase test with water and sand was followed by a 68-hour three-phase test with water, sand and air.

In the first 117-hour test, a 2 gram/liter concentration ratio of 100 mesh hydraulic fracture sand was added into the water. In the following 68 hours, the erosion test was conducted with a 15% gas volume fraction with water, sand, and air. The sand was discarded after passing one time through the pump. The pump was operated at its Best Efficiency Point (BEP) at 3600 RPM.

2.1.1 Experimental Facilities

A facility to perform erosion studies is shown in Figure 2-1 and Table 2-1. The ESP is mounted vertically and driven by a motor from the top. The liquid is pumped from the bottom. Sands are loaded into a hopper and an auger is used to convey them into the slurry loop, where the liquid is feed by a centrifugal pump. Five percent of the liquid and all the sand is conveyed by the slurry loop. A Coriolis flow meter is used in the slurry loop

to measure the amount of sand and water entering the pump. The information from the Coriolis flow meter is the feedback signal used to control the sand concentration. The speed of the auger is adjusted to keep the sand concentration at 2 grams/liter. The other 95% of the water passes through another pump and the flow rate is metered by an orifice flow meter. The water is recirculated but the used sand is separated by a hydro cyclone separator system. In this way, the sands only pass through the ESP system once, which is consist with the real operating conditions in wells.

The water loop and slurry loop are combined and provide an inlet pressure of 40 psig for the ESP, which exceeds the minimum pressure required to prevent cavitation. The flow coming out from the ESP enters a hydro cyclone separator system, where the sand is removed and discarded.

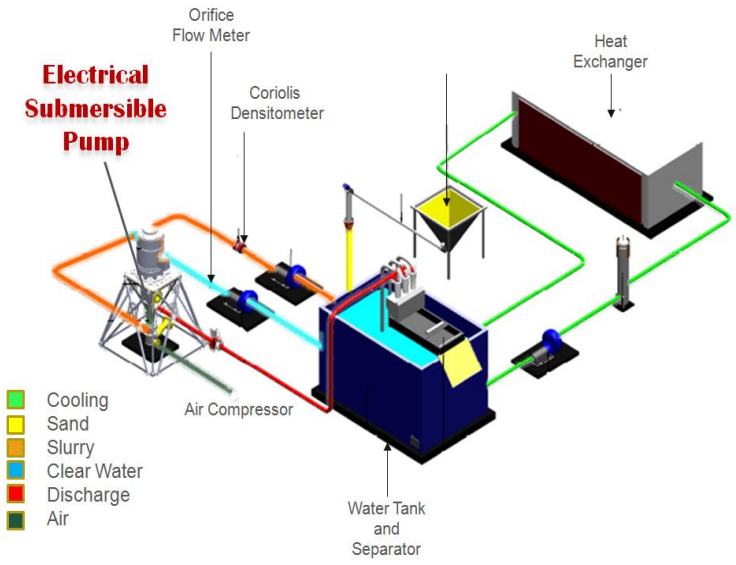

Figure 2-1 Experimental setup diagram

Table 2-1 Main components involved in the system

No.	Component	No.	Component
1.	ESP	10.	Air Control Valve
2.	ESP Drive Motor	11.	Discharge Gate Valve
3.	Derrick	12.	Air Gate Valve
4.	Feed Pump	13.	Coriolis Flow Meter
5.	Slurry Pump	14.	Orifice Flow Meter
6.	Cooling Pump	15.	Turbine Flow Meter
7.	Water Tank	16.	Sand Hopper
8.	Separator	17.	Sand Auger
9.	Discharge Pinch Valve	18.	Heat Exchanger

2.1.2 Experimental Conditions

The pump was eroded for 185 hours. This includes a 117-hour two-phase (water and sand) test and a followed 68-hour three-phase (water, sand and air) test. The typical concentration found in oil wells range from 10 mg/liter (light) to more than 200 mg/liter (severe) [5]. Since the purpose of this test is to find the failure modes, the sand concentration is set at 2g/liter to accelerate the erosion process. Details of the experimental conditions are shown in Table 2-2 and Table 2-3 respectively.

Table 2-2 Experimental conditions of the 117-hour 2-phase test

Condition	Value	Unit
Rotor spin speed	3600	RPM
BEP flow rate	1100	GPM
Sand size	100	Mesh
Condition	Value	Unit
Sand concentration	2	Grams/Liter

Table 2-3 Experimental conditions of the 68-hour 3-phase test

Condition	Value	Unit
Rotor spin speed	3600	RPM
BEP flow rate	850	GPM
Sand size	100	Mesh
Sand concentration	2	Grams/Liter
Gas volume fraction(GVF)	15%	--

The vibration of the ESP is monitored by 5 pairs of proximity probes which are mounted along the pump. The two proximity probes in each pair are mounted orthogonally in the same horizontal plane. Figure 2-2 shows the numbers, positions, and photograph of the proximity probes. Three pairs of them are monitoring the shaft just below journal bearings (noted as shaft 1, 2, and 3). The other two pairs are monitoring the labyrinth seals at the impellers' inlet (noted as impeller 2, and 3). Due to the sand eroding, the proximity probes were not present when sand was used.

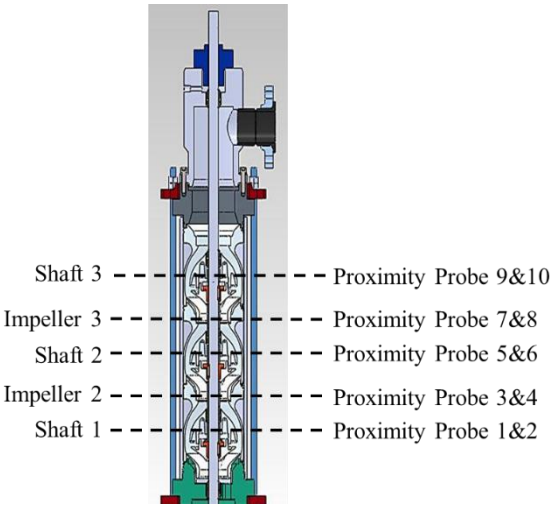

Figure 2-2 Proximity probe positions and numbers

2.1.3 Results and Analysis

2.1.3.1 Clearances of the bearings

The pump was disassembled at 8, 24, 56, 117 and 185 hours respectively. Figure 2-3 shows the bearing clearance changes after 0, 56, 117 and 185 hours of erosion. The figure includes the outside diameter (OD) and inside diameter (ID) of journals and bushings respectively. The net diametrical clearance of the bearings is also shown. The cross-section of the pump shows the locations of bearings.

The diameter of pump shaft is 1.5 inches, and the bearing wear decreases from the pump inlet (bottom of the pump) to the pump outlet. After the 117-hour two-phase test, air was added and the inlet GVF is maintained at 15%. Then, the erosion rate of the bearings increased as shown in Figure 2-3. There are two reasons of this phenomenon. Firstly, as the clearance increases, the load capacity and stiffness of the bearing decrease. In addition, the erosion of other components (impellers and diffusers) in the pump induced

more mass imbalance, which increased the loads on the bearings. These two factors caused an increase in vibration. Secondly, when air is introduced into the clearance of bearing, the lubricant film is broken which leads to higher possibilities of surface contacts. At the end, the maximum diametrical clearance is 0.080 inches (80 mils).

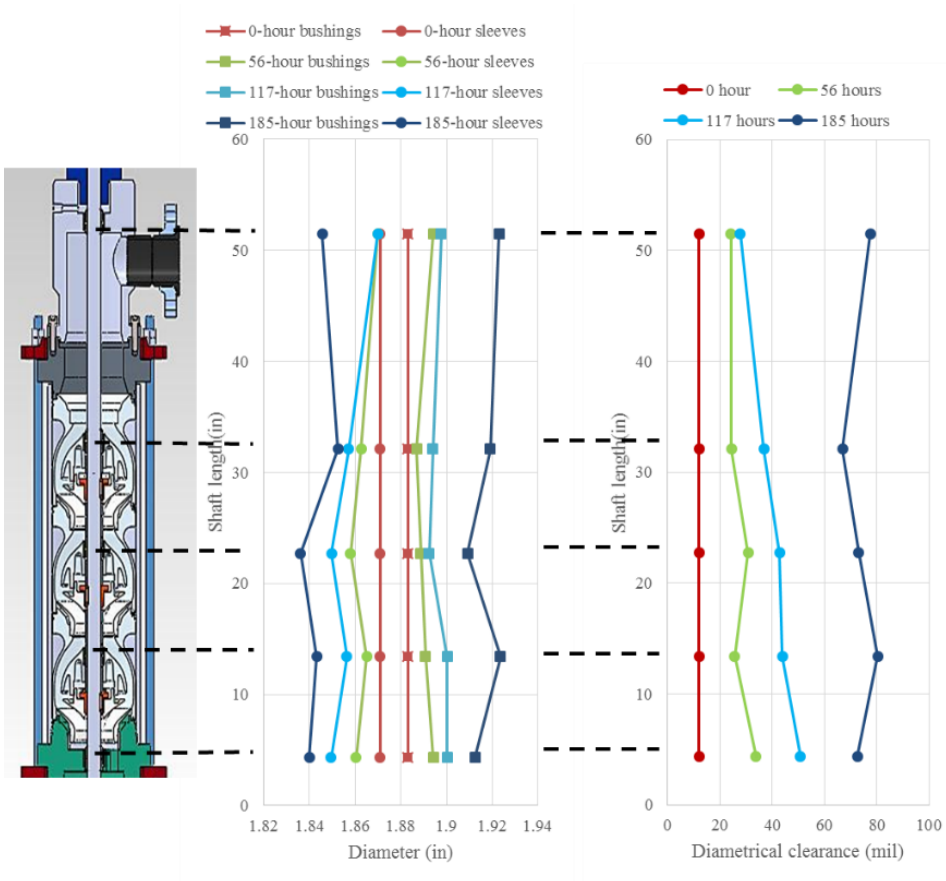

Figure 2-3 Bearing clearance changes due to erosion

2.1.3.2 Microscopic inspection

A microscopic inspection was conducted after 185 hours of erosion. The microscopic pictures of journal surfaces are shown in Figure 2-4.

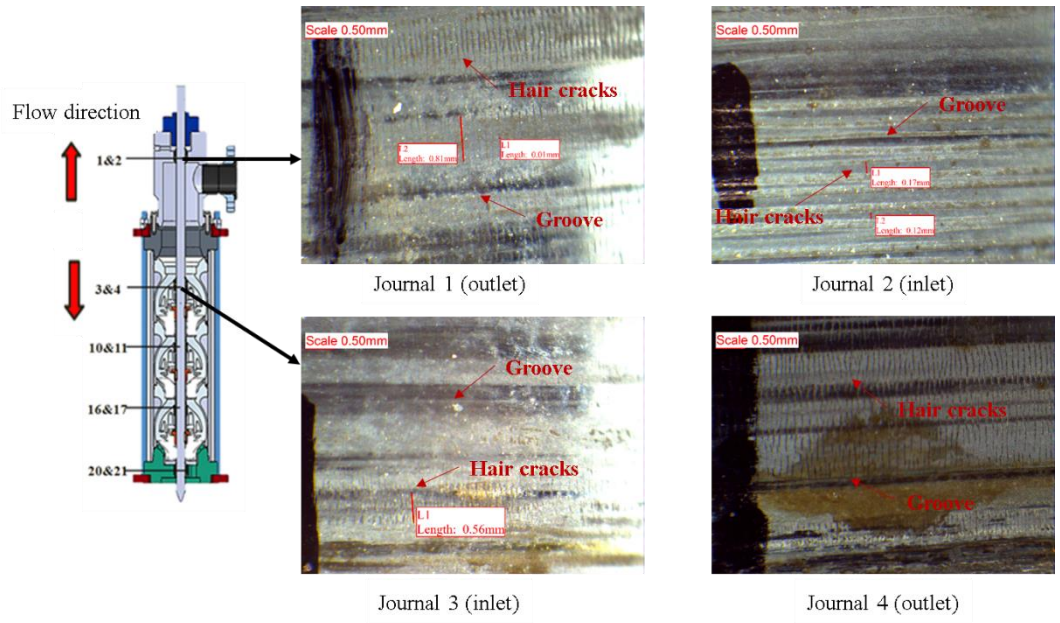

(a) Microscopic pictures of bearing 1&2, and 3&4

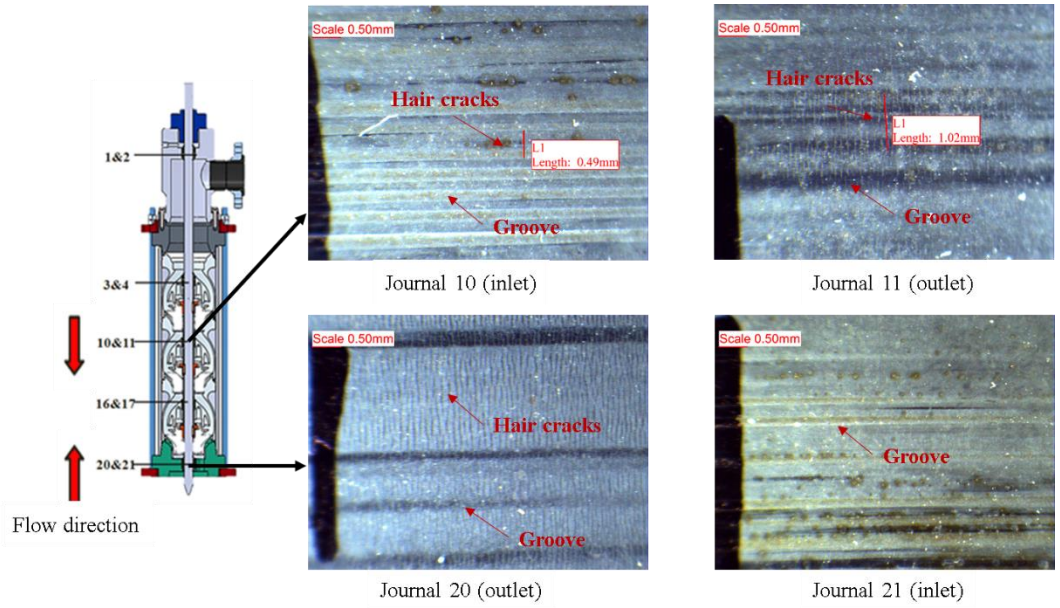

(b) Microscopic pictures of bearing 10&11, and 20&21

Figure 2-4 Microscopic pictures of journal surfaces after 185 hours

The eight images are the surface of four different journals at different positions of the pump. Two figures are shown for each position. One shows the surface at the inlet of the flow, the other one shows the surface at the outlet of the flow. The rotation of the shaft grabs the sand and drags it around the bearing. This is evidenced by the circular grooves in the journal surface. By the time the sand exits the bearing clearance, the sand size has been reduced by the crushing resulting in polishing the journal surface. Some cracks are found on the surface near the outlet of the flow. It is hypothesized that these cracks are caused by thermal stress occurring when the journal surfaces are polished by sands. The heating expended the surfaces, while the inner regions remain cool due to the low thermal conductivity of the tungsten carbide.

2.1.3.3 Operating orbit

The operating orbits from 0 to 185 hours of pump components are presented in Figure 2-5. In the figure, the operating orbit of impeller 2 has two spikes since flat spots were machined onto it to facilitate rotor angle measurement. The original radial clearances of bearings in the ESP is 6 mils. At the beginning (0 hour), the diameter of all the orbits are small and below 10 mils. As the erosion progresses, the orbits become larger. The orbits shape varies at difference locations. At the end of the 117-hour two-phase experiment, the diameter of orbits is around 20 mils. While, after 185 hours, the diameter of some orbits is around 50 mils with the inlet bearing being over 80 mils. The figure shows that the orbit near the pump inlet (Shaft 1) has the biggest diameter and it tends to be circular. At 185 hours, the bottom orbit is out of the range of the proximity probes. Shaft 2 has a significantly smaller orbit which begins relatively circular but become

elliptical at the end of the experiment. The orbits at position shaft 3 have relative small diameters, because it near the top motor. An interesting observation is that the two impeller seals have ultimate orbits smaller than Shaft 1, and 3 while Shaft 2 is smaller. It appears that as the erosion progresses the impeller seals are starting to replace the bearings as the load carrying components. It is obvious that after injecting air in the pump, the diameters of the orbits increase rapidly. This is due to radial rotor forces exceeding the load capacity of the bearings causing rubbing of the bearing surfaces. This explains how the heat checking occurs.

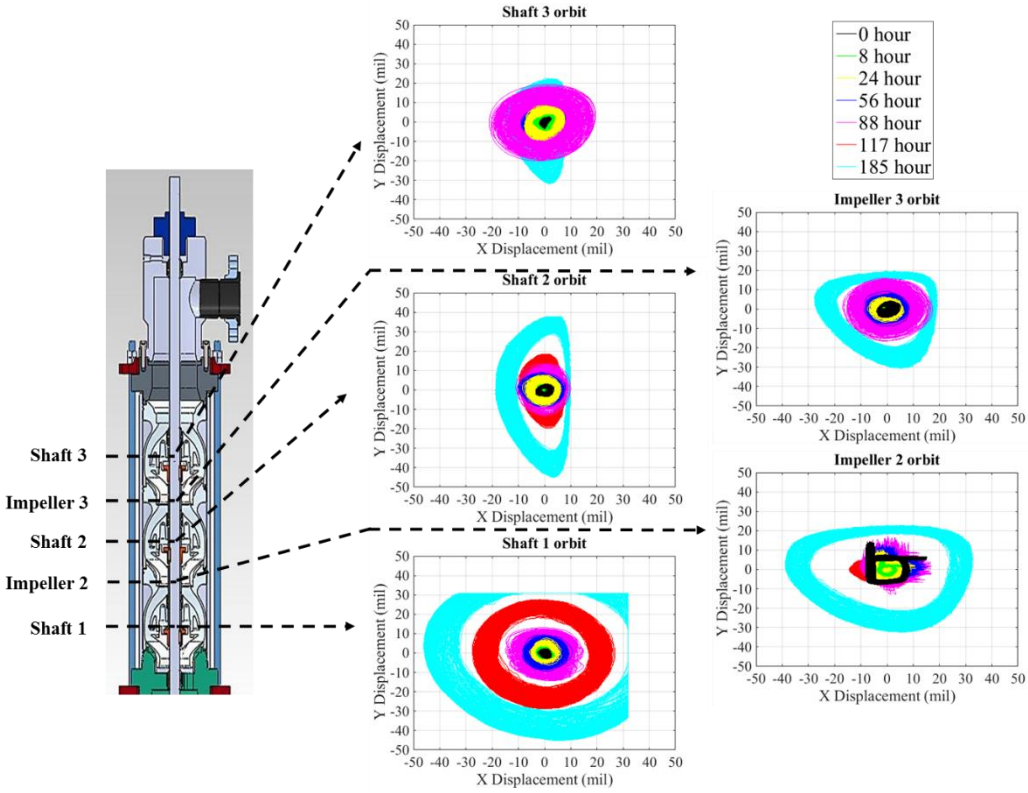

Figure 2-5 Pump components orbits at different erosion hours

2.1.3.4 Spectrum analysis

The magnitude spectra of displacements at 3600RPM and different erosion hours are analyzed. The waterfall plots of the displacements in x direction at different hours are shown in Figure 2-6.

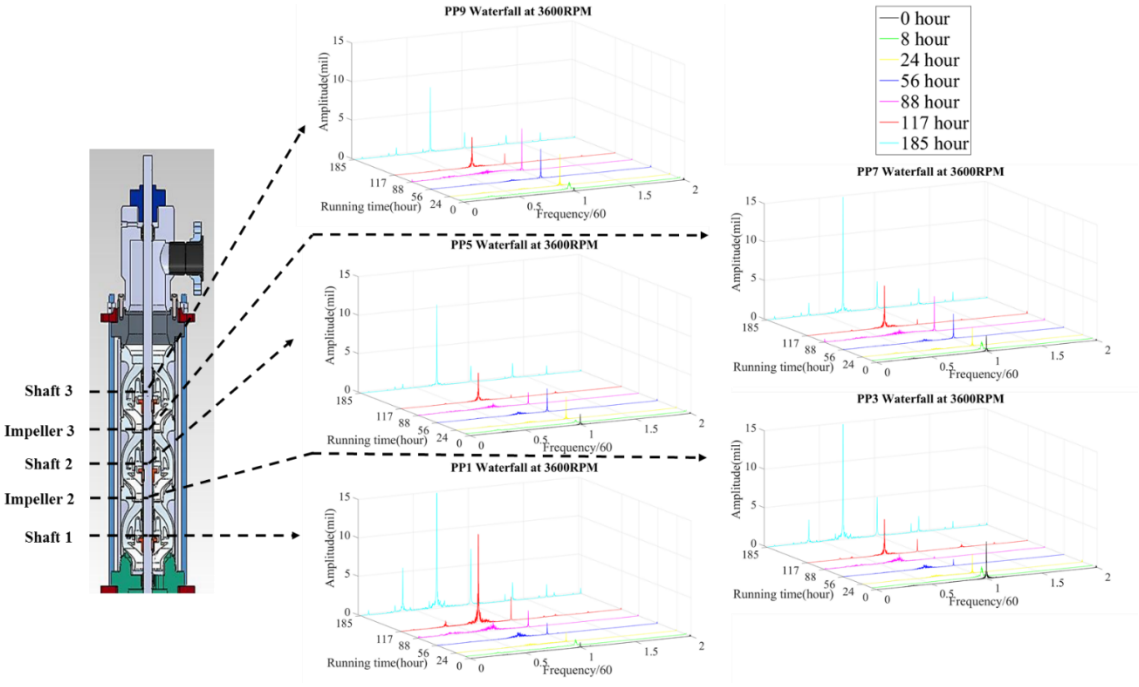

Figure 2-6 Waterfall plots at different hours of erosion

Since the spectra's magnitude at 185 hours is much larger than that at other erosion hours, the range of z axis is limited to 15 mils to see the spectrums clearly in Figure 2-6. The x-axis of each figure shows the frequency/60. Thus, x=1 means the vibration frequency is coincident with the spin frequency (3600 RPM = 60 Hz), which is called harmonic vibration. And a decimal less than 1 in x-axis means the vibration frequency is less than the spin frequency, which is called sub-harmonic vibration. The waterfall plots at each location show that the vibrations are small and harmonic at 0 hour. As the erosion

experiments are under way, 2/3 sub-harmonic vibrations occur. After 117 hours of erosion, the 2/3 sub-harmonic vibration is greater than the harmonic one and dominates the motion.

2.1.3.5 Summary

The erosion experiment shows the wear of bearings and the development of the sub-harmonic vibration in the ESP. The vibration, especially the sub-harmonic vibration, can accelerate the erosion process and even cause failure of the entire ESP system. The erosion of bearings and seals in the ESP affects the rotordynamic behavior significantly. It is one of the possible reasons for the sub-harmonic vibrations of the ESP.

2.2 Design of the Bearing/Seal Test Rig

The erosion study of the ESP shows that studying the rotordynamic behavior and material fatigue of bearings/seals in ESPs is important. However, it is expensive and takes several months to conduct a 185 hours of erosion experiment on the 3-stage real ESP. A more efficient way to test the bearings/seals should be found. Thus, the design of a vertical bearing/seal test rig is proposed. The design objectives of the test rig are as follows:

1) Simulate the mass imbalance of the eroded components in the ESP.
2) Conduct the multi-phase flow experiment efficiently.
3) Monitor the fluid in the clearance of the bearing/seal in real time.
4) Inspect the bearing surfaces easily.

2.2.1 Overview

To achieve the above objectives, the P&ID diagram of the test rig is shown in Figure 2-7.

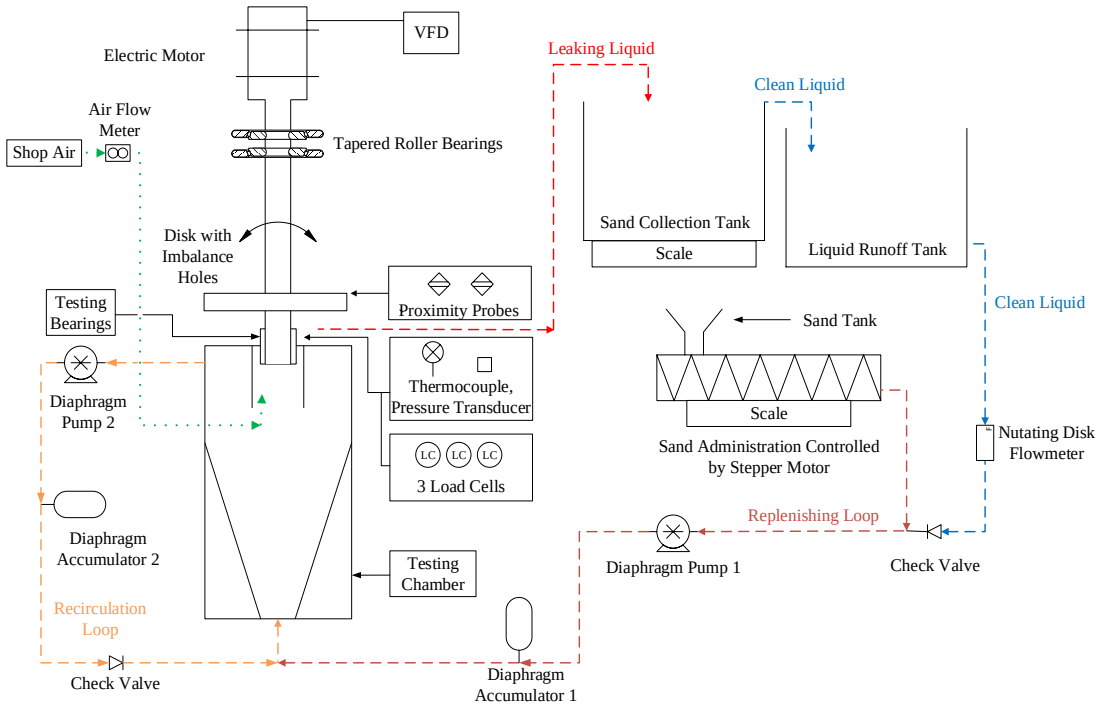

Figure 2-7 P&ID diagram of the test rig

The test bearing/seal is mounted on the bottom of a shaft which is driven by an electric motor. The speed of the motor is controlled by a Variable Frequency Driver (VFD). To fix the shaft in both axial and radial directions, two tapered roller bearings are mounted back to back on the top of the shaft. An unbalanced disk is mounted close to the test bearing. It is designed to simulate the imbalance forces generated by eroded impellers in the ESP. Two proximity probes are installed orthogonally above the disk to monitor the shaft orbits. The sleeve is assembled on the shaft by a key and two snap rings. The bushing of the test bearing is installed in an apparatus which is connected to the testing chamber. Three load cells, a thermocouple, and a dynamic pressure transducer are installed in the apparatus to monitor the forces, temperature and pressures.

An air loop and two flow loops (the replenishing loop and the recirculation loop) are used in the design. The liquid and sand are pumped into the testing chamber from the bottom. A conical bottom is added to the testing chamber to funnel settling sand into the upward stream of fluid entering the chamber. A portion of the incoming liquid and sand passes through the bearing clearance on the top of the testing chamber. The rest of the incoming liquid and sand are pumped back into the testing chamber through the recirculation loop. The pressure at the bottom of the test bearing is maintained by two diaphragm pumps. The leakage from the bearing clearance firstly flows into the sand collection tank, where the sand settles onto the bottom. Only clean liquid flows into the liquid runoff tank, where clean liquid is also added to maintain the fluid level. In this case, the sand that passes through the bearing is removed so that the sand only passes once through the test bearing. New sand is added before the diaphragm pump into the replenishing loop to maintain the sand concentration. The diaphragm accumulator in each flow loop is used to attenuate the pressure fluctuation caused by the diaphragm pump. The air is injected below the inlet of the test bearing. A short cylinder under the test bearing is used to make sure that all the injected air passes through the bearing clearance.

2.2.2 Theoretical Calculation

2.2.2.1 Removal of used sand

To make sure the sand settles in the sand collection tank but doesn't in the testing chamber, the sedimentation rate of sand is calculated. The equation of motion is:

$$G_s = F_D + F_B \tag{2.1}$$

where:

G_s is the force of gravity on the sand particles;

F_D is the drag of water on the sand particles;

F_B is the buoyancy force of water exerted on the sand particles;

The water drag force is calculated by Equation (2.2):

$$F_D = \frac{1}{2}\rho V^2 C_D A \tag{2.2}$$

where:

F_D is the drag force;

ρ is the density;

V is the relative velocity;

A is the cross-section area;

C_D is the drag coefficient, which is related to the Reynolds number.

Assuming the sand is spherical and submitting the corresponding formula of G_s, F_D, and F_B, we obtain

$$\rho_s g \frac{\pi d^3}{6} = \frac{1}{2}\rho_w V^2 C_D \frac{\pi d^2}{4} + \rho_w g \frac{\pi d^3}{6} \tag{2.3}$$

where:

ρ_s is the density of sand, and $\rho_s = 1602\ kg/m^3$;

ρ_w is the density of water, and $\rho_w = 1000\ kg/m^3$;

d is the diameter of the sand particle.

Since the Reynolds number is greater than 1000, the drag coefficient $C_D \approx 0.45$. The sedimentation rate of sand for different diameters are shown in Table 2-4. To make

sure sands cannot precipitate in the testing chamber, the flow rate in the testing chamber should be greater than the maximum sedimentation rate. While, to make sure sand is removed in the sand collection tank, the flow rate should be smaller than the minimum sedimentation rate.

Table 2-4 Sedimentation rates of sands

Sand size	Sedimentation Rate
100 mesh	2.01 in/s
140 mesh	1.69 in/s
200 mesh	1.43 in/s

2.2.2.2 Liquid leakage rate

To simulate the pressure difference between stages in the WJE-1000 ESP, the pressure between the top and bottom of the test bearing is maintained at 50PSI. Three bearings with different outside diameters are designed. The radial clearances are 6 mils, 12.5 mils, and 25 mils respectively. The liquid leakage rates for different clearances are calculated by CFD using ANSYS Fluent and shown in Table 2-5.

Table 2-5 Liquid leakage rates

	6 mils	12.5 mils	25 mils
Leakage (GPM)	7	15	30

2.2.2.3 Dimensions of the sand collection tank

The sand collection tank receives the leakage from the bearing clearance and lets the sand settle on the bottom. In normal working conditions, the sand collection tank is

always full and only clean liquid exiting into the following tank through a hole on the top of the tank. Since the tank is always full, the liquid entering rate is the same as that exiting the tank. In the experiment, the maximum liquid leakage rate is 30GPM. Setting a safety factor as 2, a 60GPM entering flow rate was considered. To make sure the sand can settle on the bottom, the vertical flow rate in the tank should be smaller than the minimum sedimentation rate of sand (1.43 in/s), which is calculated in Table 2-5. Based on these requirements, the selected sand collection tank is shown in the figure below.

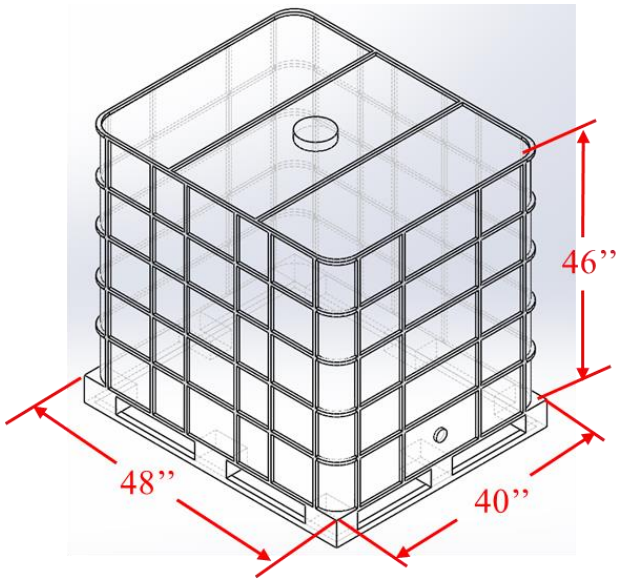

Figure 2-8 Sand collection tank

The dimension of the tank is 48''×40''×46'' (Length × Width × Height). Its capacity is 275 gal. The liquid's rising velocity is 0.12 in/s which is smaller than 1.43 in/s.

2.2.2.4 Motor power

The power of the motor must be enough to drive the shaft and unbalanced disk. Considering the power loss of the tapered roller bearings and plan journal bearings, the total horse power (HP) of the motor is:

$$HP_{total} = HP_{disk} + HP_{loss\_roller} + HP_{loss\_journal} \tag{2.4}$$

where:

HP_{total} is the total horse powers of motor;

HP_{disk} is the horse power needed to rotate the disk;

HP_{loss_roller} is the horse power loss of tapered roller bearing;

$HP_{loss\_journal}$ is the horse power loss of journal bearing.

1) Horse power needed to rotate the disk

The equation of motion for the disk is:

$$I_p \ddot{\theta} = T \tag{2.5}$$

where:

I_p is the moment of momentum of the disk ($kg - m^2$);

θ is the rotation angle of the unbalanced disk (rad);

$\ddot{\theta}$ is the second time differential of θ;

T is the torque (Nm).

Integrate Equation (2.5) respecting to time, we obtain:

$$\dot{\theta}(t) = \frac{T}{I_p} t + c_1 \tag{2.6}$$

where:

t is the time needed for the disk to reach a certain speed;

c_1 is a constant.

Submit the initial conditions $\theta = \dot{\theta} = 0$ into Equation(2.6), $c_1 = 0$ and

$$T = \dot{\theta}(t) I_p / t \tag{2.7}$$

For the designed unbalanced disk, $I_p = 0.025 \ \ kg - m^2$, the maximum desired spin speed is $\dot{\theta}(t) = 8000rpm = 837.758 rad/s$. The accelerating time is chosen as 20 seconds. Then the torque required to rotate the disk is 1.04 Nm (9.27 lb-in). The required horse power is calculated by the following equation:

$$HP = \frac{T \cdot N}{5252} \tag{2.8}$$

where:

T is the torque ($lb - in$);

N is the spin speed (RPM).

Then, the power needed to speed up the disk to 8000 RPM in 20s is 14.12 hp.

2) Horse power loss of the roller bearing

The equation to calculate the power loss of roller bearings is:

$$N_R = M_f \frac{\pi N}{30} \tag{2.9}$$

where:

N_R is the power loss of the roller bearing (W);

N is the spin speed of the bearing (RPM);

M_f is the friction moment.

Under the assumption of normal operational conditions and good lubrication, an approximate friction moment can be calculated using the equation:

$$M_f \approx f \cdot p \cdot \frac{d}{2} \tag{2.10}$$

where:

f is the coefficient of friction (depending on the type of bearings, $f \in [0.001, 0.005]$);

d is the diameter of the bearing hole (m);

p is the equivalent dynamic load of the bearing (N).

In the design, $f = 0.005$, $d = 1.5\ in = 0.0381\ m$, $p \approx 25000N$, and $N = 8000\ RPM$. Based on Equation (2.9) and Equation(2.10), the power loss of the roller bearing is $N_R = 1995\ W = 2.68\ HP$.

Since the force acting on the journal bearing is three times larger than that on the roller bearing, and the HP loss is proportional to the acting force, it is reasonable to estimate the HP loss of the testing journal bearing is three times larger than that of the roller bearing.

3) Motor horse power

Based on Equation (2.4) and the calculation above, the total motor horse power is:

$$\begin{aligned} HP_{total} &= HP_{disk} + HP_{loss_{roller}} + HP_{loss_{journal}} \\ &= 14.12 + 2.68 \times 2 + 2.68 \times 3 \\ &= 27.52 \end{aligned}$$

Considering the safety factor, a 40HP motor was chosen for the test rig.

2.2.2.5 Control algorithm of the sand administration

To maintain a consistent sand concentration, the rate of sand collected in the sand collection tank should be used to control the sand administration system. The weight of the supplementary sand is recorded in real time. As shown in Figure 2-7, there are scales under the sand collection tank and the sand tank respectively. During the experiment, the sand collection tank is always full, the volume of the sand collection tank is

$$V_{total} = V_l + V_s \tag{2.11}$$

where:

V_{total} is the total volume of tank, which is known;

V_l is the volume of the liquid;

V_s is the volume of the sand.

The weight of the liquid and sand in the sand collection tank is:

$$w = w_{total} - w_{tank} = \rho_l V_l + \rho_s V_s \tag{2.12}$$

where:

w_{total} is the total weight including tank, liquid and sand;

w_{tank} is the weight of the tank;

ρ_l is the density of the liquid;

ρ_s is the density of the sand.

The volume of sand can be calculated as:

$$V_s = \frac{w - \rho_l V_{total}}{\rho_s - \rho_l} \tag{2.13}$$

Then the mass of the precipitated sands is:

$$m_s = \rho_s V_s = \rho_s \frac{w - \rho_w V_{total}}{\rho_s - \rho_w} \tag{2.14}$$

The supplementary sand in a certain time interval is:

$$\Delta m_s = m_{s\_previous} - m_{s\_current} \tag{2.15}$$

where:

$m_{s\_previous}$ and $m_{s\_current}$ are the masses of the precipitated sands measured at the last time point and current time point respectively.

2.2.3 Mechanical Design

The overview of the entire system is shown in Figure 2-9.

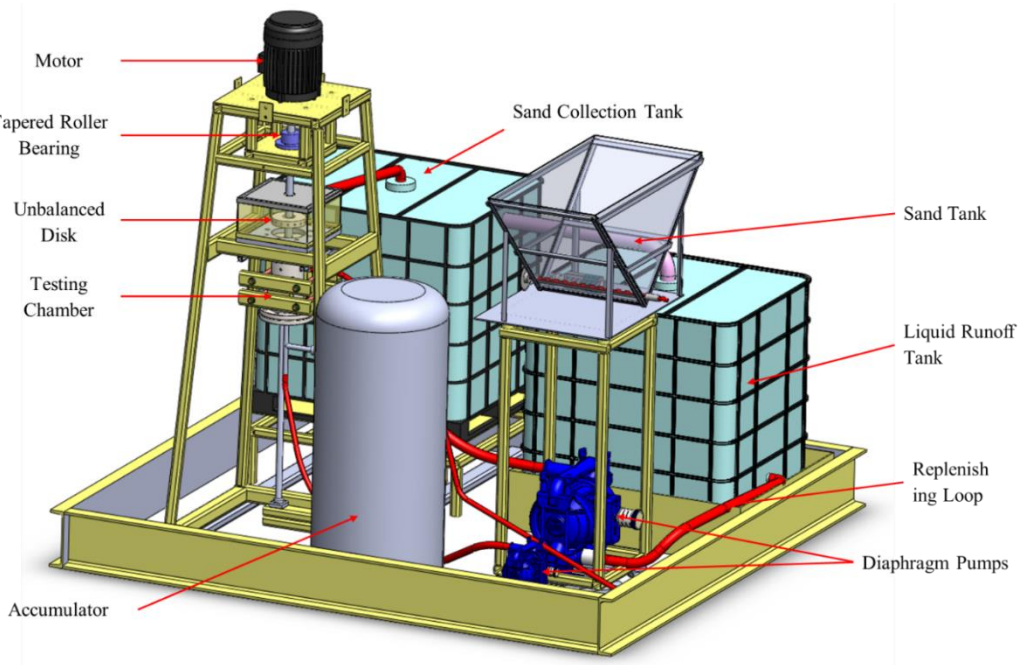

Figure 2-9 Overview of the bearing/seal test rig

All the components of the test rig are assembled in a pan which will collect the liquid when there are leakages. The design details are presented in the following section.

2.2.3.1 Shaft and unbalanced disk

A shaft with an unbalanced disk is designed to simulate the rotating motion of the shaft in a WJE-1000 ESP. The unbalanced disk is used to simulate the imbalances of the eroded impellers. To satisfy the design objective, the unbalanced disk should have similar operating orbits as the impellers in previous erosion experiments.

The dimensions of a WJE-1000 ESP are shown in Figure 2-10.

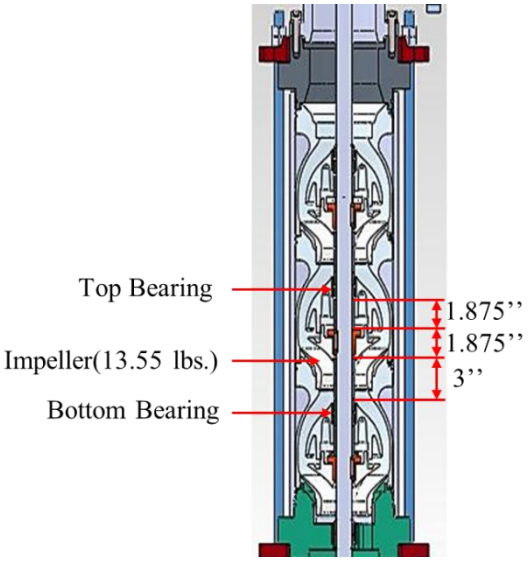

Figure 2-10 Dimensions of a WJE-1000 ESP

In the figure, the dimensions of the second stage are presented. The mass of each impeller is 13.55 lbs. The distance between the impeller and the top journal bearing is 1.875 inches and between the impeller and the bottom journal bearing is 3 inches. The dimensions of the designed shaft are shown in Figure 2-11.

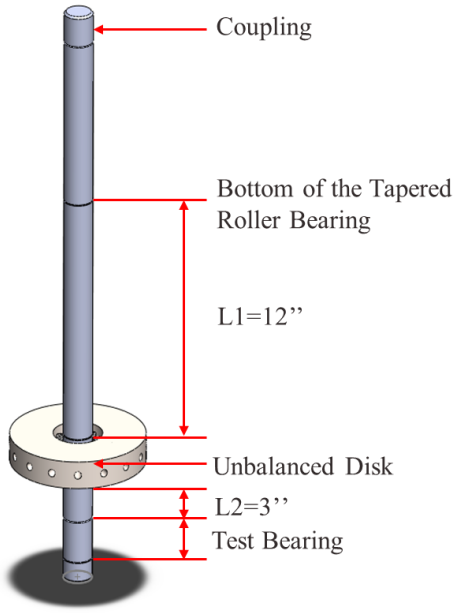

Figure 2-11 Dimensions of the designed shaft

The diameter of the designed shaft is 1.5 inches which is same as that of the WJE-1000 ESP. There are two tapered roller bearings on the top, which are used to support the weight of the shaft and disk as well as eliminating radial motions. The distance between the disk and the lower tapered roller bearing is 12 inches. The distance between the bottom of the disk and the journal bearing is 3 inches which is same as the distance between the impeller and the bottom bearing in the WJE 1000 ESP. In this case, the test bearing carries 4 times more loads than the top tapered roller bearings.

The designed unbalanced disk is shown in Figure 2-12.

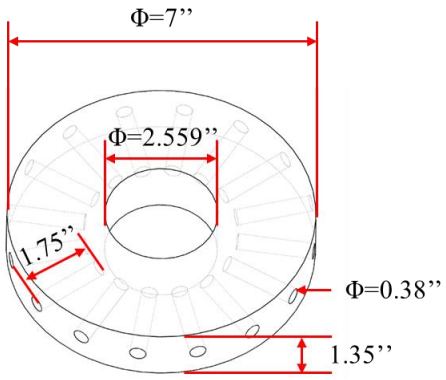

Figure 2-12 Dimensions of designed disk

The outside diameter of the unbalanced disk is 7 inches and the height is 1.35 inches. It is made by 316 stainless steel and the total mass is 11.68 lbs. There are 16 threaded holes around the disk. The imbalance of the disk can be adjusted by screwing set screws into the treaded holes. The diameter of imbalance holes is 0.38 inch and the depth is 1.75 inch. The allowed adjustable maximum eccentricity of the disk is 0.061 inch, which can generate a 323.3 g-in mass imbalance correspondingly. This is enough to simulate the imbalance of the impellers in the WJE-1000 ESP.

A balance machine as shown in Figure 2-13 is used to measure the mass imbalance of the unbalanced disk. The unbalanced disk is firstly balanced based on the ISO G1 criteria. And a certain mass imbalance value can be set by adding or removing the set screws. In this case, the mass imbalance of the disk can be controlled.

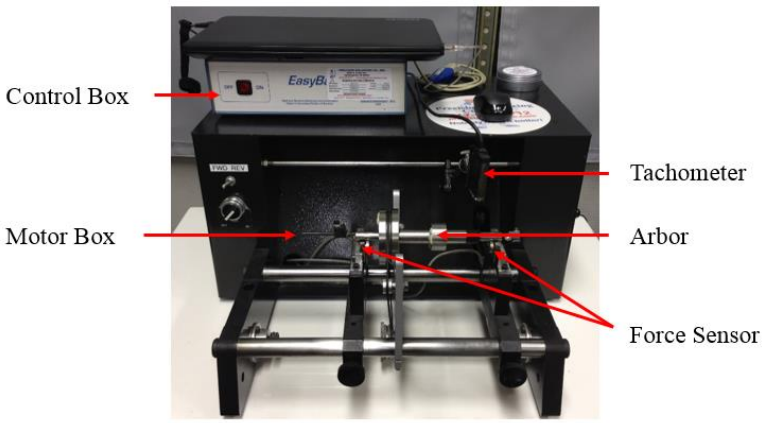

Figure 2-13 Balance machine

2.2.3.2 Testing chamber

The testing chamber is made from a 6-inch steel pipe. A conical bottom is added to the testing chamber to funnel settling sand into the upward stream of fluid entering the chamber. The cross section of the shaft and testing chamber is shown in Figure 2-14.

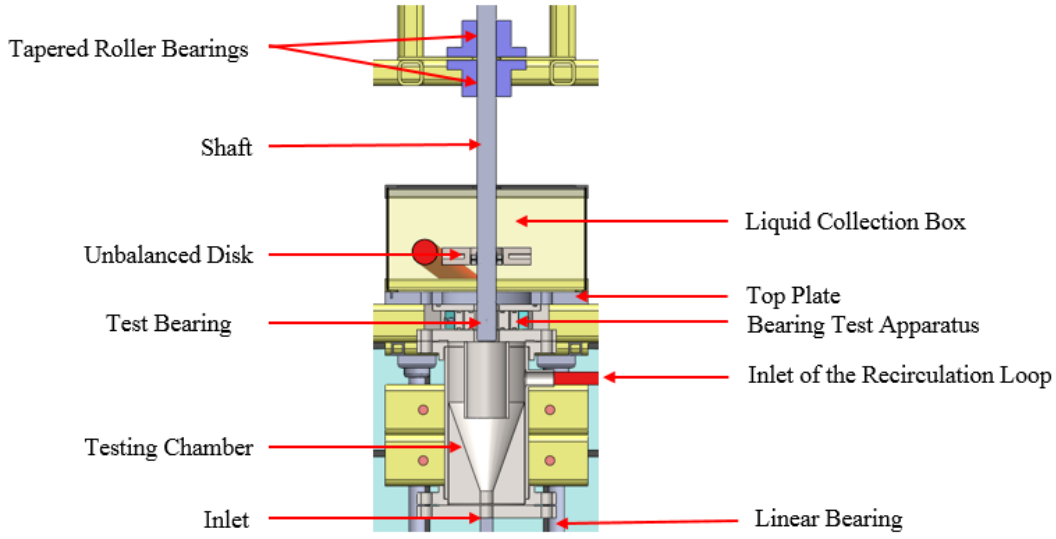

Figure 2-14 Cross sections of the shaft and testing chamber

As shown in Figure 2-14, the inlet is on the bottom of the testing chamber and the outlet is on the top. A 3-inch pipe is welded just below the test bearing. It is used to make sure the injected air goes through the bearing clearance. A liquid collection box is mounted on the top of the test bearing. It collects the liquid leaking from the bearing clearance, and guide the liquid to the sand collection tank. A portion of the incoming liquid and sand passes through the bearing clearance on the top of the testing chamber. The rest of the incoming liquid and sand are pumped back into the testing chamber through the recirculation loop. The location of the recirculation loop inlet is shown in Figure 2-14.

The testing chamber is mounted on a pair of linear bearings, and supported on the top plate. It is easy to disassemble the test bearings when needed. The linear bearings allow vertical motions of the testing chamber, so the bearing can be opened for inspection while maintaining alignment. In addition, two orthogonal locating pins are used to fix the relative position between the top plate and the testing chamber. On the top of the testing chamber, a flange is used to support the bearing test apparatus. The unbalanced disk is mounted on the shaft using a flush-mount screw-clamp bushing.

2.2.3.3 Bearing test apparatus

The bearing test apparatus is designed to mount all the probes which are used to monitor the parameters of the test bearing during the experiment. An exploded view and a top view of the bearing test apparatus are shown in Figure 2-15 and Figure 2-16 respectively.

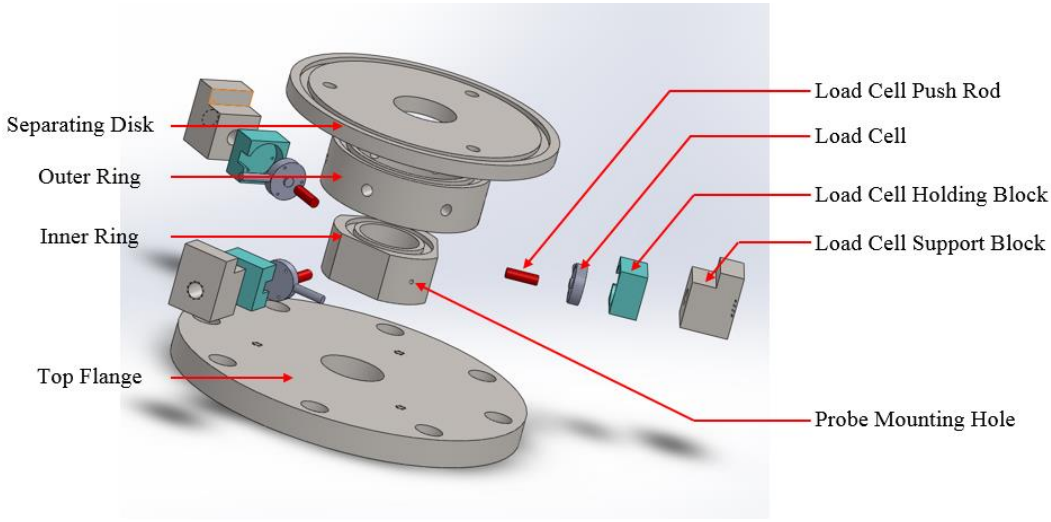

Figure 2-15 Exploded view of the bearing test apparatus

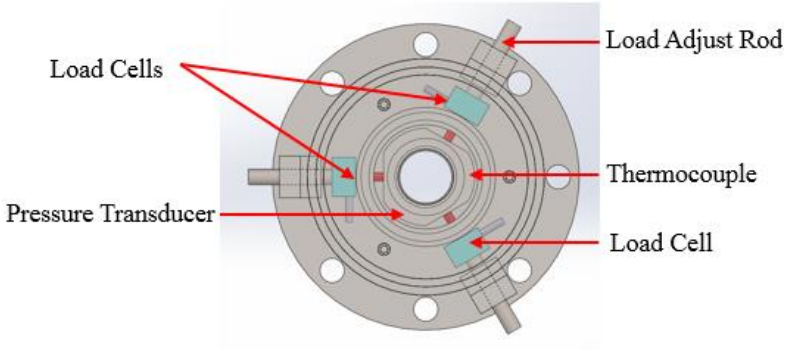

Figure 2-16 Top view of the bearing test apparatus

The components of the test apparatus include the separating disk, outer ring, inner ring, top flange, load cell push rods, load cell holding blocks, and support blocks. The inner ring is made of stainless steel and it is used as the bushing mount for the test bearing. The outer ring is used to support the load cell push rods, the pressure transducer, and the thermocouple. The outer ring and inner ring are fixed by the separating disk and top flange. The load cells are hold by the blocks and connected to the inner ring using small rods. Three load cell support blocks are welded on the top flange with a 120˚ interval angle.

Since the load cells only measure the compressive forces, they are preloaded by the load adjust rod to measure the force in both directions. As shown in Figure 2-16, a dynamic pressure transducer and a thermocouple are mounted through the outer ring. The details of the inner ring are shown in Figure 2-17. Two special holes are designed to let the probes reach the bearing clearance.

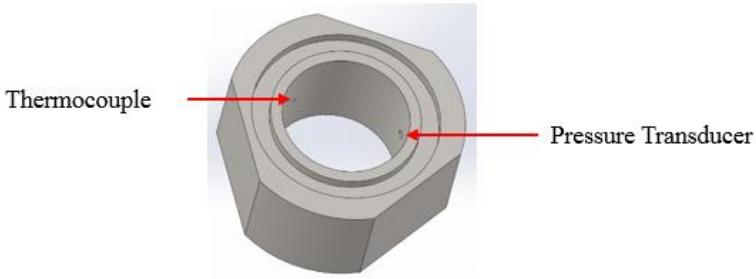

Figure 2-17 Probe mounting holes of the inner ring

2.2.4 Data Acquisition and Control System Design

The data acquisition and control system is designed to monitor the operating parameters, control the motor and diaphragm pumps. The instruments need to be controlled and the data need to be collected are shown in Table 2-6 and Table 2-7 respectively.

Table 2-6 List of instruments

No	Instrument	Function	Control value	Control device	Data Type
1.	Recirculating diaphragm pump	Recirculate the flow	Air input pressure or volume	Air pressure control valve	4-20 mA current
2.	Replenishing diaphragm pump	Maintain the pressure at the bearing inlet	Air input pressure or volume	Air pressure control valve	4-20 mA current
3.	Stepper motor	Supplement sands to maintain the sand concentration	Rotation speed and number of rotation.	Computer, Motor Drive	RS-232
4.	VFD	Control the speed of the motor	Frequency of motor's power supply	Computer	RS-485
5.	Control valve	Control the flow rate in the air loop	Percentage of open	NI AI module	4-20 mA current

Table 2-7 List of data acquisition instruments

No	Instrument	Function	Data Type
1.	Proximity probe	Measure the orbit of the disk	Voltage
2.	Dynamic pressure transducer	Measure the dynamic pressure in the bearing clearance	Voltage
3.	Static pressure transducer	1) Measure the static pressure in the testing chamber 2) Measure the pressure at the inlet and outlet of air loop	4-20 mA current
4.	Thermocouple	Measure the temperature in the bearing clearance	Voltage
5.	Load cell	Measure the load on the bushing	Voltage
6.	Scale	Measure the weight of the sand tank, collection tank, and the sand tank	RS 232
7.	Nutating disk flow meter	Measure the flow rate in the replenishing loop	4-20 mA current
8.	Tachometer	Measure the spin speed of the shaft	Voltage pulse
9.	Air flow meter	Measure the flow rate in the air loop	4-20 mA

2.2.4.1 NI hardware selection

The National Instrument cRIO-9074 real time controller and C series modules are selected based on the requirements of the system. The selected C series modules are as follows:

- NI 9215: Simultaneous Analog Input Module
- NI 9237: Half/Full-Bridge Analog Input Module
- NI 9213: Thermocouple Input Module
- NI 9205: Voltage Input Module
- NI 9265: Analog Output Module
- NI 9215: Analog Input Module

To analyze the experimental data conveniently, the monitoring data in the bearing annulus should be collected simultaneously. The signals include pressure, temperature, and loads. NI 9215 and NI 9237 are used to collect the simultaneous data. The instrument connection chart is shown in Figure 2-18.

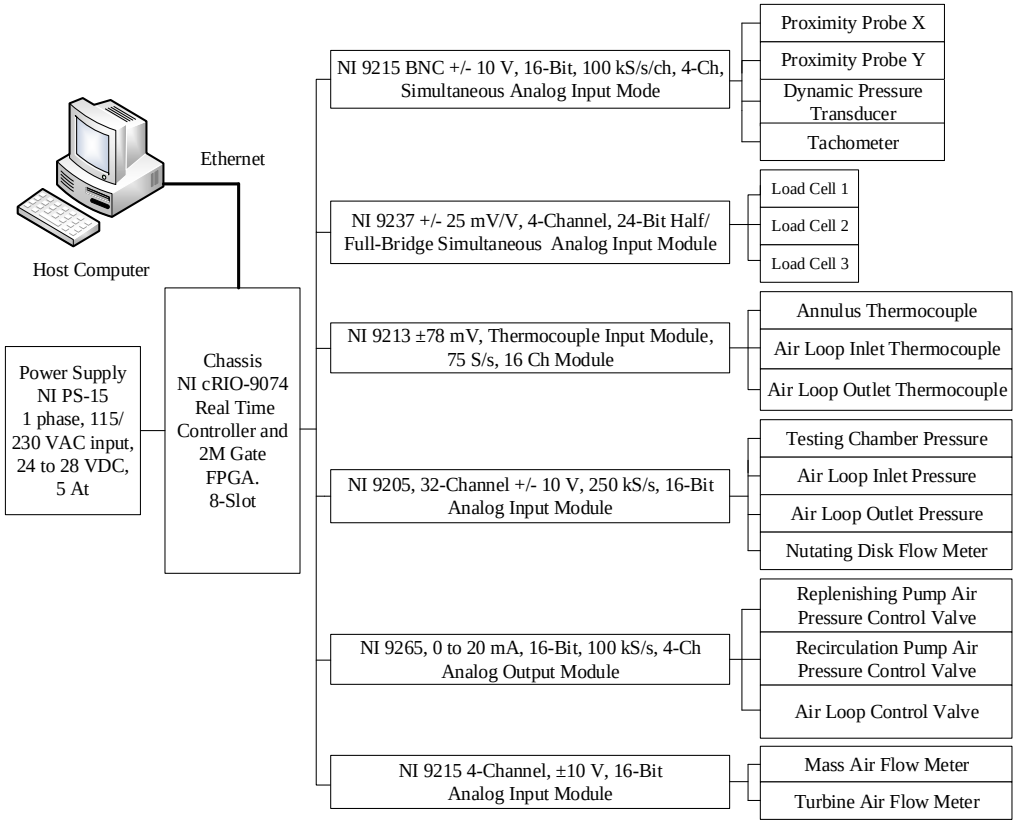

Figure 2-18 Instrument connection chart

As shown in the figure, the host computer communicates with NI cRIO real time controller through Ethernet. The voltage or current signals from the probes are recorded by different C series modules. The sampling frequencies and digital bits of the modules satisfy the Nyquist criterion and accuracy requirements of the system.

2.2.4.2 Electrical devices selection

Based on the chart in Figure 2-18, the corresponding electrical devices are selected and shown in Figure 2-19 to Figure 2-23.

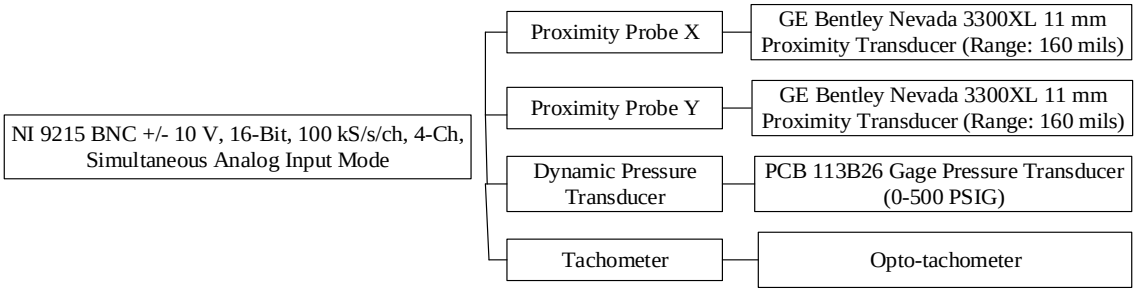

Figure 2-19 Devices connected to NI 9215

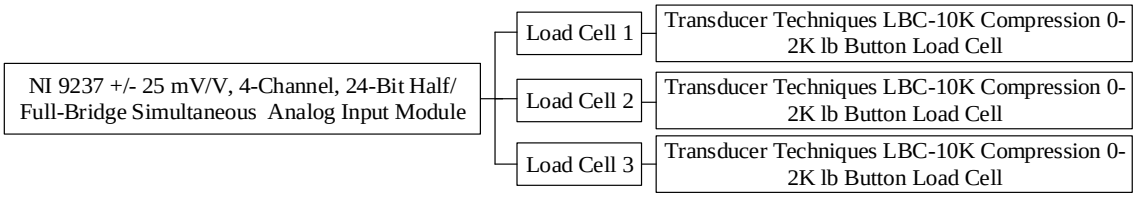

Figure 2-20 Devices connected to NI 9237

NI 9215 and NI 9237 are simultaneous modules and they share a same clock to achieve simultaneous data acquisition. The NI cRIO real time controller has three working modes: high speed mode, monitor mode, and hybrid mode. The hybrid mode allows the controller to work in two modes at the same time. The simultaneous data acquisition needs the controller working in the high-speed mode. Since only two modules work in simultaneous mode, the controller in this application is set in hybrid mode. The GE Bentley Nevada 3300XL 11 mm proximity transducers are selected to measure the vibration of the shaft. The range of the proximity probe is 160 mils and the linear range is 20 to 180 mils. Thus, the proximity probes are mounted about 100 mils away from the shaft. In this way, the probe can measure the displacement ranges from -80 to 80 mils. A PCB dynamic pressure transducer with a range of 0 to 500 PSIG is used to monitor the dynamic pressure in the bearing clearance. The compression button load cell has a range

of 0-2000 lbs. Shunt calibrations were conducted to make sure the accuracy of the load cells. A T type thermocouple is selected to measure the temperature in the bearing clearance, inlet and outlet of the air loop. The analog data from thermocouples are recorded by the NI 9213.

The devices connected to NI 9205 are shown in Figure 2-21. The Omega PX 429 pressure transducers with different ranges are used to measure static pressures. The pressure transducers transfer the gauge pressure to 4-20 mA current signal linearly. For the Nutating disk flow meter, the output is 4-20 mA current corresponding to 0-70 GPM. Passing through a resistor, current signals are transferred to voltage signals and recorded by the NI 9205.

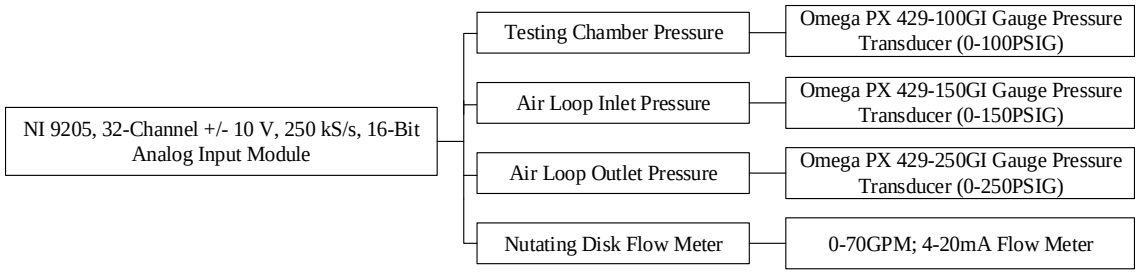

Figure 2-21 Devices connected to NI 9205

The NI 9265 module is an analog output module which can output a 0 to 20 mA current signal, which is always used as the reference signal for actuators. The devices controlled by NI 9265 are shown in Figure 2-22.

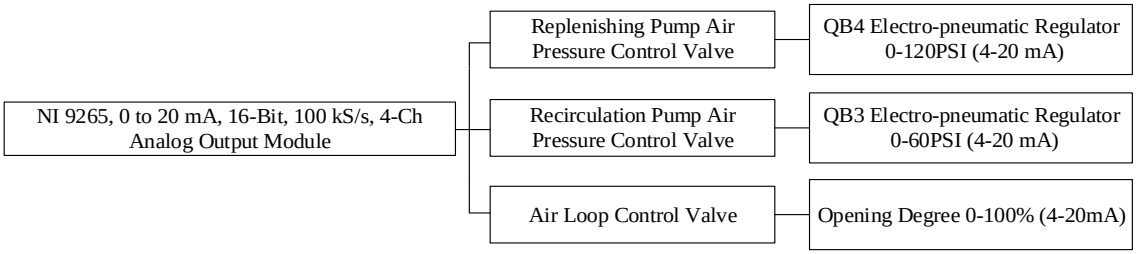

Figure 2-22 Devices connected to NI 9265

The electro-pneumatic regulators (QB3 and QB4) control the air output pressure based on the current reference signals from the NI 9265. The air loop control valve changes its open degree corresponding to the 0-20 mA signal given by the NI 9265.

The gas volume fraction (GVF) required by the test rig ranges from 0 to 60%. The range of a single turbine air flow meter is too large. It cannot measure the GVF below 40% when the bearing clearance is 6 mils. Thus, another mass air flow meter is selected to measure the small air flow rate. The signals from these two air flow meters are processed by NI 9215 as shown in Figure 2-23.

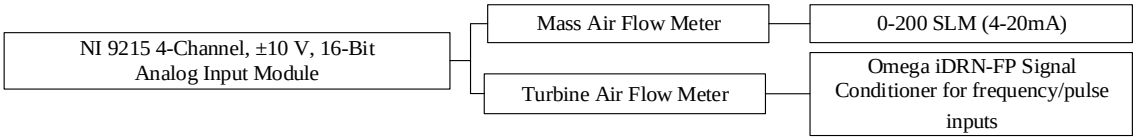

Figure 2-23 Devices connected to NI 9215

2.2.4.3 Control algorithm

The diaphragm pumps, the stepper motor, and VFD need to be controlled. The control algorithm for them are listed as follows.

1) Diaphragm pumps

The recirculation loop diaphragm pump is used to maintain the flow and avoid sand sedimentation in the testing chamber. The function of replenishing loop diaphragm pump

is to maintain the pressure at the inlet of the test bearing. An open loop control algorithm is chosen for both loops and it is shown in Figure 2-24.

Figure 2-24 Control diagram of diaphragm pumps

2) VFD and stepper motor

Since the VFD and stepper motor have their own controllers respectively. Both of their control orders are sent by serial communication ports in the host computer. The difference is that the stepper motor uses RS-232 communication protocol while VFD uses RS-485 communication protocol. The control signal for the VFD is the spin speed of motor. And the control signal of stepper motor is calculated based on the sand loss. The control diagram of VFD and stepper motor is shown in Figure 2-25.

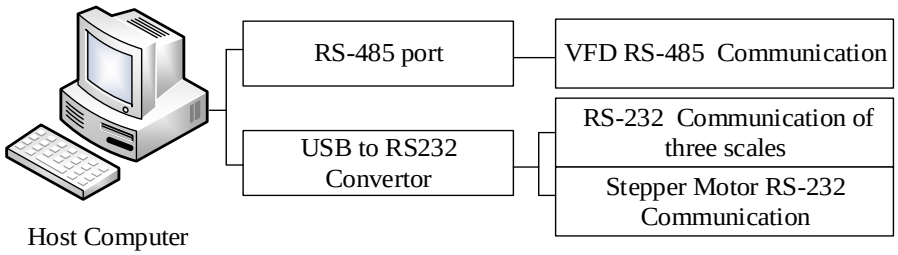

Figure 2-25 Control diagram of VFD and stepper motor

2.2.4.4 LabVIEW programming

Laboratory Virtual Instrument Engineering Workbench (LabVIEW) is a system design platform and development environment for a visual programming language from National Instruments. It is widely used for data acquisition, instrument control, and industrial automation. The programs run on the host computer includes the main control

program and the simultaneous data acquisition programs. The control panels are shown in the figures below.

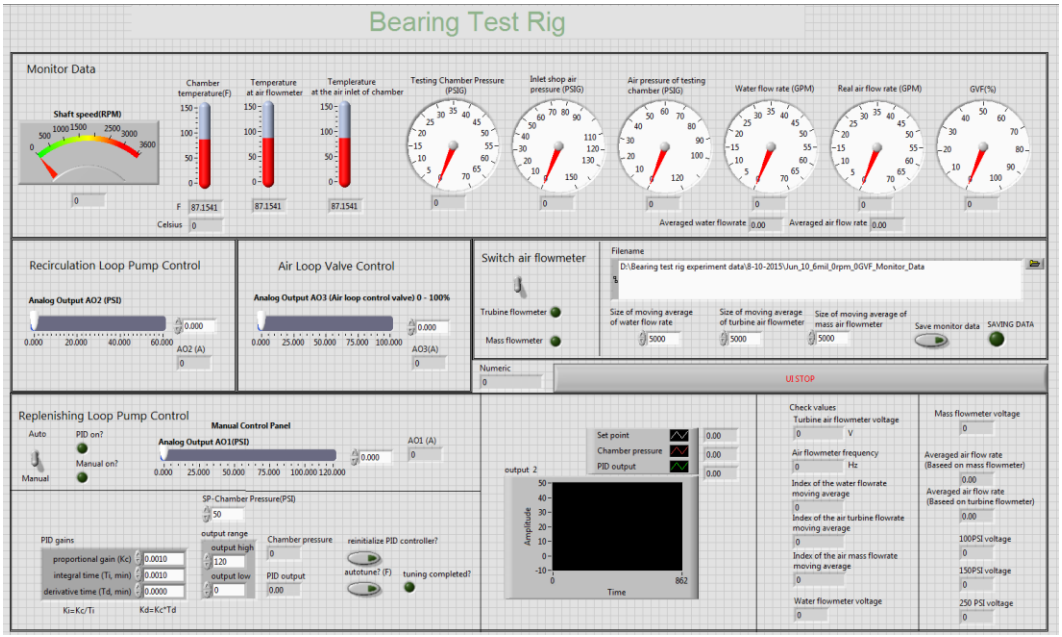

Figure 2-26 LabVIEW main program

The main program monitors the pressures, temperature, spin speed, and flow rate. It also controls the diaphragm pumps and the air loop control valve. In addition, all the monitoring data can be saved by the main program.

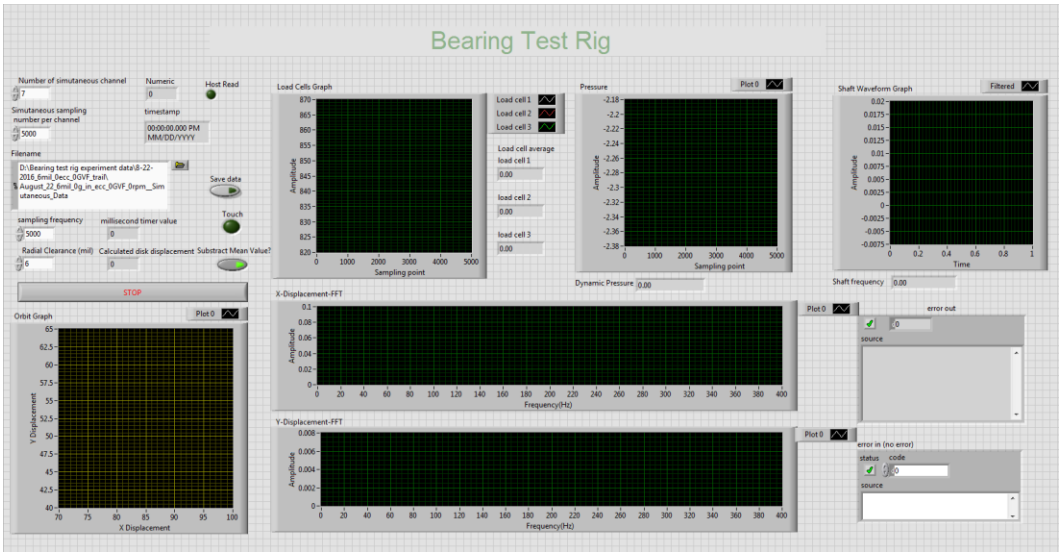

Figure 2-27 LabVIEW simultaneous program

The LabVIEW simultaneous program records the data which must to be collected simultaneously. These data include the pressure, temperature, and loads. The sampling frequency is 5 KHz, which satisfies the system's requirement, since the maximum spin frequency of the motor is 133.33 Hz (8000 RPM). The orbit of the shaft is shown in the lower left corner. All the data can be saved simultaneously.

2.2.5 Actual Bearing/Seal Test Rig

The test rig was built based on the mechanical and data acquisition system design. And the completed test rig is shown in the figures below.

Figure 2-28 Vertical bearing/seal test rig

Only two-phase (water and air) experiments are considered currently, thus the sand tank wasn't mounted. The NI Data acquisition hardware system is shown in Figure 2-29. In the figure, the NI hardware, power strip, DC power supply, and connection panel are mounted on a rack. The signal input/output ports are connected to the BNC connector panel or the thermocouple connector panel.

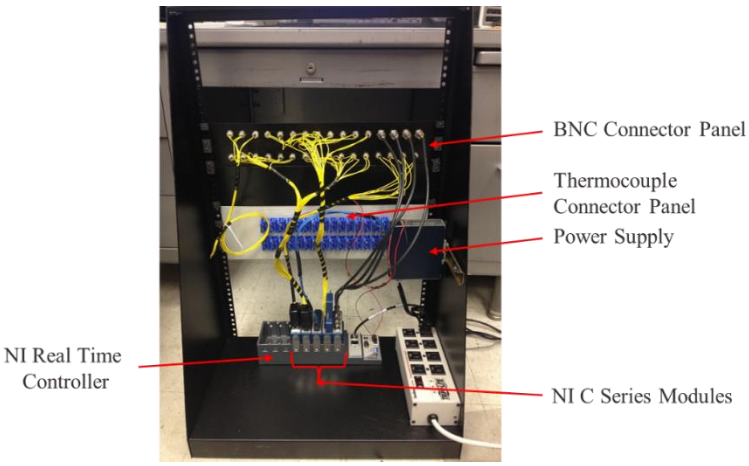

Figure 2-29 Data acquisition hardware system

3. EXPERIMENTAL RESULTS AND ANALYSIS

Experiments on journal bearings with different radial clearances, mass imbalances, and multi-phase flows (water and air) are conducted to study the dynamic behaviors of the plan journal bearings. The experimental conditions, transient and spectrum analysis are presented in this chapter.

3.1 Experimental Conditions

In the experiments, the radial clearance of bearing starts at 6mil since it is the original radial clearance of a WJE-1000 ESP. Based on the result of the erosion experiments, the radial clearance of the bearing increased up to 25 mils. Thus, bearings with 6, 12.5, and 25 mils radial clearance are tested. In the experiments, the bushing is made of stainless steel, and the journal is made of brass as shown in Figure 3-1.

Figure 3-1 Brass journal used in the experiments

In the experiments, the mass imbalance is measured and adjusted by the balance machine shown in Figure 2-13. Firstly, the disk is balanced based on the IOS G1.0 standard. Then, the mass imbalance is increased step by step until the journal and bushing contacts.

The experimental conditions are summarized as follows:

1) Bearing radial clearance: 6 mils, 12.5 mils, and 25 mils respectively
2) Lubrication: water and air
3) Pressure difference: 50 PSI for 6 mils and 12.5 mils bearing, 30 PSI for 25 mils bearings.
4) Gas volume fraction (GVF): 0%, 30%, 60%
5) Motor spin speeds: 600, 1200, 1800, 2400, 3000 and 3600 RPM
6) Mass imbalances: 0, 5 g-in, 10 g-in, 14 g-in 19 g-in, 31 g-in, 43 g-in, and 52 g-in.

Three load cells are mounted with an interval of 120°. Two proximity probes are mounted orthogonally above the unbalanced disk. The geometry relationships of the sensors are shown in Figure 3-2.

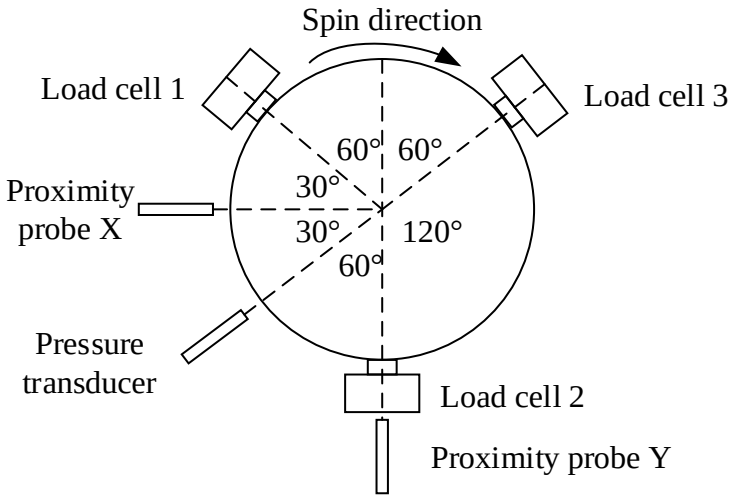

Figure 3-2 Geometry relationships of sensors

3.2 Experimental Results and Analysis

In this section, the shaft orbits, waterfall plot of the displacement, and the coherence between the displacement, force, and pressure are presented and analyzed.

3.2.1 Shaft Orbits

The shaft orbits are measured by a pair of orthogonal proximity probes above the mass imbalance disk. Some typical shaft orbits with different experimental conditions are shown in Figure 3-3, Figure 3-4, and Figure 3-5. The subtitle shows the radial clearance of the bearing, the mass imbalance of the disk, and the GVF respectively. The operating conditions shown are selected to present maximum orbit size without bearing rub. For the bearing with 6 mils and 12.5 mils radial clearance, the experiments are conducted with different mass imbalances and GVFs respectively. For the bearing with 25 mils radial clearance, only the experiments with 0% GVF and 30 PSI differential pressure are conducted.

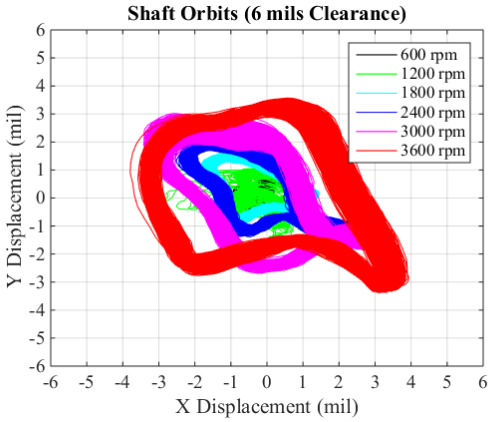

(a) 6 mils, 43 g-in, 0% GVF

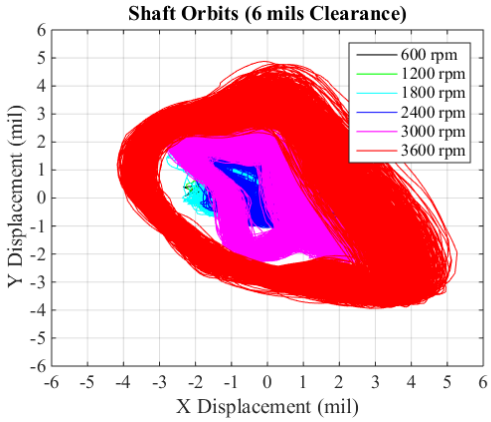

(b) 6 mils, 31 g-in, 30% GVF

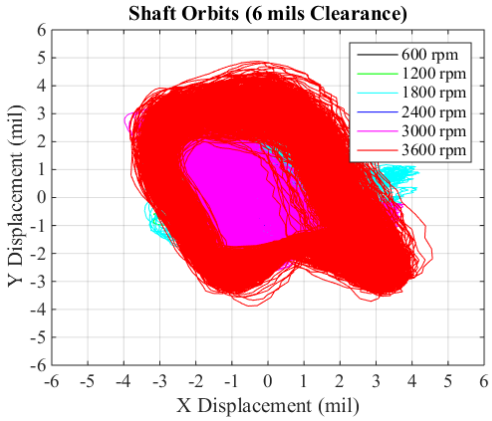

(c) 6 mils, 19 g-in, 60% GVF

Figure 3-3 Shaft orbits of the bearing with 6 mils radial clearance

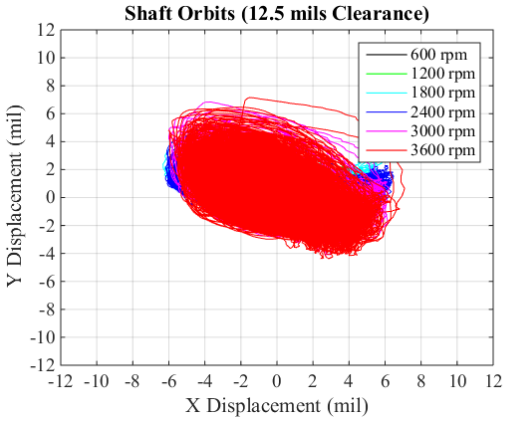

(a) 12.5 mils, 10 g-in, 30% GVF

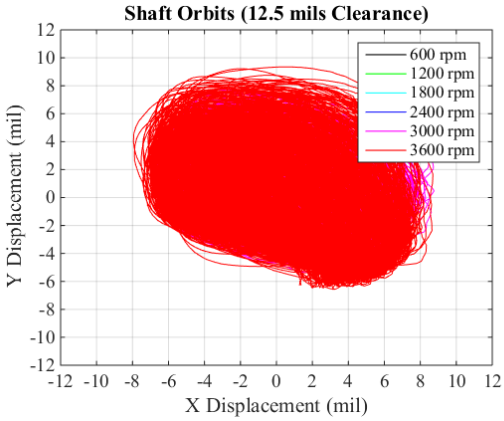

(b) 12.5 mils, 10 g-in, 60% GVF

Figure 3-4 Shaft orbits of the bearing with 12.5 mils radial clearance

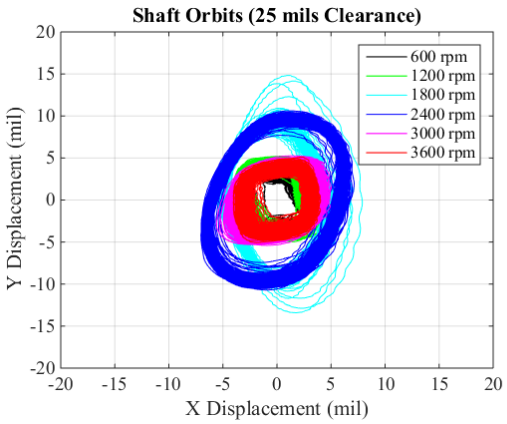

(a) 25 mils, 0 g-in, 0% GVF

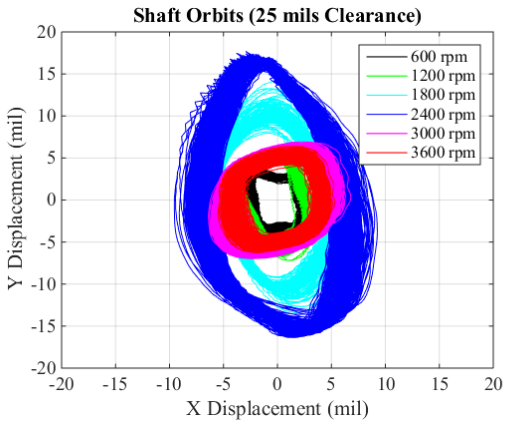

(b) 25 mils, 14 g-in, 0% GVF

Figure 3-5 Shaft orbits of the bearing with 25 mils radial clearance

Figure 3-3 and Figure 3-4 shows that:

1) Since the increase in unbalance force, the diameter of the orbits increases with increasing spin speed.
2) The diameter of the orbits increases with increasing GVF. After adding the air, the orbit reach the same radius as that of the experiments without air with a smaller mass imbalance. The air breaks the fluid film in the bearing clearance, thus decreases the load capacity.
3) The standard deviation of the orbits radius increases after injecting air.
4) For the bearing with 12.5 mils radial clearance, the shaft orbits with air show more noises than that of the bearing with 6 mils radial clearance. The diameter of the orbits with 60% GVF is greater than that of the orbits with 30% GVF, which means the load capacity decreases with increases in GVF.

The shaft orbits in Figure 3-5 shows that:

1) The diameter of the orbits increases with increasing mass imbalances.

2) The diameter of the orbits reaches the maximum value at 2400 RPM (40Hz) and reduces afterwards.

Figure 3-6 is presented to show the effects of the bearing clearance, mass imbalance, and GVF on the shaft orbits. It shows the error bar of shaft orbit radius of each bearing with different mass imbalances and GVFs at 3600 RPM.

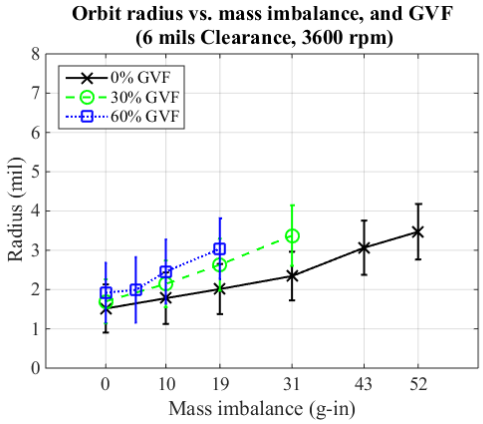

(a) 6 mils radial clearance

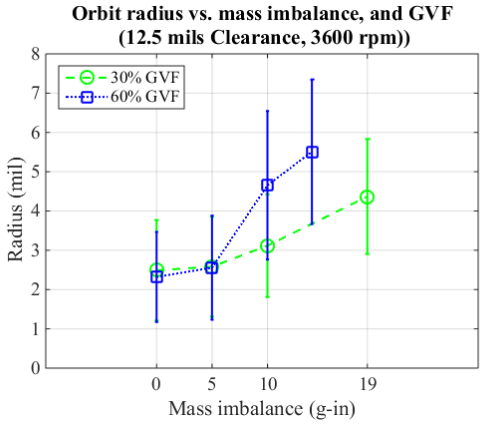

(b) 12.5 mils radial clearance

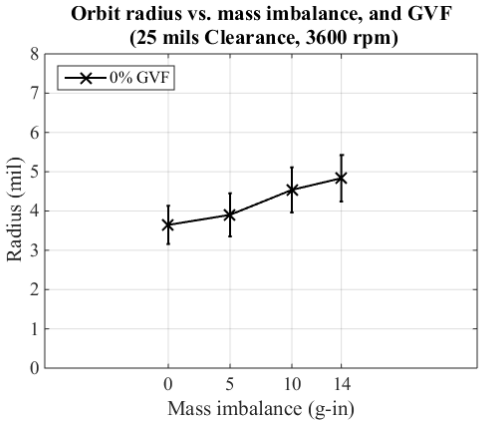

(c) 25 mils radial clearance

Figure 3-6 Orbit radius vs. mass imbalance, and GVF at 3600 RPM

Figure 3-6 shows that the orbit radius increases with increasing mass imbalance. Figure 3-6 (a) shows that the orbit radius increases with increasing GVF at same mass imbalances. The standard deviations of the orbit radius are similar. It also proved by the orbits in Figure 3-3. For the relationships between shaft orbit and mass imbalance, Figure 3-6 (b) shows the same trend as Figure 3-6 (a). The standard deviation of the orbits with 30% and 60% GVF are much greater. The displacement of the bearing with 12.5 mils radial clearance is greater than that of the bearing with 6 mils radial clearance under same experimental conditions.

Figure 3-6 (c) shows the same trend of the relationship between orbit radius and mass imbalances as Figure 3-6 (a) and Figure 3-6 (b), for the 25 mils bearing. But a much-reduced mass imbalance for a given orbit size illustrating the decrease in bearing load capacity with increasing clearance.

3.2.2 Waterfall

To study the spectra of the displacements with different spin speeds, some typical waterfall plots of the displacement in x direction are presented in Figure 3-7, Figure 3-8, and Figure 3-9 respectively. Since the maximum spin speed is 60Hz, the spectra range from 0 Hz to 180 Hz are shown in the figures.

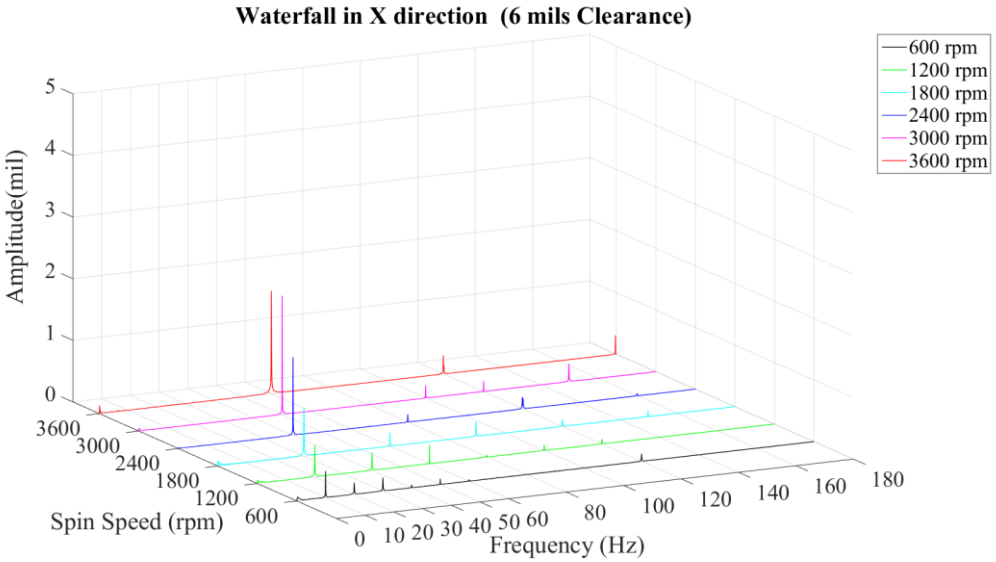

(a) 6 mils, 19 g-in, 0% GVF

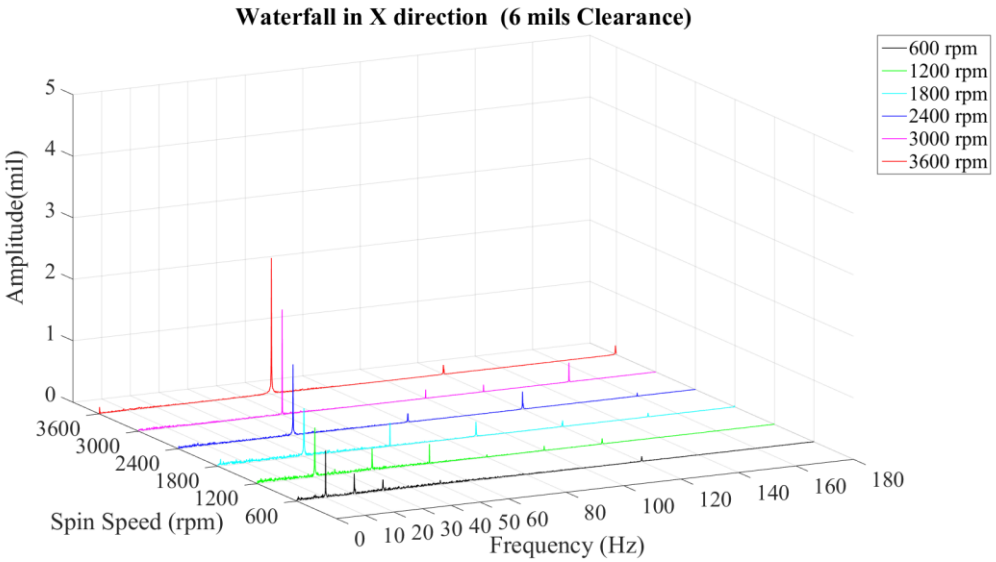

(b) 6 mils, 19 g-in, 30% GVF

Figure 3-7 Waterfall of the bearing with 6 mils radial clearance

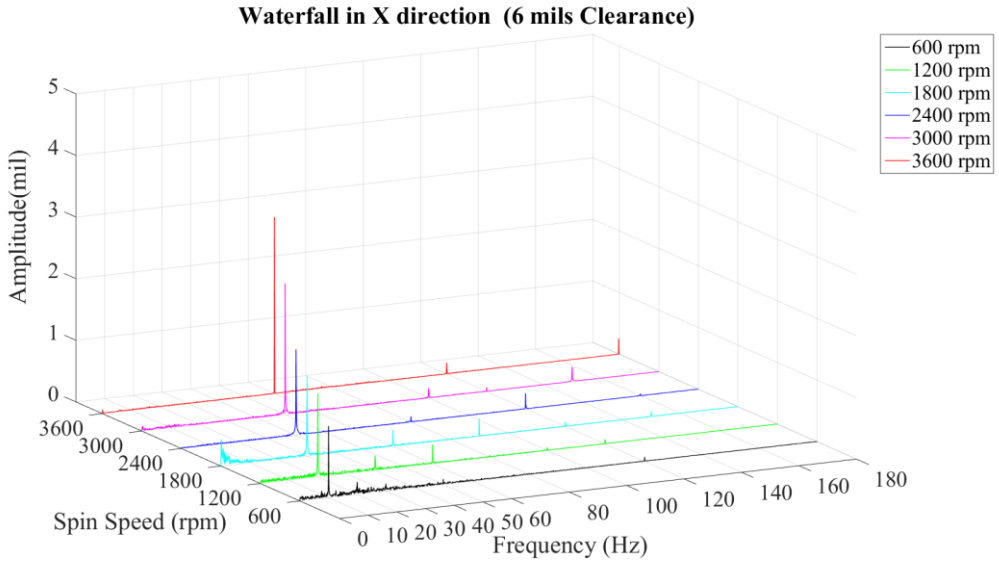

(c) 6 mils, 19 g-in, 60% GVF

Figure 3-7 Continued.

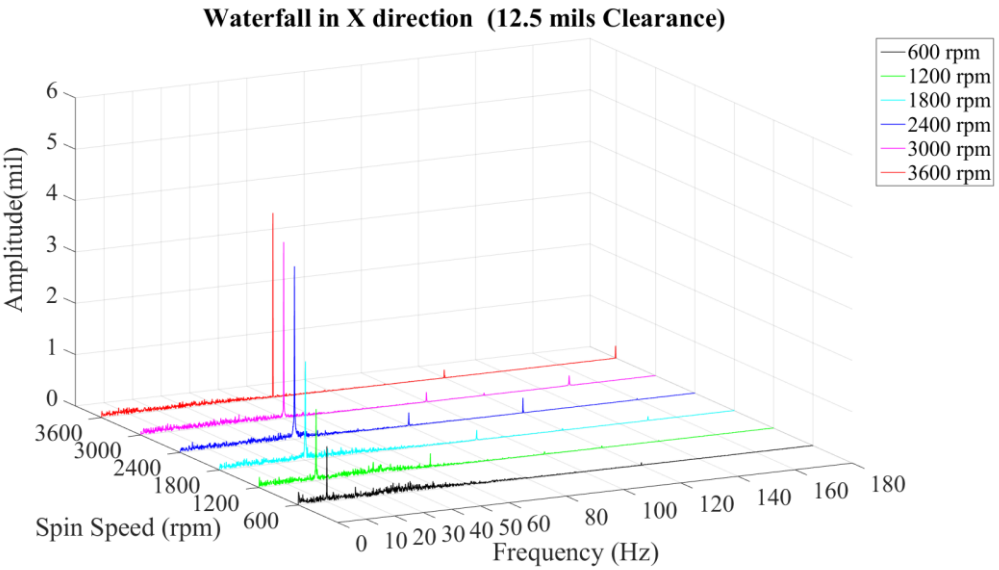

(a) 12.5 mils, 10 g-in, 30% GVF

Figure 3-8 Waterfall of the bearing with 12.5 mils radial clearance

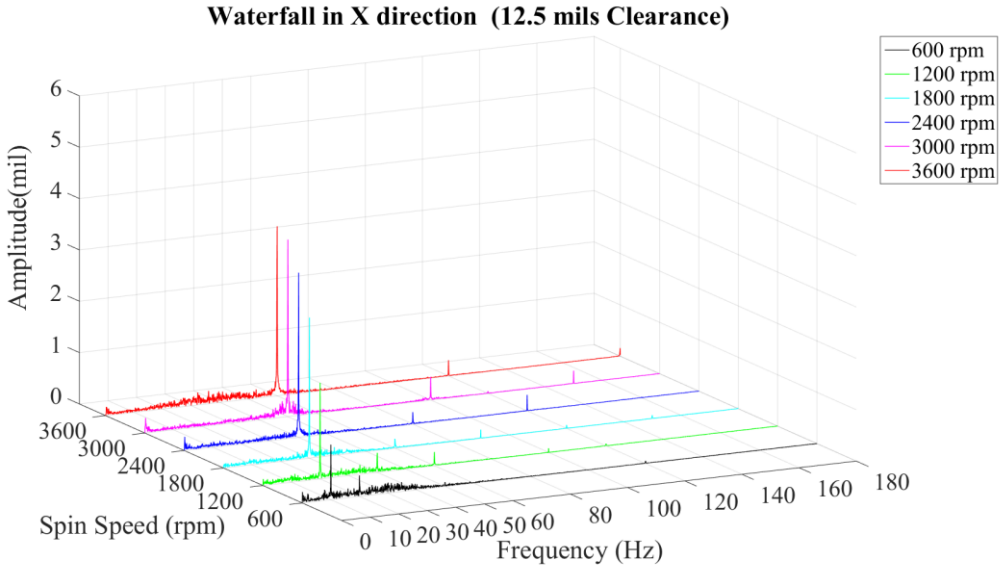

(b) 12.5 mils, 10 g-in, 60% GVF

Figure 3-8 Continued.

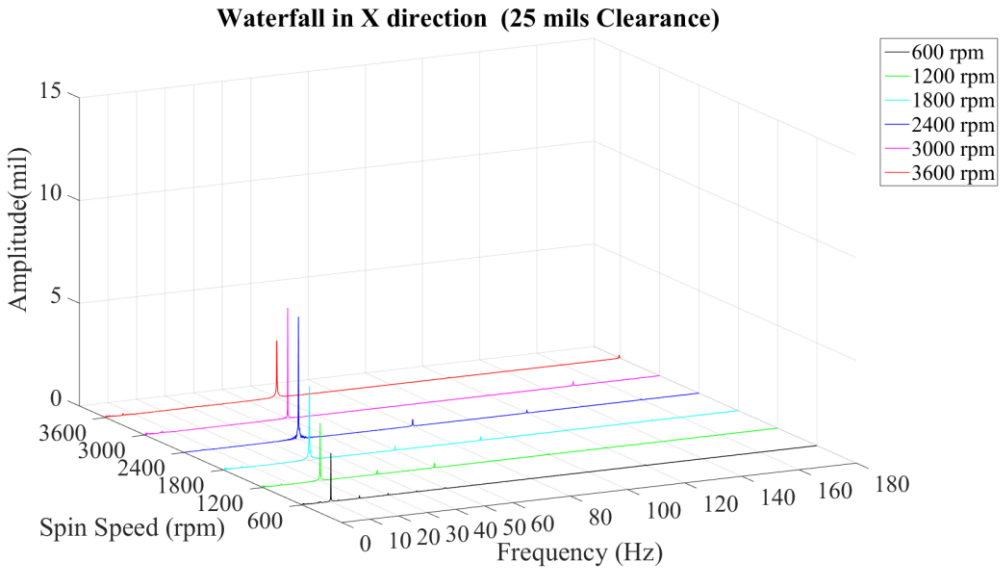

(a) 25 mils, 14 g-in, 0% GVF

Figure 3-9 Waterfall of the bearing with 25 mils radial clearance

Figure 3-7, Figure 3-8, and Figure 3-9 show that there are only synchronous vibrations during the experiments. After injecting the air in the experiments, some noise occurs between 0 and 60 Hz.

3.2.3 Coherence

The relationship between the displacements, dynamic pressure, and force, are important for analyzing the dynamic behaviors of the fluid film bearing. Figure 3-10, Figure 3-11, and Figure 3-12 show the relationship in the point view of the pressure transducer. It means that the force and displacement are shown relative to the position of the dynamic pressure transducer. In the figures, the red, blue, and green lines represent the dynamic pressure, displacement, and force respectively.

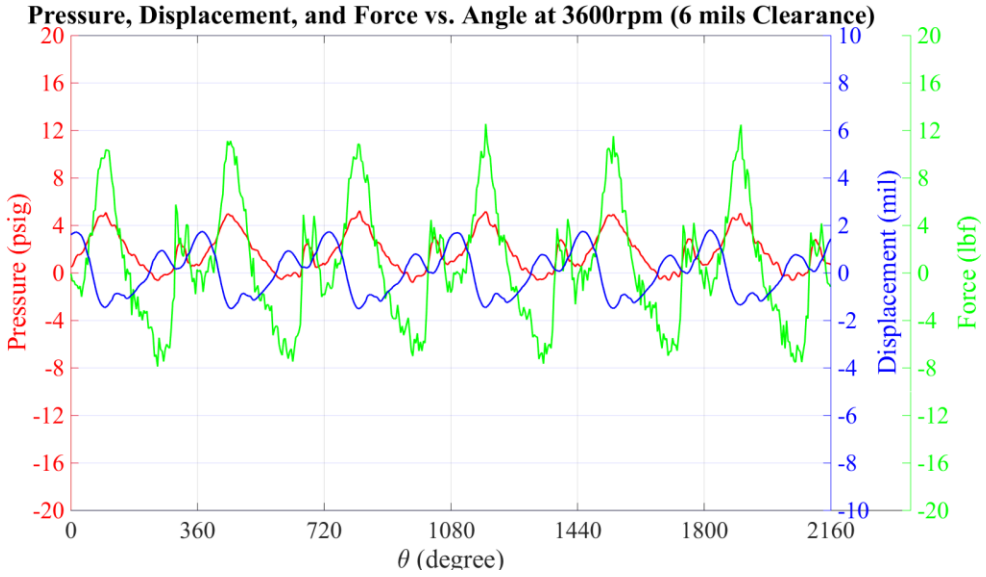

(a) 6 mils, 19 g-in, 0% GVF

Figure 3-10 Pressure, displacement, and force vs. Angle (6 mils, 3600 RPM)

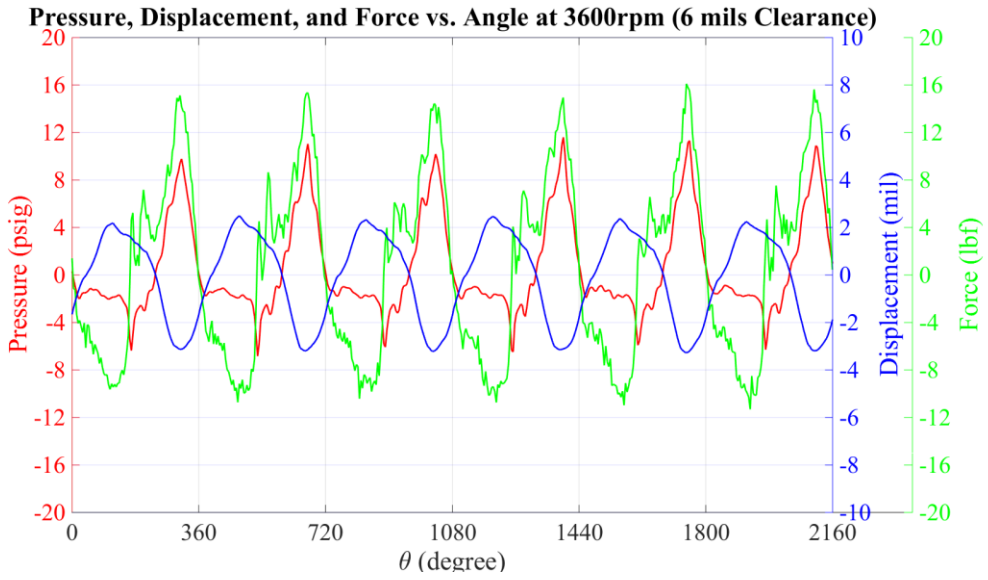

(b) 6 mils, 43 g-in, 0% GVF

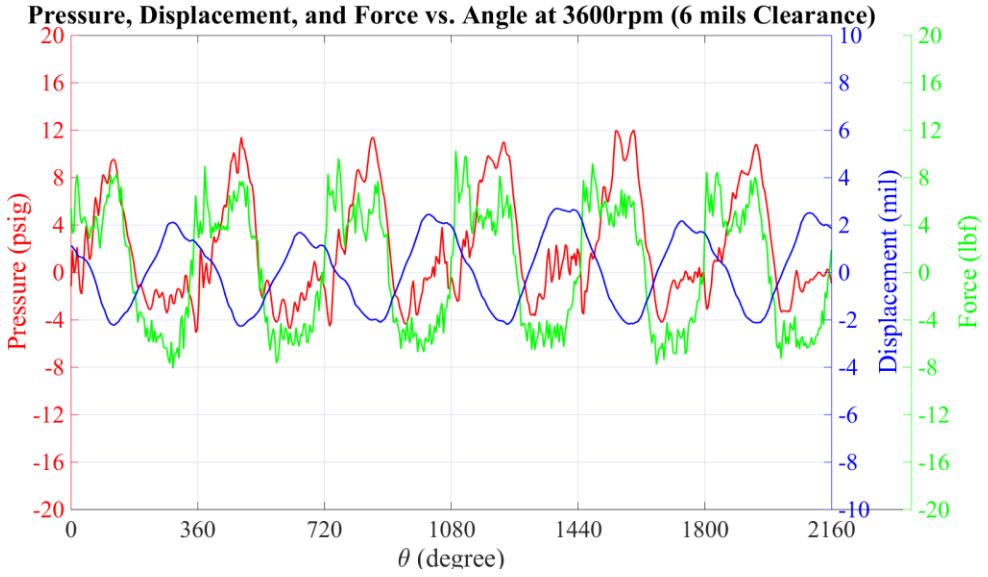

(c) 6 mils, 19 g-in, 30% GVF

Figure 3-10 Continued.

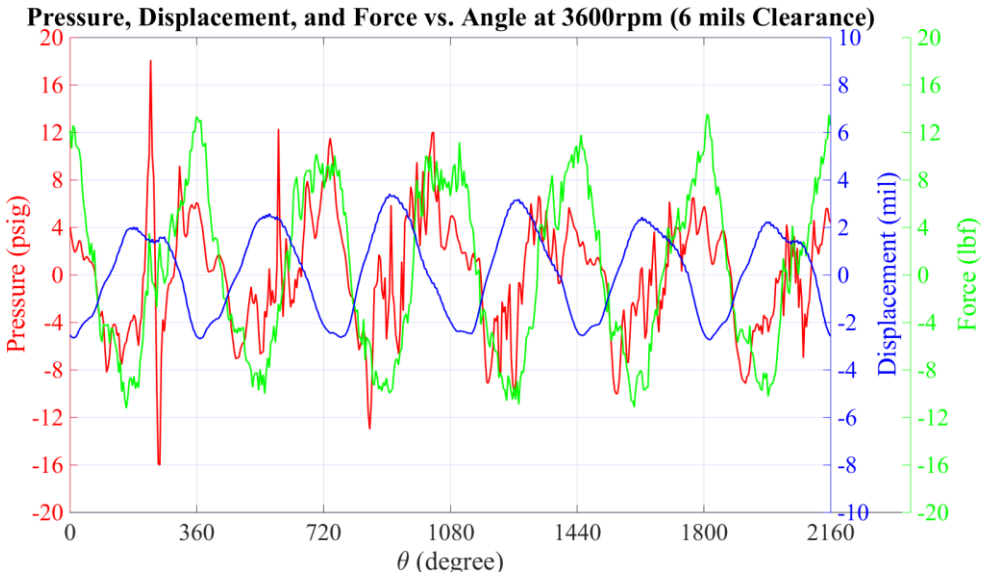

(d) 6 mils, 19 g-in, 60% GVF

Figure 3-10 Continued.

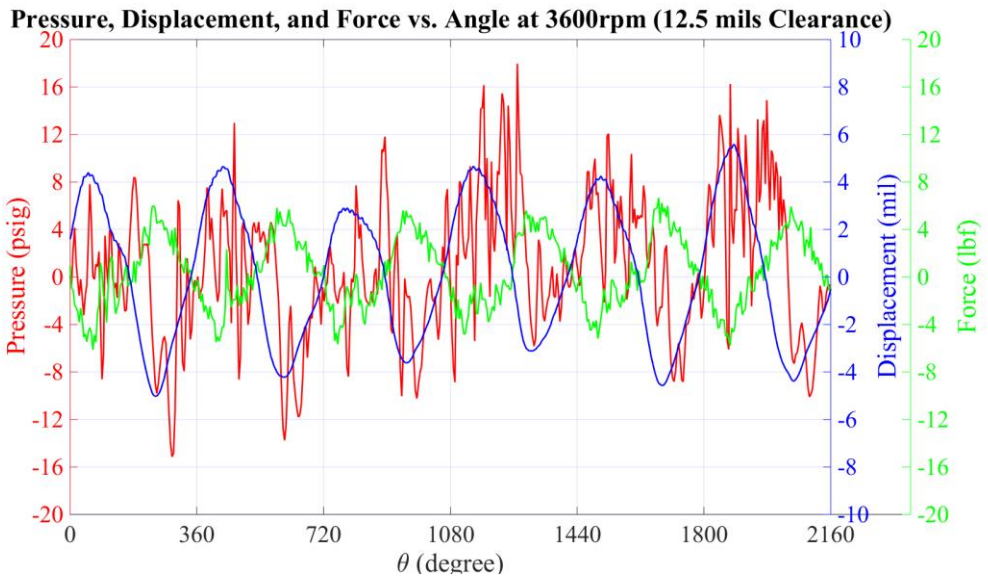

(a) 12.5 mils, 19 g-in, 30% GVF

Figure 3-11 Pressure, displacement, and force vs. Angle (12.5 mils, 3600 RPM)

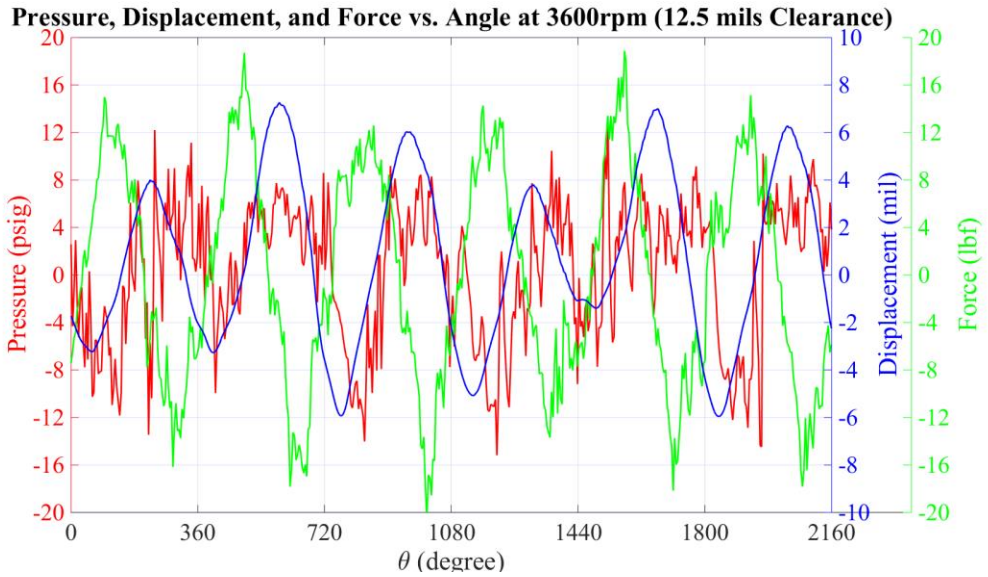

(b) 12.5 mils, 14 g-in, 60% GVF

Figure 3-11 Continued.

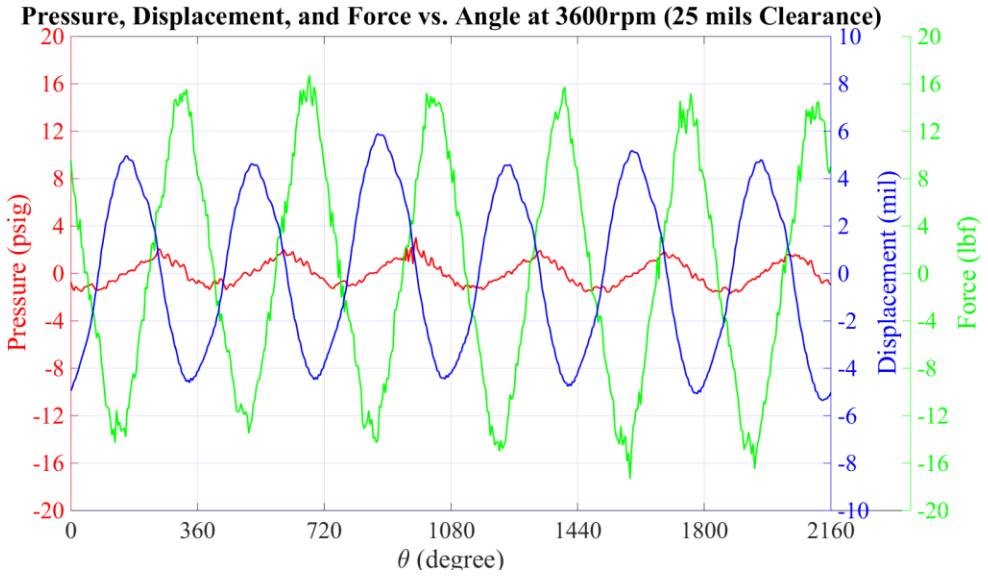

(a) 25 mils, 14 g-in, 0% GVF

Figure 3-12 Pressure, displacement, and force vs. Angle (25 mils, 3600 RPM)

Figure 3-10, Figure 3-11, and Figure 3-12 show that: (1) The pressure and force are in phase for the bearing with 6 mils and 12.5 mils radial clearance. (2) The dynamic

pressure increases with increasing mass imbalance. (3) There are more noises on the pressure and force when running the experiment with air. To show the relationships among the displacements, pressure, and force, a low pass filter with a cut-off frequency at 65 Hz is applied. The comparison among the filtered peak-to-peak amplitudes of the displacement, and pressure for each experiment are shown in Figure 3-13, and Figure 3-14 respectively.

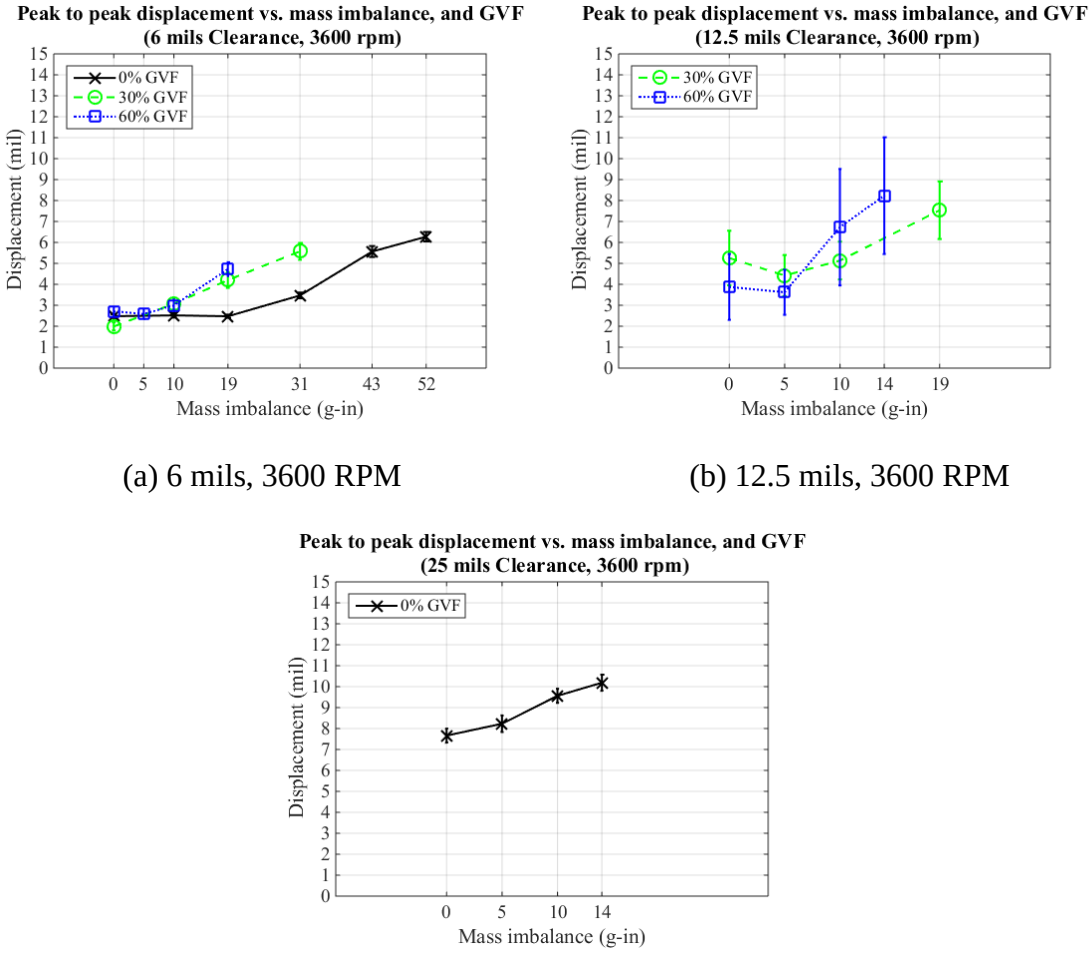

(a) 6 mils, 3600 RPM

(b) 12.5 mils, 3600 RPM

(c) 25 mils, 3600 RPM

Figure 3-13 Peak-to-peak displacement vs. mass imbalance, and GVF

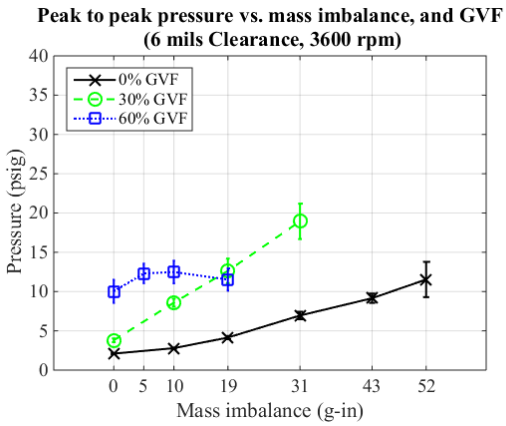

(a) 6 mils, 3600 RPM

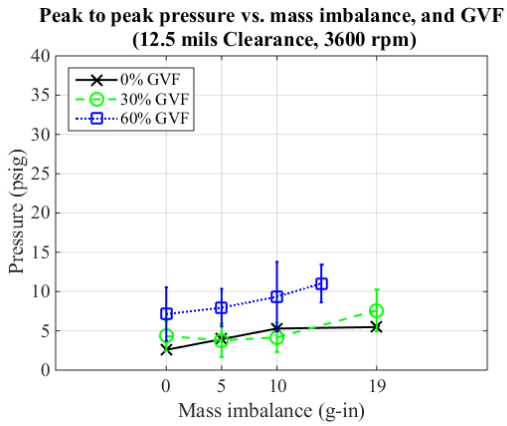

(b) 12.5 mils, 3600 RPM

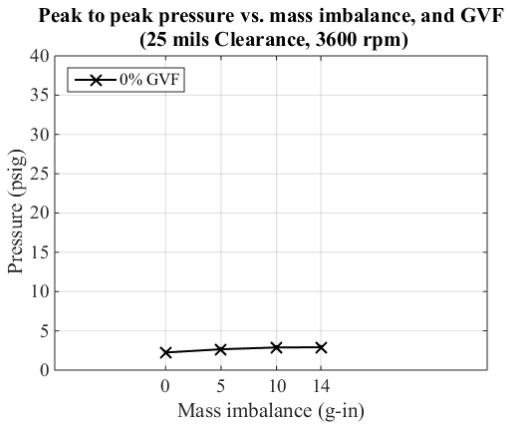

(c) 25 mils, 3600 RPM

Figure 3-14 Peak-to-peak pressure vs. mass imbalance, and GVF

Figure 3-13 is the peak-to-peak displacement with different mass imbalances and GVFs. The experimental result of the 12.5 mils bearing shows the same trend as the orbit radius presented in Figure 3-6. In Figure 3-13 (b), the mean value and the standard deviation of the displacement increases a lot when the mass imbalance is larger than 10 g-in. It is because the increased mass imbalance squeezed the water and air, resulting in noises of the vibration.

Figure 3-14 presents the peak-to-peak pressure with different mass imbalances and GVFs. It shows that:

1) For the 6 mils bearing, the dynamic pressure increases with increases in mass imbalance at 0%, 30%. It is roughly a constant between 10 psi and 13 psi with 60% GVF. It means the fluid film is broken by the air.
2) For the 12.5 mils bearing, the pressure increases with increasing mass imbalances. Compared with the data of 6 mils bearing, the growth rate of the pressure reduces under same experimental conditions.
3) For the 25 mils bearing, the dynamic pressure is roughly a constant with different mass imbalances. The value is less than that of the 6 mils, and 12.5 mils bearing. There are two reasons of this phenomenon. Firstly, the pressure difference between the inlet and outlet of the 25 mils bearing is 30 psi rather than that of the other two bearings, which is 60 psi. Secondly, the motion of the shaft is much less than the radial clearance of the bearing, resulting in a low dynamic pressure.

Besides the amplitude of displacement, force, and pressure, the coherence and phase difference among the displacement, force, and pressure at 60Hz are calculate. The coherence is calculated using Equation (3.1).

$$C_{xy} = \frac{\left|G_{xy}\right|^2}{G_{xx}G_{yy}} \tag{3.1}$$

where:

C_{xy} is the coherence between x and y;

G_{xy} is the cross-spectra density between x and y;

G_{xx}, G_{yy} are the auto-spectral density of x and y respectively.

The value of coherence satisfies $0 \leq C_{xy} \leq 1$. If the coherence is equal to 1, it is an indication that $x(t)$ and $y(t)$ are completely linear related. Otherwise, if the coherence is equal to zero, it is an indication that $x(t)$ and $y(t)$ are completely unrelated.

The coherences among the displacement, pressure, and force are shown in Figure 3-15.

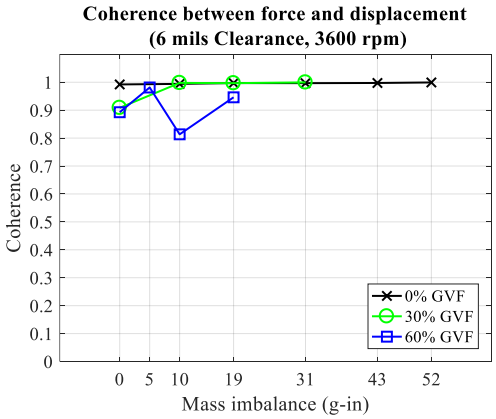

(a) 6 mils, 3600 RPM

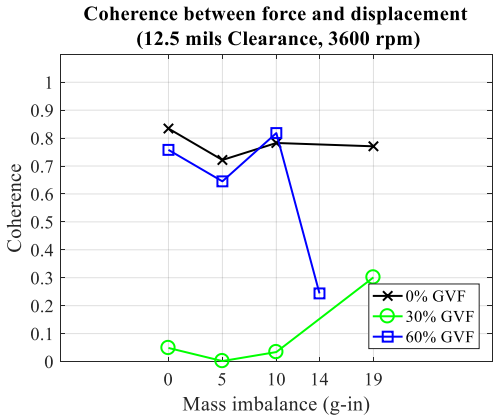

(b) 12.5 mils, 3600 RPM

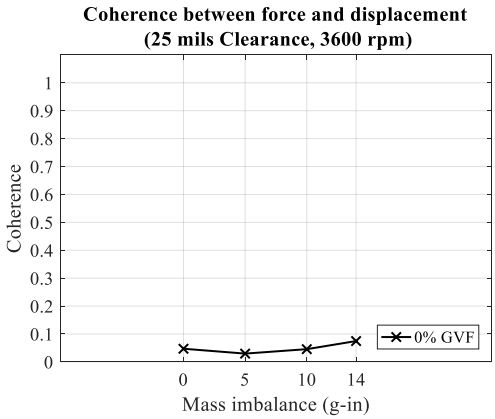

(c) 25 mils, 3600 RPM

Figure 3-15 Coherence between force and displacement

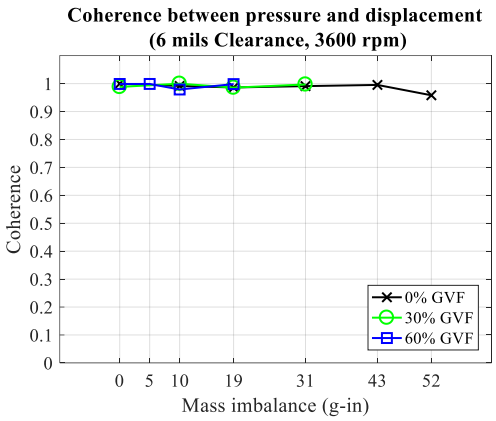

(a) 6 mils, 3600 RPM

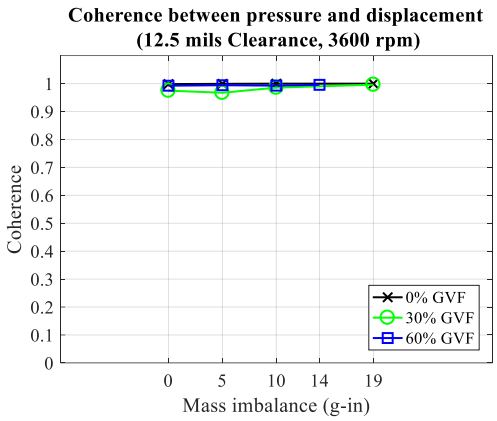

(b) 12.5 mils, 3600 RPM

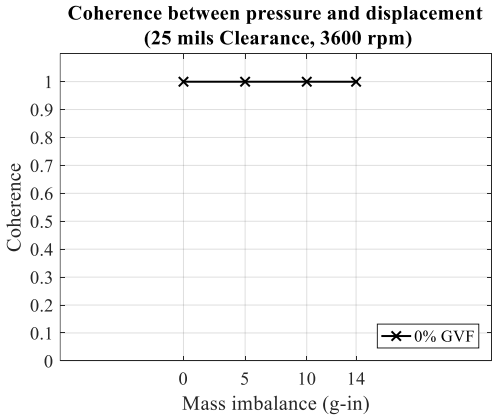

(c) 25 mils, 3600 RPM

Figure 3-16 Coherence between pressure and displacement

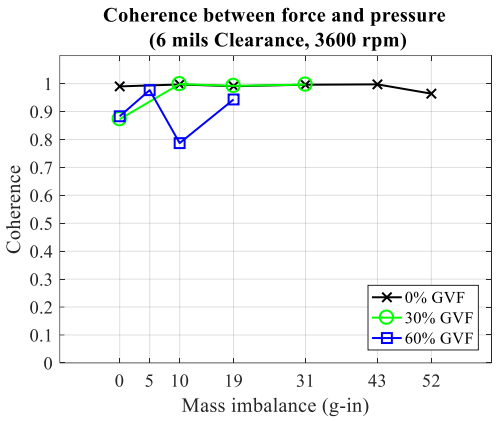

(a) 6 mils, 3600 RPM

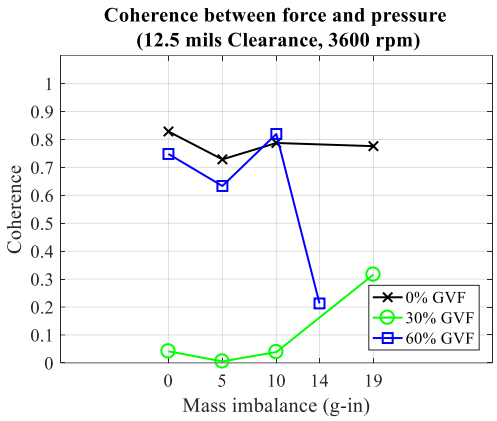

(b) 12.5 mils, 3600 RPM

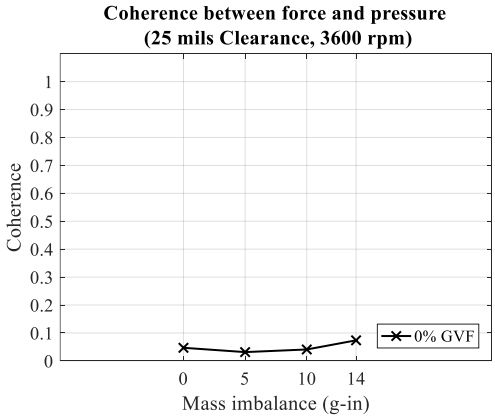

(c) 25 mils, 3600 RPM

Figure 3-17 Coherence between force and pressure

Figure 3-15, Figure 3-16, and Figure 3-17 show that:

1) For the bearing with 6 mils radial clearance, the coherences among displacement, force, and pressure are close to 1 under different experimental conditions. The fluctuation of the coherence increases with increases in GVF.
2) For the bearing with 12.5 mils radial clearance, the coherence between pressure and displacement is 1 for all the experimental conditions. Regarding to the coherence related to force, the value is close to 0.8 with 0% and 60 %GVF,

which is acceptable considering the noise with 60% GVF. But the coherence related to force of the data with 30% GVF is too small, showing there is no relation at 60Hz.

3) For the bearing with 12.5 mils radial clearance, the coherences between force and pressure are close to 0. Since the load capacity decreases with increases in bearing clearance, the hydraulic force is smaller than that of the other two bearing with the same mass imbalance.

Figure 3-18, Figure 3-19, and Figure 3-20 show the leading phase of the force relative to the minimum displacement, the leading phase of the pressure relative to the minimum displacement, the leading phase of the force relative to the dynamic pressure at 3600 RPM respectively. Only the data showing good coherence value are presented in the figures. Since the sampling frequency is 5 KHz, the phase resolution at 3600 RPM is 4.32°.

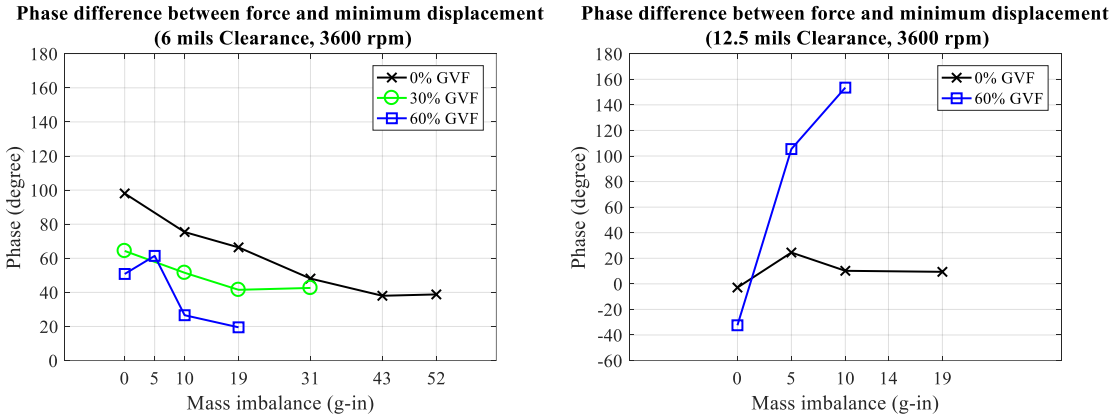

(a) 6 mils, 3600 RPM (b) 12.5 mils, 3600 RPM

Figure 3-18 Phase difference between force and minimum displacement

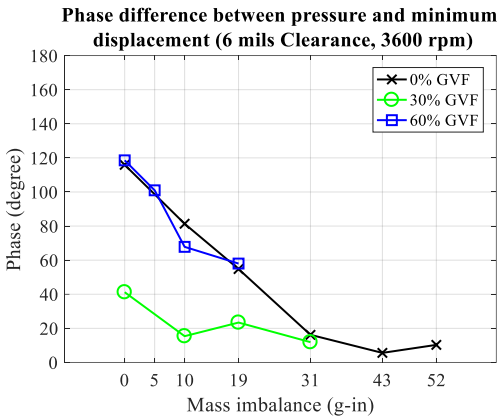

(a) 6 mils, 3600 RPM

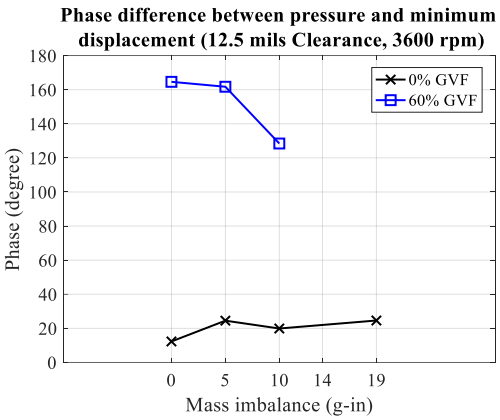

(b) 12.5 mils, 3600 RPM

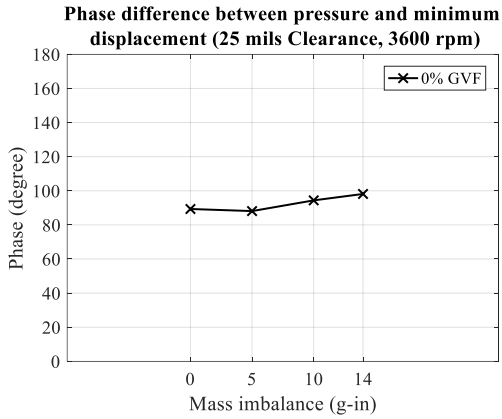

(b) 25 mils, 3600 RPM

Figure 3-19 Phase difference between pressure and minimum displacement

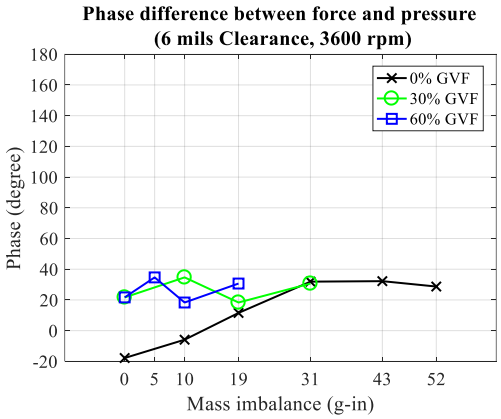

(a) 6 mils, 3600 RPM

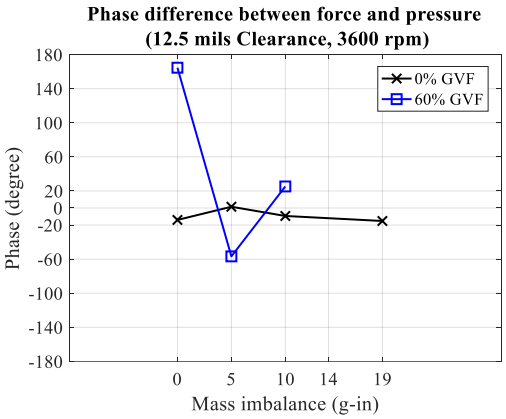

(b) 12.5 mils, 3600 RPM

Figure 3-20 Phase difference between force and pressure

The phase difference between force and minimum displacement in Figure 3-18 shows that:

1) For the 6 mils bearing, the leading phase of the force relative to the minimum displacement decreases with increasing mass imbalances as well as the GVF. The leading phase decreases from 100° to 40° with 0% GVF. It decreases from 60° to 40° with 30% GVF, and from 50° to 20° with 60% GVF. It shows the effect of eccentricity on the whirl, resulting in the changes of the leading phase.
2) For the 12.5 mils bearing, the phase difference is roughly a constant at 0% GVF. The phase difference increases from -40° to 160° with increasing mass imbalance with 60% GVF. The air breaks the fluid film resulting in the phase changes.

The phase difference between pressure and minimum displacement in Figure 3-19 shows:

1) For the 6 mils bearing, the leading phase of the pressure relative to the minimum displacement decreases with increasing mass imbalances. The phase difference decreases from 120° to 10° with 0% GVF. It decreases from 40° to 20°, and stays at 20° as a constant, when the GVF is 30%. The changing rate of the phase difference with 60% GVF is same as that of the test with 0% GVF. The phase stops changing when the mass imbalance is large enough. For the test with 0% GVF, the value is 31 g-in, while for the 30% GVF test, the value is 10 g-in.

2) For the 12.5 mils bearing, the phase difference is a constant (20º) with 0% GVF, which means the force and the minimum displacement are in phase. As shown in Figure 3-11, noises occur after adding the air. The phase decreases from 160º to 130° with 60% GVF, while the phase decreases from 120° to 60° for the 6 mils bearing with the same experimental conditions. Compared with the 6 mils bearing, the 12.5 mils bearing has a larger clearance, which allows more air in the clearance. The pressure of the mixed flow is measured resulting in the noise in the spectrum and a relative large phase difference.
3) For the 25 mils bearing, the pressure leads the minimum displacement with a constant value (roughly 90°).

The phase difference between force and pressure presented in Figure 3-20 shows:

1) For 6 mils bearing, the phase increases with increasing the mass imbalance. It reaches a constant (30°) when the mass imbalance is greater than 31 g-in with 0% GVF. The phase is roughly a constant at 30° with 30% and 60% GVF. Considering the phase resolution (4.32° at 3600 RPM), the force and pressure are in phase.
2) For the 12.5 mils bearing, the force and pressure are in phase (roughly 0°) with 0% GVF. The phase at 60 % GVF changes from 160° to 20°, which is caused by the noises induced by the air.

In this chapter, bearings with different clearance are tested under different disk mass imbalances and GVFs. The experimental results verify the design of the test rig. It is also shown that: (1) The load capacity of the bearing decreases with increasing clearance.

(2) The air breaks the fluid film in the clearance resulting in the load capacity reduction, and vibration noise increase. (3) The effects of imbalance forces, and GVFs on the phase difference between the displacement, force, and pressure.

4. SIMULATION AND ANALYSIS

Computational Fluid Dynamics (CFD) is the science of predicting fluid flow, and related phenomena by solving a set of governing equations. FLUENT is a commercial CFD program developed by ANSYS. It can perform multi-physics analysis, including fluid forces, thermal effects, structural integrity and electromagnetic radiation. In this chapter, quasi-steady CFD simulations are conducted to study the flow in bearing clearances firstly. Then transient simulations of the entire vertical rotor-bearing system are conducted based on a proposed FSI method using Fluent and MATLAB, as well as an optimized FSI method respectively.

4.1 Quasi-Steady CFD Simulation

The schematic of the journal bearing's geometry is shown in Figure 4-1. In ESP applications, the journal bearing not only supports the shaft but also prevents the fluid leakage between stages. They are called annular seals in other applications generally.

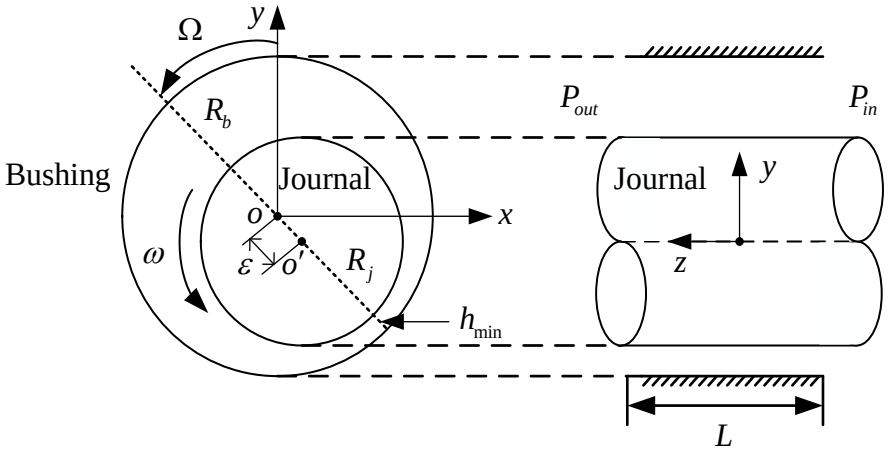

Figure 4-1. Schematic of the journal bearing's geometry

In Figure 4-1:

o is the origin of the bushing (stator);

o' is the origin of the journal (rotor);

ε is the eccentricity of the journal;

ω is the angular velocity of the journal;

Ω is the angular velocity of the whirl of the journal;

R_b and R_j are the radius of the bushing and journal respectively;

L is the length of the bearing;

h_{min} is the minimum clearance;

P_{in} and P_{out} are the pressure at the inlet and outlet of the bearing respectively.

The pressure distribution in the fluid film of the journal bearing is related to the rotordynamic parameters (stiffness, damping ratio, etc.), which is important for the dynamic analysis of the rotor-bearing system. The governing equations of the incompressible fluid (the density is a constant) are the continuity equation and the Navier-Stokes equations, which are presented in Equation (4.1) and Equation (4.2) respectively.

$$\nabla \bullet \mathbf{u} = 0 \tag{4.1}$$

where $\mathbf{u}$ is the velocity vector.

$$\rho \frac{D\mathbf{u}}{Dt} = -\nabla p + \rho \mathbf{g} + \mu \nabla^2 \mathbf{u} \tag{4.2}$$

where:

ρ is the fluid density;

$\mathbf{u}$ is the velocity vector;

P is the pressure;

$\mathbf{g}$ is the inertial force vector;

μ is the viscosity.

In this section, Quasi-Steady CFD simulations are conducted to study the flow in the bearing clearance.

4.1.1 Quasi-Steady CFD Simulation Setup

The simulation is conducted on three bearings with different radial clearances. These dimensions are listed in Table 4-1:

Table 4-1 Parameters of the journal bearings

Parameter	Value
Journal outside diameter	0.0475 m (1.869 in); 0.0471 m (1.856 in);0.0465 m (1.831 in)
Bushing inside diameter	0.0478 m (1.881 in)
Radial clearance	152.4 μm (0.006 in); 304.8 μm (0.012 in); 635 μm (0.025 in)
Bearing length	0.0381 m (1.5 inch)
Lubricant	Water
Lubricant density	1000 kg/m^3
Inlet gauge pressure	0.345 MPa (50 psi)
Outlet gauge pressure	0
Spin speed of the rotor	3600 RPM (376.99 rad/s)

Simulations are conducted with different eccentricity ratios to study their effects on the flow in the bearing clearance. The eccentricity ratio starts from 0 with an interval of 0.1. The maximum eccentricity ratio depends on the converging status of each simulation. The coordinate in the simulation is shown in Figure 4-2. The gird independent studies of each bearing are shown in Table 4-2, Table 4-3, and Table 4-4.

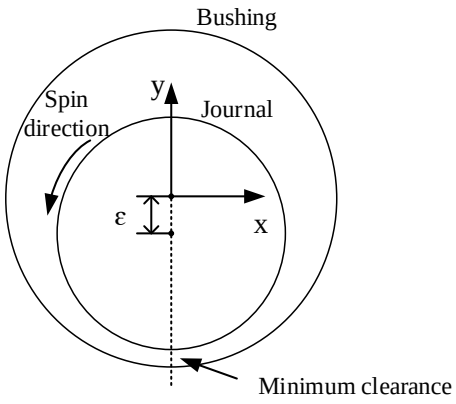

Figure 4-2 Coordinate in the simulation

Table 4-2 Mesh independence study results (6 mils radial clearance, $\varepsilon = 0.9$)

No.	No. of elements	F_x (N)	F_y (N)	Minimum y+	Maximum y+	Relative deviation for F_x (%)	Relative deviation for F_y (%)
1	8000	133.61	27.81	0.0739	3.062	4.3248	34.4883
2	32000	138.69	42.69	0.0515	3.267	0.6875	0.5543
3	128000	138.87	41.39	0.0402	3.591	0.5628	2.5051
4	**200000**	**139.49**	**42.19**	**0.0375**	**3.7250**	**0.1145**	**0.6414**
5	288000	139.53	41.95	0.0321	3.8460	0.0893	1.1946
6	324000	140.61	41.16	0.0436	4.7450	0.6836	3.0645
7	583200	140.65	41.30	0.0312	5.2640	0.7102	2.7271
8	648000	139.60	42.15	0.0276	4.1580	0.0396	0.7156
9	1012000	139.62	42.26	0.0230	4.3370	0.0264	0.4715
10	1568000	139.65	42.46	0.0208	4.5710	0.0000	0.0000

Table 4-3 Mesh independence study results (12.5 mils radial clearance, $\varepsilon = 0.9$)

No.	No. of elements	F_x (N)	F_y (N)	Minimum y+	Maximum y+	Relative deviation for F_x (%)	Relative deviation for F_y (%)
1	11200	39.19	60.91	0.0446	3.7003	3.2601	4.7701
2	44800	38.04	63.61	0.0475	4.0220	0.2171	0.5486
3	179200	38.69	62.86	0.0481	4.4683	1.9236	1.7280
4	260000	39.07	62.42	0.0531	5.1732	2.9415	2.4013
5	**280000**	**38.46**	**63.12**	**0.0436**	**4.1862**	**1.3301**	**1.3116**
6	340000	37.89	63.86	0.0243	2.2833	0.1708	0.1529
7	403200	38.74	62.87	0.0480	4.7953	2.0572	1.7103
8	489600	37.92	63.86	0.0243	2.3567	0.1054	0.1528
9	907200	38.80	63.00	0.0480	5.1590	2.2098	1.5040
10	1101600	37.96	63.96	0.0243	2.5424	0.0000	0.0000

Table 4-4 Mesh independence study results (25 mils radial clearance, $\varepsilon = 0.9$)

No.	No. of elements	F_x (N)	F_y (N)	Minimum y+	Maximum y+	Relative deviation for F_x (%)	Relative deviation for F_y (%)
1	13600	3.74	74.82	0.0566	4.2520	25.6739	1.9911
2	54400	4.36	76.47	0.0600	4.6580	13.2866	0.1768
3	217600	5.05	76.84	0.0608	5.1660	0.3950	0.6561
4	324000	4.05	79.17	0.3096	24.4400	19.5625	3.7051
5	**340000**	**5.03**	**76.56**	**0.0609**	**5.3470**	**0.0063**	**0.2915**
6	489600	5.05	76.56	0.0608	5.5000	0.2570	0.2883
7	777600	5.63	76.12	0.1629	14.6100	11.8289	0.2921
8	972000	5.87	75.08	0.0895	8.5150	16.6002	1.6465
9	1101600	5.03	76.34	0.0608	5.8690	0.0000	0.0000

In Table 4-2, Table 4-3, and Table 4-4, the rows with bold numbers show the mesh chosen for the simulation. It shows that the maximum y+ is around 5 based on the chosen mesh. Because the maximum clearance occurs when the eccentricity ratio is 0.9 and the number of divisions in the bearing clearance is same, the maximum y+ is reduced in the

simulation with smaller eccentricity ratios. The mesh independence study on the bearings without eccentricity shows that the maximum y+ is 2.5.

4.1.2 Quasi-Steady CFD Simulation Results

The pressure contours with different eccentricity ratios at 3600 RPM for the three journal bearings are presented. The pressures are gauge pressures in the figures. The minimum clearance and the spin speed are marked in the subfigure (i) of Figure 4-3, Figure 4-4, and Figure 4-5.

4.1.2.1 Simulation results of the bearing with 6 mils radial clearance

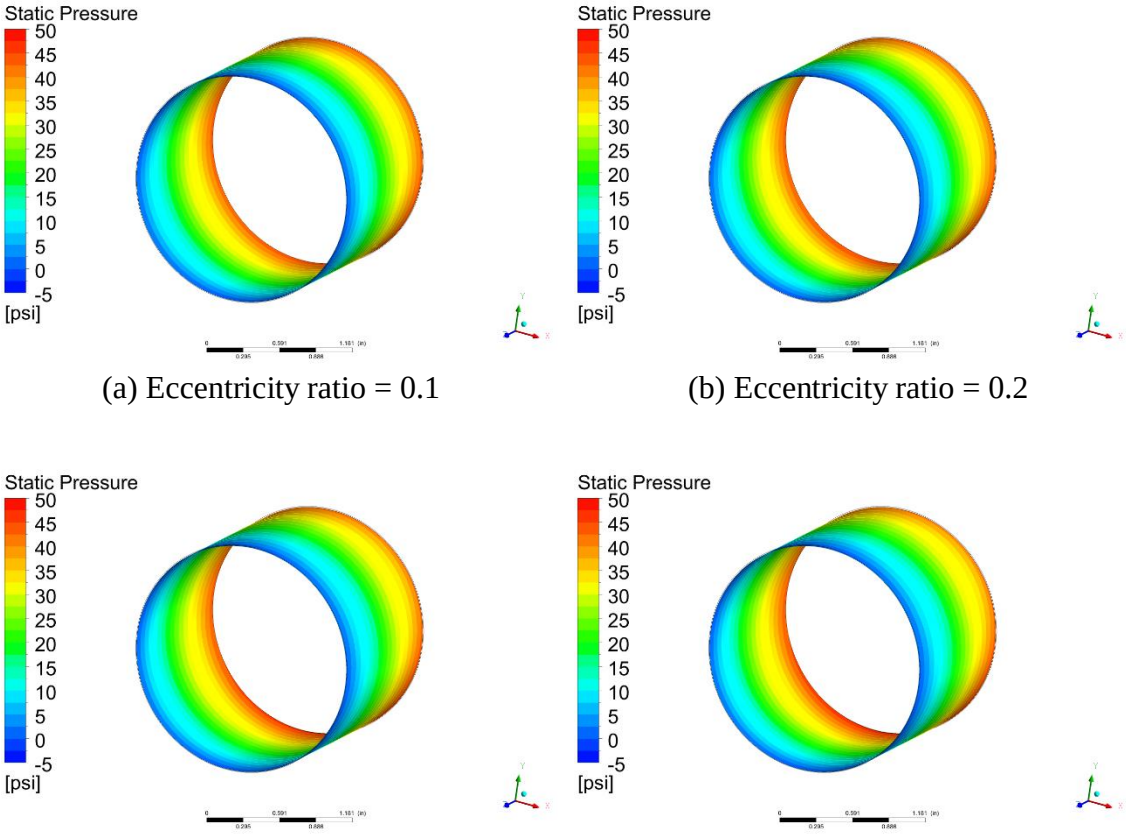

(a) Eccentricity ratio = 0.1 (b) Eccentricity ratio = 0.2

(c) Eccentricity ratio = 0.3 (d) Eccentricity ratio = 0.4

Figure 4-3 Pressure contours at 3600 RPM (6 mils radial clearance)

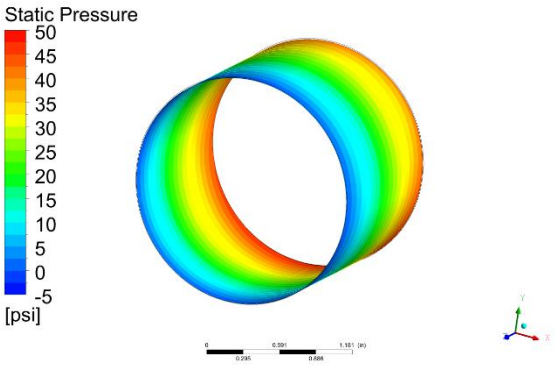

(e) Eccentricity ratio = 0.5

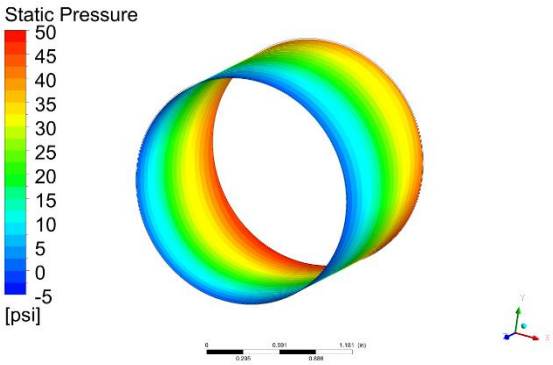

(f) Eccentricity ratio = 0.6

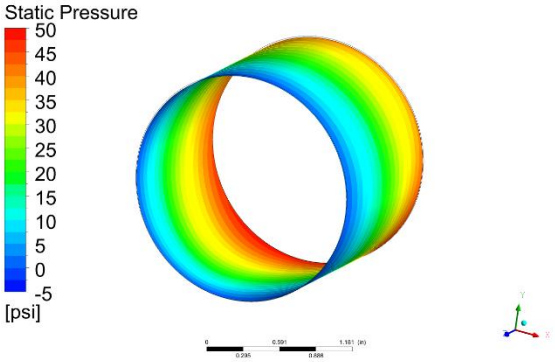

(g) Eccentricity ratio = 0.7

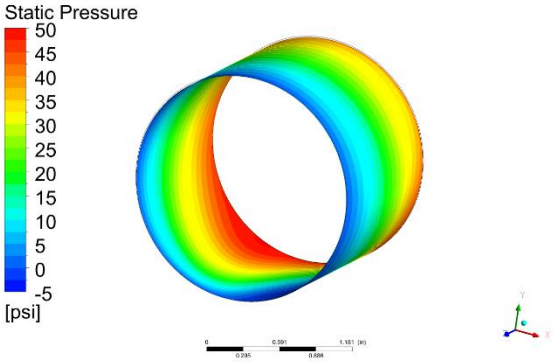

(h) Eccentricity ratio = 0.8

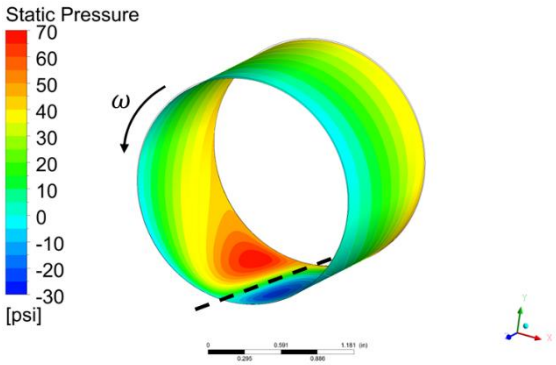

(i) Eccentricity ratio = 0.9

Figure 4-3 Continued.

The pressure contours shown in Figure 4-3 show that:

1) The pressure decreases linearly from the inlet to the outlet when the eccentricity ratio is less than or equal to 0.6. Because the clearance difference caused by the eccentricity is not large enough.
2) When the eccentricity ratio is greater than 0.6, the liquid in the converging zone (the zone before the minimum clearance) is squeezed and a high-pressure zone is formed. The liquid in the diverging zone (the zone after the minimum clearance) forms a low-pressure zone.
3) The pressure contours are uniform circles, which are parallel to the inlet and outlet boundaries, when the eccentricity ratio is less than or equal to 0.6. When the eccentricity ratio is greater than 0.6, the pressure contours show that the high-pressure zone and low-pressure zone approach to the minimum clearance with increases in the eccentricity ratio. It results in the changes of the phase difference between the hydraulic force and the minimum clearance.

The hydraulic forces generated by the fluid film with full and half Sommerfeld boundary conditions (the negative pressure is forced to be the ambient pressure), and the relative angle to the minimum clearance are shown in Table 4-5.

Table 4-5 Hydraulic forces at 3600 RPM (6 mils radial clearance)

	Full Sommerfeld				Half Sommerfeld			
ε	F_x (lb.)	F_y (lb.)	F_{total} (lb.)	θ (°)	F_x (lb.)	F_y (lb.)	F_{total} (lb.)	θ (°)
0.1	0.20	2.27	2.27	84.99	0.20	2.26	2.27	84.96
0.2	1.33	3.10	3.37	66.84	1.31	3.09	3.36	67.05
0.3	1.63	5.41	5.66	73.21	1.62	5.39	5.63	73.30
0.4	3.43	5.90	6.83	59.80	3.40	5.88	6.79	59.97
0.5	5.56	6.40	8.48	49.04	5.50	6.38	8.42	49.22
0.6	7.66	8.21	11.22	46.99	7.61	8.18	11.17	47.06
0.7	11.57	8.29	14.23	35.63	11.51	8.26	14.17	35.67
0.8	18.08	9.36	20.36	27.36	17.93	9.62	20.35	28.22
0.9	31.78	9.61	33.20	16.83	29.46	16.05	33.55	28.58

The hydraulic forces shown in Table 4-5 shows that:

1) The force in x and y direction increase with increases in eccentricity ratio.
2) The force in the x direction is greater than that in the y direction, when the eccentricity ratio is greater than 0.6. This means the cross-coupled component plays a more significant role.
3) When the eccentricity ratio is less than 0.8, the forces calculated with full Sommerfeld and half Sommerfeld are similar. The difference occurs with the eccentricity of 0.9, especially the force in y direction.

4.1.2.2 Simulation results of the bearing with 12.5 mils radial clearance

The pressure contours and forces of the bearing with 12.5 mils clearance are shown in Figure 4-4 and Table 4-6 respectively.

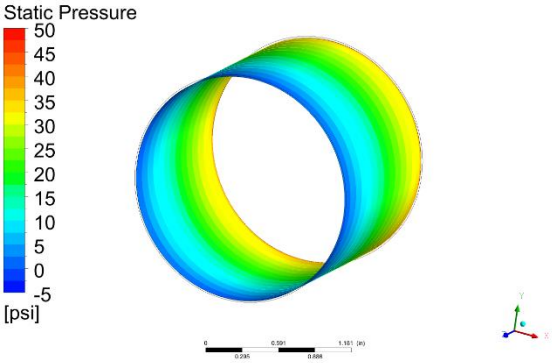

(a) Eccentricity ratio = 0.1

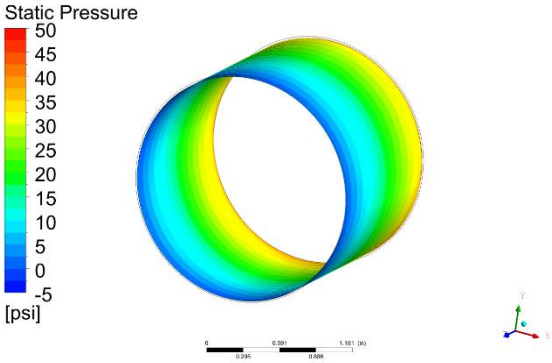

(b) Eccentricity ratio = 0.2

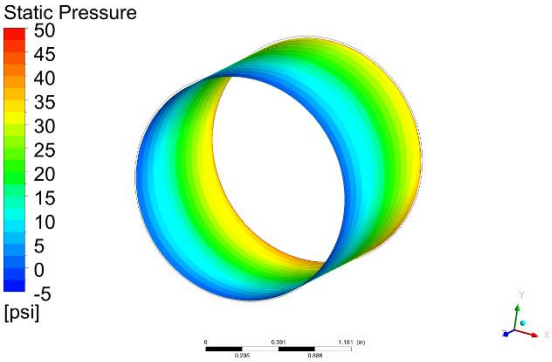

(c) Eccentricity ratio = 0.3

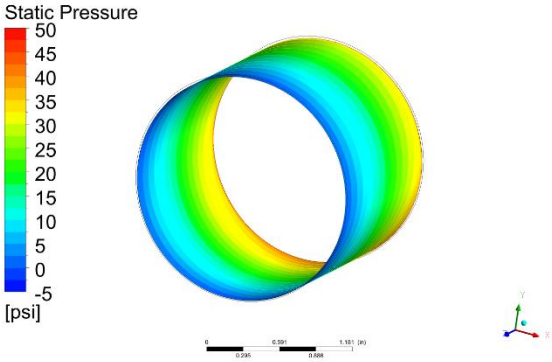

(d) Eccentricity ratio = 0.4

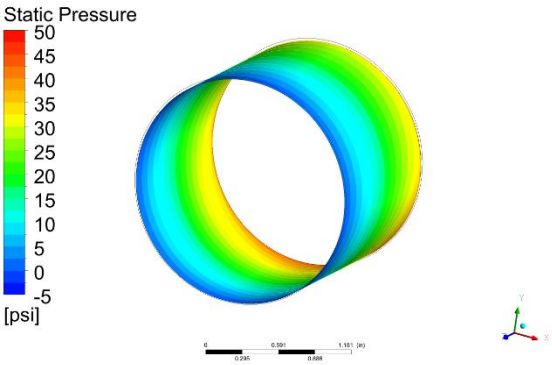

(e) Eccentricity ratio = 0.5

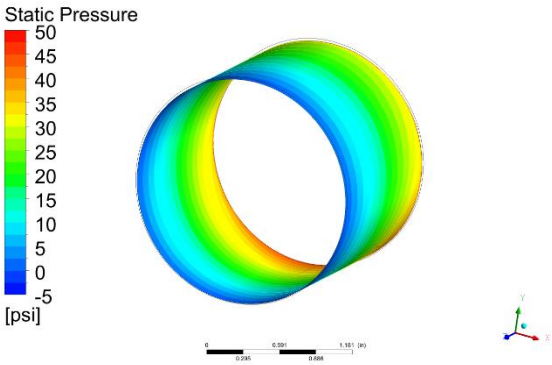

(f) Eccentricity ratio = 0.6

Figure 4-4 Pressure contours at 3600 RPM (12.5 mils radial clearance)

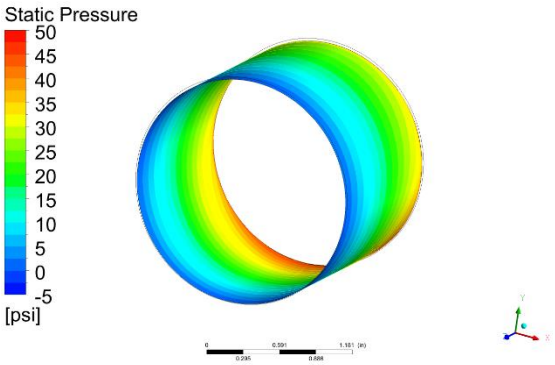

(g) Eccentricity ratio = 0.7

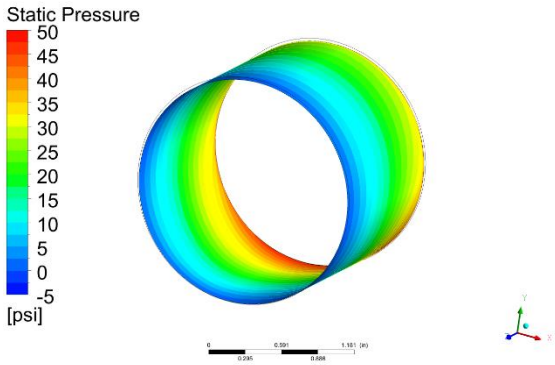

(h) Eccentricity ratio = 0.8

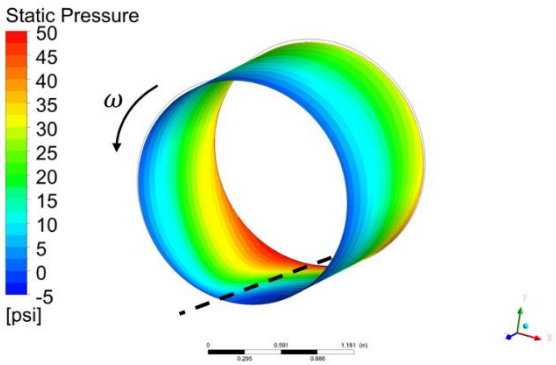

(i) Eccentricity ratio = 0.9

Figure 4-4 Continued.

Table 4-6 Hydraulic forces at 3600 RPM (12.5 mils radial clearance)

	Full Sommerfeld				Half Sommerfeld			
ε	F_x (lb.)	F_y (lb.)	F_{total} (lb.)	θ (°)	F_x (lb.)	F_y (lb.)	F_{total} (lb.)	θ (°)
0.1	-0.07	2.01	2.01	91.96	-0.08	2.00	2.00	92.25
0.2	-0.13	4.03	4.03	91.85	-0.15	4.01	4.01	92.14
0.3	-0.17	6.02	6.02	91.60	-0.20	5.99	6.00	91.90
0.4	-0.15	7.97	7.97	91.09	-0.19	7.93	7.93	91.40
0.5	-0.02	9.83	9.83	90.12	-0.07	9.78	9.78	90.43
0.6	0.36	11.53	11.53	88.20	0.30	11.48	11.48	88.53
0.7	1.30	12.98	13.04	84.30	1.21	12.92	12.98	84.63
0.8	3.45	13.99	14.41	76.13	3.36	13.93	14.33	76.43
0.9	8.65	14.19	16.62	58.65	8.52	14.30	16.65	59.22

The pressure contours shown in Figure 4-4 show that:

1) The pressure changes almost linearly from the inlet to the outlet, when the eccentricity ratio is less than or equal to 0.7.
2) When the eccentricity ratio is 0.9, the high-pressure zone and low-pressure zone are not as obvious as those of the bearing with 6 mils radial clearance. This is because the minimum film thickness is greater than that of the bearing with 6 mils radial clearance.

The hydraulic forces shown in Table 4-6 show that:

1) The force in x direction has no changes when the eccentricity ratio is smaller than or equal to 0.5. It increases with increasing the eccentricity ratio when the eccentricity ratio is greater than 0.6.
2) The force in y direction increases with increasing eccentricity ratio.
3) When the eccentricity ratio is 0.9, the force in x direction is less than that in y direction. It means the direct component plays a more significant role.

4.1.2.3 Simulation results of the bearing with 25 mils radial clearance

The pressure contours and hydraulic forces of the bearing with 25 mils clearance are shown in Figure 4-5 and Table 4-7 respectively.

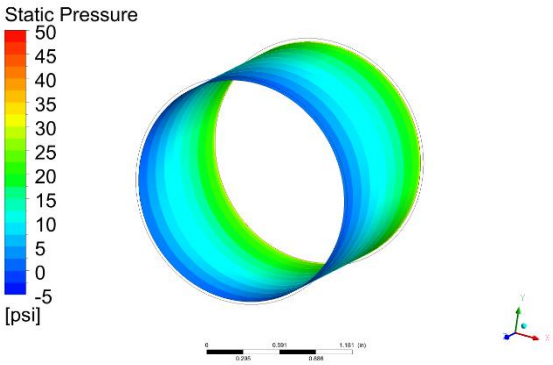

(a) Eccentricity ratio = 0.1

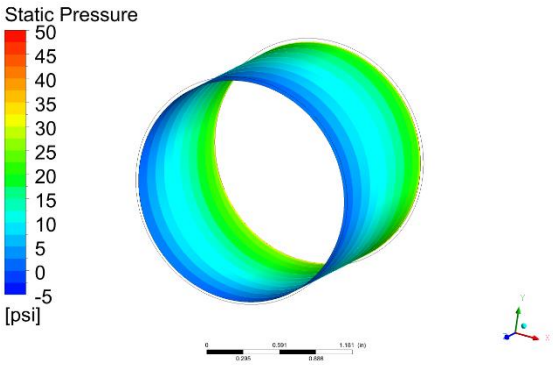

(b) Eccentricity ratio = 0.2

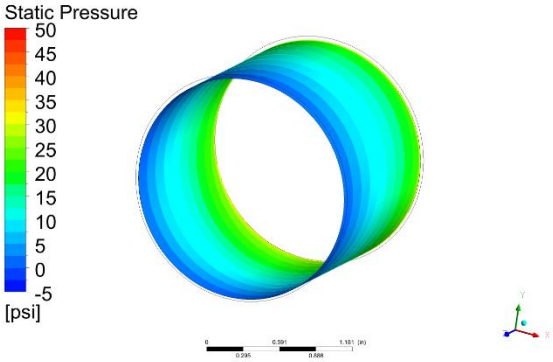

(c) Eccentricity ratio = 0.3

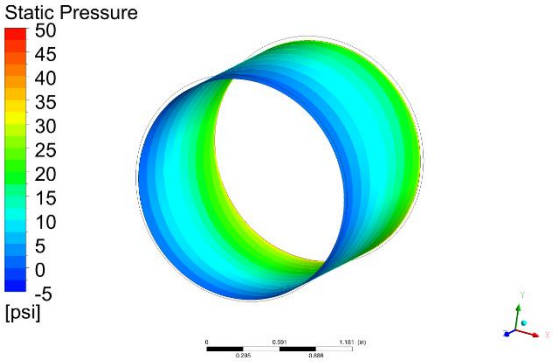

(d) Eccentricity ratio = 0.4

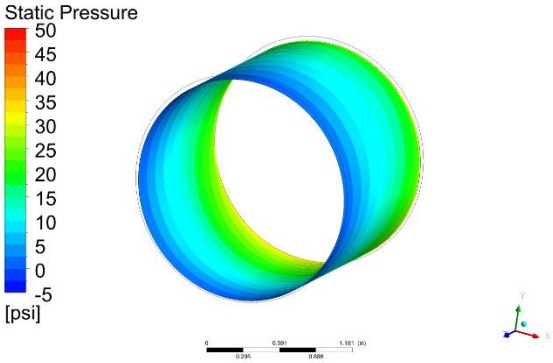

(e) Eccentricity ratio = 0.5

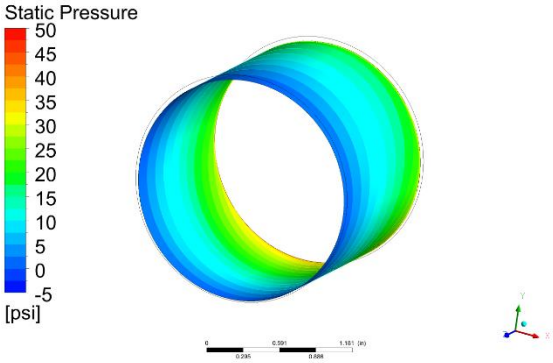

(f) Eccentricity ratio = 0.6

Figure 4-5 Pressure contours at 3600 RPM (25 mils radial clearance)

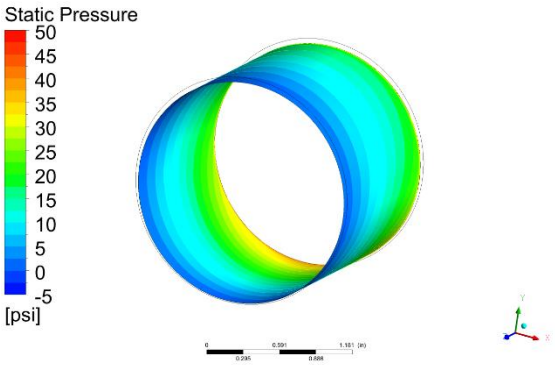

(g) Eccentricity ratio = 0.7

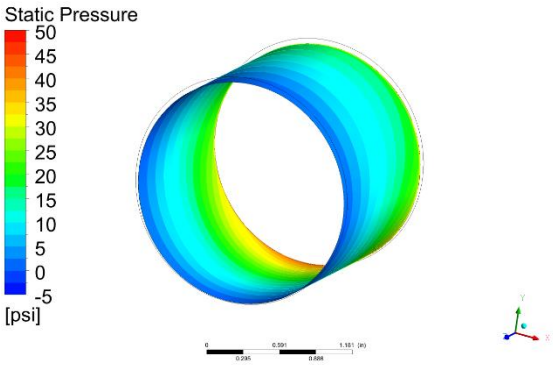

(h) Eccentricity ratio = 0.8

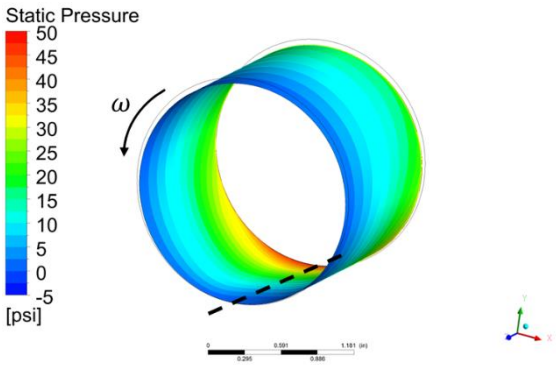

(i) Eccentricity ratio = 0.9

Figure 4-5 Continued.

Table 4-7 Hydraulic forces at 3600 RPM (25 mils radial clearance)

	Full Sommerfeld				Half Sommerfeld			
ε	F_x (lb.)	F_y (lb.)	F_{total} (lb.)	θ (°)	F_x (lb.)	F_y (lb.)	F_{total} (lb.)	θ (°)
0.1	-0.07	2.06	2.06	91.93	-0.07	2.05	2.06	92.00
0.2	-0.14	4.13	4.14	91.94	-0.15	4.12	4.12	92.02
0.3	-0.22	6.22	6.22	91.99	-0.22	6.19	6.20	92.08
0.4	-0.30	8.33	8.34	92.08	-0.32	8.30	8.31	92.18
0.5	-0.41	10.49	10.50	92.22	-0.43	10.45	10.46	92.35
0.6	-0.54	12.69	12.70	92.42	-0.57	12.63	12.65	92.58
0.7	-0.67	14.82	14.84	92.61	-0.72	14.76	14.78	92.79
0.8	-0.59	16.58	16.59	92.04	-0.65	16.51	16.52	92.27
0.9	1.14	17.23	17.27	86.22	1.06	17.16	17.19	86.48

The pressure contours shown in Figure 4-5 show that:

1) The pressure changes linearly from the inlet to the outlet, when the eccentricity ratio is less than or equal to 0.8.
2) When the eccentricity ratio is 0.9, the high-pressure zone and low-pressure zone are not as obvious as those of the other two bearings. This is because the minimum film thickness is greater than that of the other bearings.

The hydraulic forces shown in Table 4-7 show that:

1) The forces in x direction and y direction are small for all the eccentricity ratios.
2) The forces in y direction increases along with increases in the eccentricity ratio. When the eccentricity ratio is 0.9, the force in y direction is greater than that of the other bearings.
3) When the eccentricity ratio is 0.9, the force in x direction is less than that in y direction. It means the direct component is more significant.

To compare the simulation results of the hydraulic force of the three bearings, the comparison between the total force, and phase difference relative to the minimum clearance are shown in Figure 4-6 and Figure 4-7.

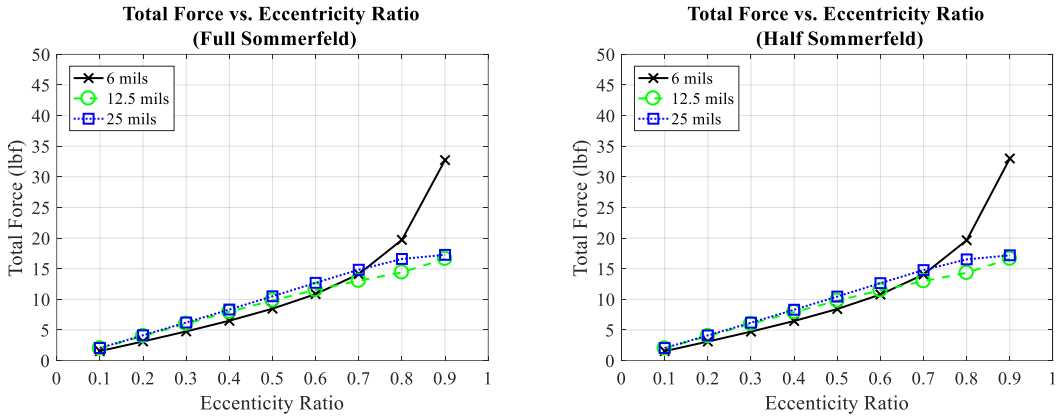

(a) Full Sommerfeld (b) Half Sommerfeld

Figure 4-6 Total force vs. eccentricity ratio

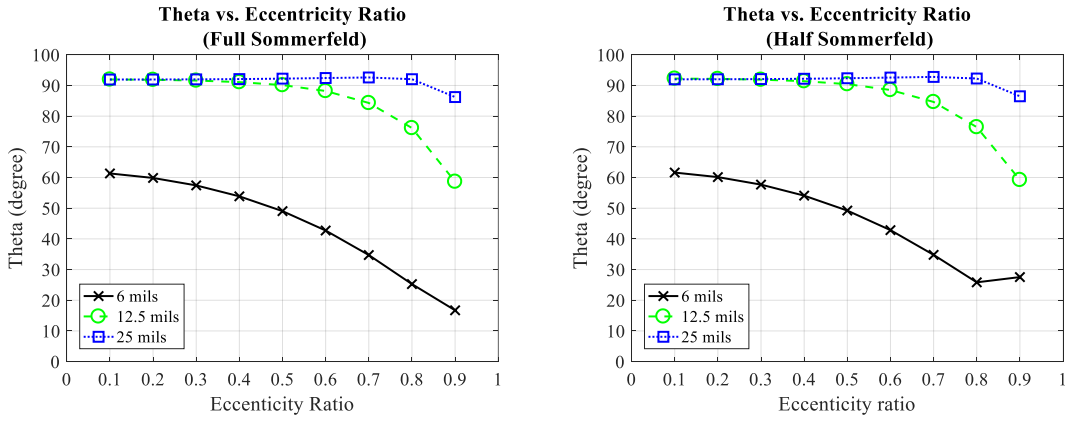

(a) Full Sommerfeld (b) Half Sommerfeld

Figure 4-7 Phase angle vs. eccentricity ratio

The comparison in Figure 4-6 and Figure 4-7 show that:

1) The total forces increase with increases in eccentricity ratio. The growth rate of the 6 mils bearing is larger than that of the other two bearings.

2) The phase difference between the force and the minimum displacement decreases with increases in eccentricity ratio. The attenuation rate of the 6 mils bearing is larger than that of the other two bearings.
3) Since the radial clearance of the 12.5 mils and 25 mils bearing are too large to create the pressure difference between the leading edge and trailing edge, the force with full Sommerfeld and half Sommerfeld are similar. The phase decreasing ratio of the 12.5 mils bearing is larger than that of the 25 mils bearing.
4) In the figure, it seems that the total force generated by the 12.5 mils and 25 mils bearing are same. It is because they are compared with same eccentricity ratio, rather than the same eccentricity.

The comparison between Figure 4-7 and the phase difference between force and the minimum clearance of real experiments in Figure 3-18 shows that:

1) For the 6 mils bearing, the phase difference decreases with increasing in eccentricity ration. The trend of phase changing consistent with the real experimental results shown in Figure 3-18.

4.2 Fluid Structure Interaction Simulation

The quasi-steady simulation of the journal bearing gives the pressure distribution, and the reaction force of the bearing with a certain eccentricity ratio. The bearings play an important role in affecting the system's motion as well as stability. The effects of the rotor should also be considered. The linearized rotor dynamic parameters of fluid film bearings, as shown in Equation (4.3), are generally used in predicting system's dynamic response.

$$\begin{Bmatrix} -F_x(t) \\ -F_y(t) \end{Bmatrix} = \begin{bmatrix} K & k \\ k & K \end{bmatrix} \begin{Bmatrix} x \\ y \end{Bmatrix} + \begin{bmatrix} C & c \\ -c & C \end{bmatrix} \begin{Bmatrix} \dot{x} \\ \dot{y} \end{Bmatrix} + \begin{bmatrix} M & 0 \\ 0 & M \end{bmatrix} \begin{Bmatrix} \ddot{x} \\ \ddot{y} \end{Bmatrix} \tag{4.3}$$

It can simplify the simulation but also results in losing the nonlinear features of the system. To predict the transient response of the rotor-bearing system with nonlinear features, a partitioned fluid structure interaction simulation is conducted. The reaction force of the bearing is calculated in real time by FLUENT based on the rotor's position, spin speed, and whirl speed. In the FSI simulation, the Timoshenko beam model is used to model the shaft of the bearing test rig.

4.2.1 General Finite Element Model

The equation of motion for a rotor-bearing system model is expressed by:

$$\mathbf{M}\ddot{\mathbf{x}} + \mathbf{C}\dot{\mathbf{x}} + \mathbf{K}\mathbf{x} = \mathbf{F}(t) \tag{4.4}$$

where:

$\mathbf{M}$ is the mass matrix;

$\mathbf{C}$ is the entire damping matrix, including gyroscopic effects, and bearing/seal's damping;

$\mathbf{K}$ is the entire stiffness matrix, including element stiffness and the bearing/seal's stiffness;

$\mathbf{x}$ is the generalized coordinates of the rotor in inertial coordinates;

$\mathbf{F}$ is the generalized force.

For the mass matrix, lumped and consistent mass are the generally used in FEM method. Since the geometry of the shaft is simple, the lumped mass matrix is used in this study, with the consideration of improving computational efficiency. It means that the

mass of the node equals to ½(mass of the left element + mass of the right element). The disc gyroscopic effect of an element with 4 degrees of freedom is presented in Equation (4.5), which is a part of the entire damping matrix.

$$C_G = \begin{bmatrix} 0 & 0 & 0 & 0 \\ 0 & 0 & 0 & \omega I_p \\ 0 & 0 & 0 & 0 \\ 0 & -\omega I_p & 0 & 0 \end{bmatrix} \tag{4.5}$$

where:

ω is the spin angular velocity of the rotor;

I_p is the moment of inertia of the element.

The stiffness matrix used in the simulation is obtained by the Timoshenko beam model, which is presented in the following section.

4.2.2 Timoshenko Beam Model

The Timoshenko beam model considers shear deformation and rotational bending effects, resulting in a 4th order equation. It is more effective than the ordinary Euler-Bernoulli beam model since it considers the deformation. The nodal displacements of a 3D Timoshenko beam element in local coordinates are shown in Figure 4-8 [48]. Each element has two nodes with 6 degrees of freedom.

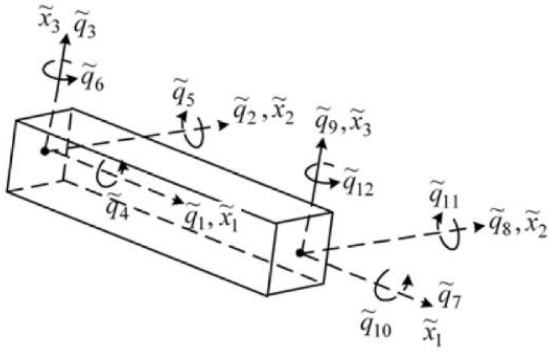

Figure 4-8 Nodal displacements of Timoshenko beam element in local coordinates

where:

$\tilde{x}_1, \tilde{x}_2, \tilde{x}_3$ are the local Cartesian coordinate;

$\tilde{q}_1, \tilde{q}_2, \tilde{q}_3$ are the linear displacement in $\tilde{x}_1, \tilde{x}_2, \tilde{x}_3$ axis of the left node;

$\tilde{q}_4, \tilde{q}_5, \tilde{q}_6$ are the rotational displacement in $\tilde{x}_1, \tilde{x}_2, \tilde{x}_3$ axis of the right node.;

$\tilde{q}_7, \tilde{q}_8, \tilde{q}_9$ are the linear displacement in $\tilde{x}_1, \tilde{x}_2, \tilde{x}_3$ axis of the left node;

$\tilde{q}_{10}, \tilde{q}_{11}, \tilde{q}_{12}$ are the rotational displacement in $\tilde{x}_1, \tilde{x}_2, \tilde{x}_3$ axis of the right node;

The stiffness matric of the 3D Timoshenko beam in the local coordinate is shown in Equation (4.6) [48].

$$\tilde{\mathbf{F}} = \tilde{\mathbf{K}}_e \tilde{\mathbf{q}} \tag{4.6}$$

where:

$$\tilde{\mathbf{F}} = \begin{bmatrix} \tilde{f}_1 \\ \tilde{f}_2 \\ \tilde{f}_3 \\ \tilde{f}_4 \\ \tilde{f}_5 \\ \tilde{f}_6 \\ \tilde{f}_7 \\ \tilde{f}_8 \\ \tilde{f}_9 \\ \tilde{f}_{10} \\ \tilde{f}_{11} \\ \tilde{f}_{12} \end{bmatrix} = \begin{bmatrix} \frac{EA}{L} & & & & & & & & & & & \\ 0 & \frac{12\beta_{12}^a}{L^3} & & & & & & & & & & \\ 0 & 0 & \frac{12\beta_{13}^a}{L^3} & & & & & & & & & \\ 0 & 0 & 0 & \frac{GJ}{L} & & & & & SYM & & & \\ 0 & 0 & \frac{-6\beta_{13}^a}{L^2} & 0 & \frac{\beta_{13}^b}{L} & & & & & & & \\ 0 & \frac{6\beta_{12}^a}{L^2} & 0 & 0 & 0 & \frac{\beta_{12}^b}{L} & & & & & & \\ -\frac{EA}{L} & 0 & 0 & 0 & 0 & 0 & \frac{EA}{L} & & & & & \\ 0 & \frac{-12\beta_{12}^a}{L^3} & 0 & 0 & 0 & \frac{-6\beta_{12}^a}{L^2} & 0 & \frac{12\beta_{12}^a}{L^3} & & & & \\ 0 & 0 & \frac{-12\beta_{13}^a}{L^3} & 0 & \frac{6\beta_{13}^a}{L^2} & 0 & 0 & 0 & \frac{12\beta_{13}^a}{L^3} & & & \\ 0 & 0 & 0 & \frac{-GJ}{L} & 0 & 0 & 0 & 0 & 0 & \frac{GJ}{L} & & \\ 0 & 0 & \frac{-6\beta_{13}^a}{L^2} & 0 & \frac{\beta_{13}^c}{L} & 0 & 0 & 0 & \frac{6\beta_{13}^a}{L^2} & 0 & \frac{\beta_{13}^b}{L} & \\ 0 & \frac{6\beta_{12}^a}{L^2} & 0 & 0 & 0 & \frac{\beta_{12}^c}{L} & 0 & \frac{-6\beta_{12}^a}{L^2} & 0 & 0 & 0 & \frac{\beta_{12}^b}{L} \end{bmatrix} \begin{bmatrix} \tilde{q}_1 \\ \tilde{q}_2 \\ \tilde{q}_3 \\ \tilde{q}_4 \\ \tilde{q}_5 \\ \tilde{q}_6 \\ \tilde{q}_7 \\ \tilde{q}_8 \\ \tilde{q}_9 \\ \tilde{q}_{10} \\ \tilde{q}_{11} \\ \tilde{q}_{12} \end{bmatrix}$$

$$\beta_{12}^a = \frac{EI_{\tilde{x}_3}}{1+\Phi_{12}};\ \beta_{12}^a = \frac{EI_{\tilde{x}_2}}{1+\Phi_{13}};\ \beta_{12}^b = (4+\Phi_{12})\beta_{12}^a;\ \beta_{13}^b = (4+\Phi_{13})\beta_{13}^a$$

$$\beta_{12}^c = (2-\Phi_{12})\beta_{12}^a;\ \beta_{13}^c = (2-\Phi_{13})\beta_{13}^a;\ \Phi_{12} = \frac{24I_{\tilde{x}_3}(1+\nu)}{k_2AL^2};\ \Phi_{12} = \frac{24I_{\tilde{x}_2}(1+\nu)}{k_3AL^2}$$

A is the cross-section area;

E is the modulus of elasticity (Young's modulus);

G is the shear modulus of elasticity;

I is the moment of inertia;

$J$is the polar moment of inertia;

ν is the Poisson's ratio;

L is the length of the element.

For the circular cross-section, $k_2 = k_3 = \frac{6(1+\nu)}{7+6\nu}$, where ν is the Poisson's ratio.

Assume the rotation matrix from global coordinate to local coordinate is $\mathbf{R}$. Thus, $\tilde{\mathbf{F}} = \mathbf{RF}$; $\tilde{\mathbf{q}}_\mathbf{e} = \mathbf{Rq}_\mathbf{e}$ substituting this into Equation (4.6) obtains the stiffness matrix in global coordinate is $\mathbf{K}_\mathbf{e} = \mathbf{R}^\mathbf{T}\tilde{\mathbf{K}}_\mathbf{e}\mathbf{R}$. For small deformation; the rotational angle is small resulting in an identity matrix. In addition, since only the degrees of freedom in x and y direction are considered, the dimension of each node is reduced from 6 to 4 in the following simulations.

4.2.3 FSI Simulation Setup

A Fluid Structure Interaction simulation using MATLAB and ANSYS Fluent is proposed to analyze the rotordynamic behavior of the rotor-bearing system. The rotor-bearing system is modeled in MATLAB using the Timoshenko beam model, while the hydraulic force of the plain journal bearing is calculated by ANSYS Fluent during the simulation. The flow chart for the FSI simulation is shown in Figure 4-9.

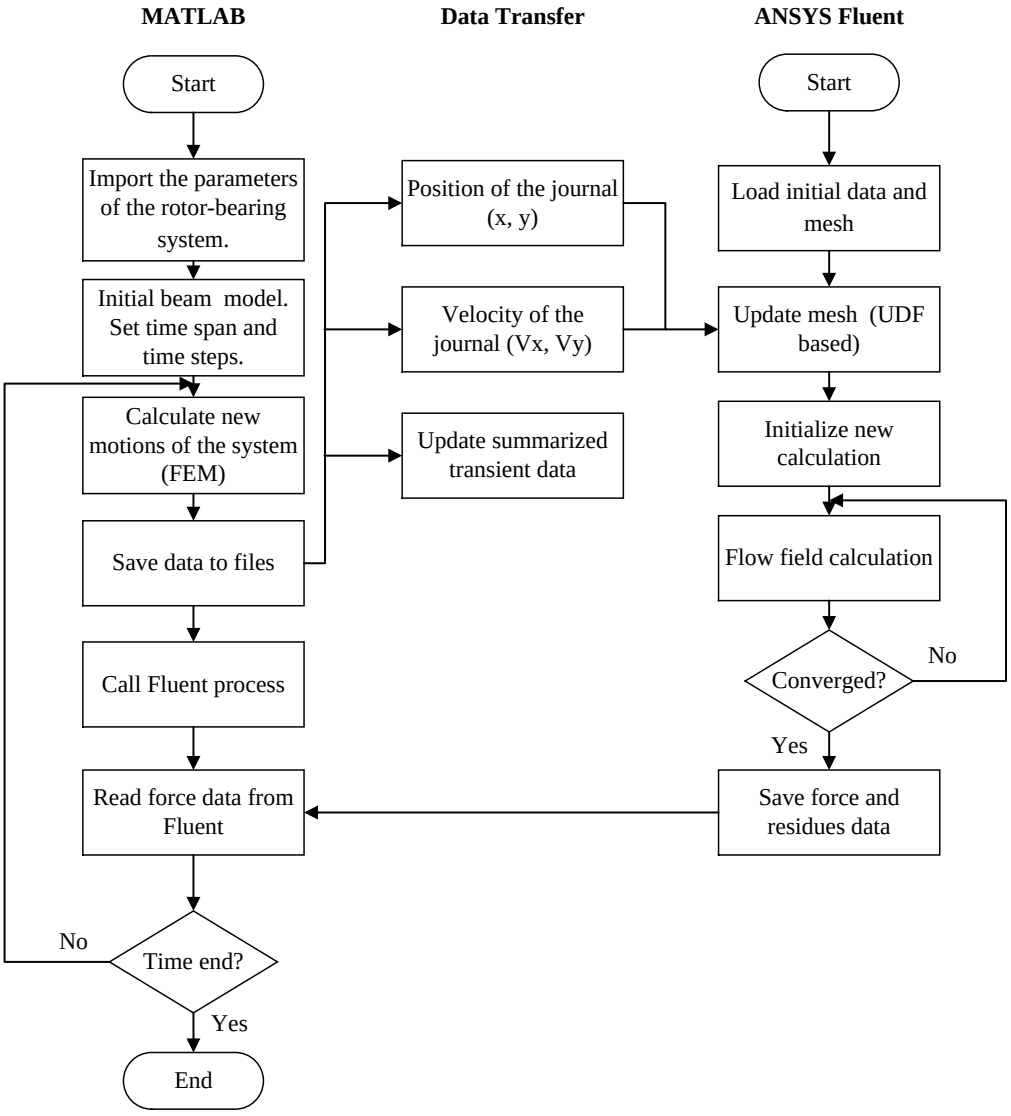

Figure 4-9 Flow chart of the FSI simulation

The FSI simulation consists of three parts: MATLAB beam model, data transfer, and ANSYS Fluent. The MATLAB code firstly imports the rotor length, node division, material parameters, rotordynamic parameters of the bearing to set up the beam model. The force, including the force caused by pressure difference and the shear force, calculated by Fluent is used as the boundary conditions for the nodes of the journal bearing. The new position of the shaft is obtained by integrating the equation of motion. Then, it is saved

and transferred to Fluent for the next calculation. Fluent uses these data to update the new position of the journal as well as the meshes in the flow zone using a User Defined Function (UDF). Then the hydraulic forces generated by the journal bearing in the current time step are obtained. The new forces are saved and transferred back to MATLAB for the next iteration. The entire loop continues until the initialized time steps are reached. Then, the summarized data is saved for post process.

The MATLAB and Fluent based FSI simulation combines the advantages of two commercial software programs, especially the computational capacity of Fluent. It is convenient to update the mesh using the dynamic mesh technique in Fluent as well as conducting multi-phase simulation in future.

4.2.3.1 Model of the rotor

The rotor model is shown in Figure 4-10. The rotor is made of Nickel alloy with a diameter of 1.5'' (0.0381 m). Since the rotor is vertically mounted in the test rig, the effects of gravity are ignored in the simulation.

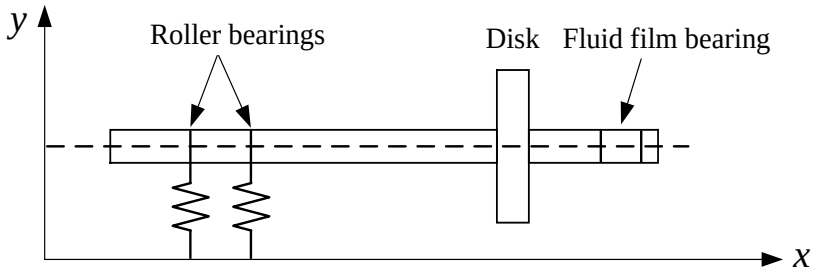

Figure 4-10 Rotor model in the simulation.

The parameters of the rotor's material used in the simulation are presented in Table 4-8.

Table 4-8 Material parameters of the rotor

Temperature (Celsius)	Modulus of Elasticity N/m^2 ()		Poisson's Ratio
	Young's Modulus	Torsional Modulus	
21	2.00E+11	8.00E+10	0.29

Two roller bearings are mounted on the top of the rotor to fix its vertical and radial motion as well as pitch and yaw. The parameters of them are calculated by XLTRC 2 and tuned based upon the measured natural frequency of the rotor bearing system without the fluid film bearing. Their parameters are presented in Table 4-9.

Table 4-9 Rotordynamic parameters of the roller bearing

Speed (RPM)	K_{xx} N/m	K_{yy} N/m	C_{xx} $N \cdot s/m$	C_{yy} $N \cdot s/m$
3600	6.18E+07	6.18E+07	5.25E+02	5.25E+02

The rotor's node data with the node number and length of the element is shown in Table 4-10.

Table 4-10 Node data of the rotor

Node No.	Length (in)	Length (m)	Node No.	Length (in)	Length (m)
1	1.126	0.0286	25-27	1	0.0254
2	1.126	0.0286	28	0.25	0.0064
3-10	0.7185	0.0182	29-65	0.04	0.001
11-22	1	0.0254	66	0.25	0.0064
23	0.675	0.0171	67	1	0.0254
24	0.675	0.0171	68	0	0

The unbalance disk is added in node 24 with a mass of 5.4 Kg, a polar moment of inertial of 0.0225 Kg · m, and a transverse moment of inertial of 0.0117 Kg · m^2. Different imbalance forces are also added to node 24. The stiffness and damping ratio of roller bearings are added on node 5 and 9 respectively.

4.2.3.2 Mesh update UDF

Since the boundary of the rotor changes in each time step, one of the challenge in implementing the FSI simulation is updating the mesh in the flow zone of the bearing. Considering the flow zone in this study is a simple cylinder, a mesh updating method is proposed, which is more efficient than the built-in dynamic mesh methods in Fluent under in this case. The uniform hexahedral mesh is used in the simulation. The target of the mesh updating program is to find the nodes' new coordinates based on their current ones. The diagram of the 2D grid motion is presented in Figure 4-11.

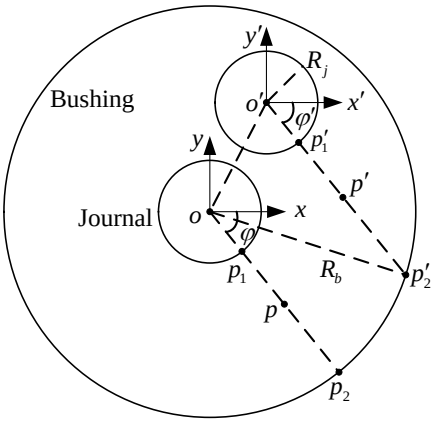

Figure 4-11 Diagram of the 2D grid motion

where:

o is the origin of the bushing. The origins of the bearing and journal are coincident initially;

o' is the origin of the journal;

R_b and R_j are the radius of bushing and journal respectively;

p is the location of a general node of the grid;

p' is the new location of grid p;

p_1 is the intersection between line op and the journal boundary;

p_2 is the intersection between line op and the bushing boundary;

p_1' and p_2' are the new positions of p_1 and p_2 respectively;

φ is the angle between line op and x axis;

φ' is the angle between line op' and x' axis.

In Figure 4-11, the known variables are $\mathbf{oo'}$, $\mathbf{op}$, φ, φ', R_b, and R_j, while the unknown variable is the coordinate of p' in the global coordinate $\left(p_x', p_y'\right)$.

The journal moves from point o to o'. To make sure the relative position between point p' and point o' is same as that between point p and point o, the angle $\varphi' = \varphi$. Since the uniform mesh is used, the ratio of $\left|\mathbf{p_1'p'}\right|$ to $\left|\mathbf{p_1'p_2'}\right|$ is equal to the ratio of $\left|\mathbf{p_1p}\right|$ to $\left|\mathbf{p_1p_2}\right|$. Let

$$\varepsilon = \frac{\left|\mathbf{p_1p}\right|}{\left|\mathbf{p_1p_2}\right|} = \frac{\left|\mathbf{p_1'p'}\right|}{\left|\mathbf{p_1'p_2'}\right|} \tag{4.7}$$

After obtaining ε, the diagram of the calculation triangle to get $\left|o'p_2'\right|$ is presented in Figure 4-12.

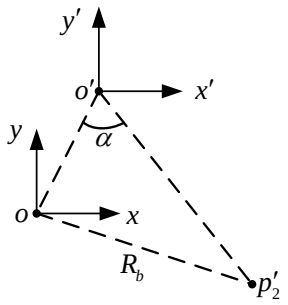

Figure 4-12 Diagram of the calculation triangle

Since $\mathbf{o'p'_2}$ is parallel to $\mathbf{op}$, the angle between $\mathbf{o'o}$ and $\mathbf{o'p'_2}$ can be obtained by the equation:

$$\alpha = \cos^{-1}\left(\frac{\mathbf{o'o}\cdot\mathbf{op}}{|\mathbf{o'o}||\mathbf{op}|}\right), \quad \alpha \in [0,\pi] \tag{4.8}$$

Then, based on the law of cosine:

$$|\mathbf{o'p'_2}| = |\mathbf{o'o}|\cos\alpha + \sqrt{|\mathbf{o'o}|(\cos^2\alpha - 1) + R_b^2} \tag{4.9}$$

The trail solution is discarded since $|\mathbf{o'o}| \le R_b$ and $|\mathbf{o'p'_2}| \ge 0$.

Then the $|\mathbf{o'p'}|$ is obtained by Equation (4.10):

$$|\mathbf{p'_1p'}|_2 = |\mathbf{o'p'_2}| - R_j; |\mathbf{p'_1p'}| = |\mathbf{p'_1p'}|_2 \bullet \varepsilon; |\mathbf{o'p'}| = |\mathbf{p'_1p'}| + R_j \tag{4.10}$$

Since the coordinate of point o' and the angle φ' are known, the coordinate of p' in the global coordinate $\left(p'_x, p'_y\right)$ could be obtained.

4.2.3.3 Boundary conditions

For the CFD conducted by Fluent, the bushing surface is set as a stationary wall. The journal surface is set as a rotating wall, the velocity is calculated based on not only the spin speed, but also the radial velocity of the rotor.

4.2.3.4 Simulation conditions

The FSI simulation was conducted for the 6, 12.5, and 25 mils bearing with different mass imbalances. The simulation conditions for each bearing are shown in Table 4-11, where the √ means the corresponding simulation is conducted.

Table 4-11 FSI simulation conditions

Bearing clearance (mil)	Disk mass imbalance (g-in)		
	2.13	5.32	10.63
6	√	X	√
12.5	√	√	√
25	X	X	√

Since Fluent stops computing when the journal contacts with the bearing boundary, the maximum eccentricity ratio of the journal is set at 0.95. To obtain smooth orbits of the rotor and to assure the convergence of Fluent, the time step for the simulation is set at 0.0001s, resulting in a 2.16 degree of resolution at 3600 RPM.

4.2.4 FSI Simulation Result

The bearing orbits and the corresponding magnitude spectrum of each simulation are shown in Figure 4-13, Figure 4-14, and Figure 4-15. The spectra of each simulation are summarized in Table 4-12.

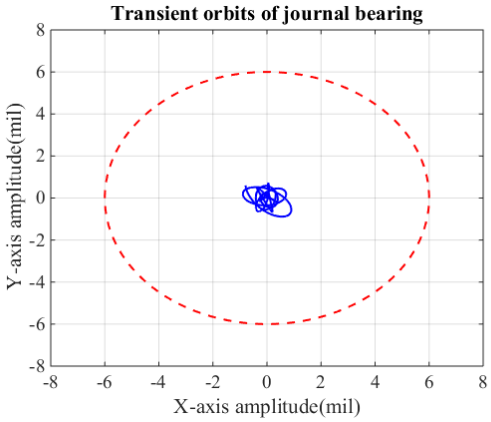

(a) Transient orbits (2.13 g-in)

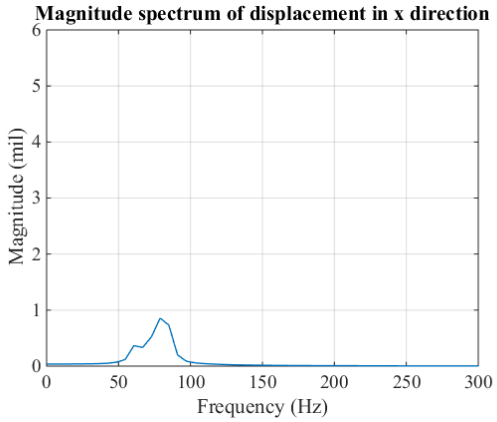

(b) Magnitude spectrum (2.13 g-in)

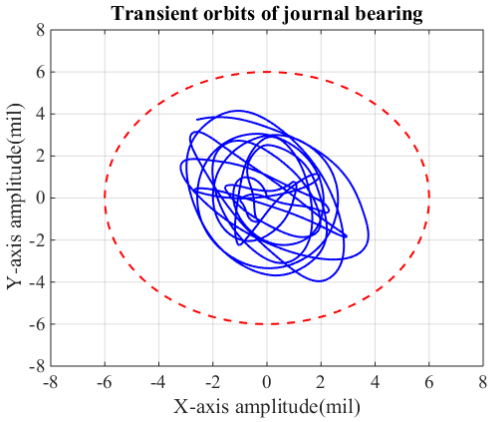

(c) Transient orbits (10.63 g-in)

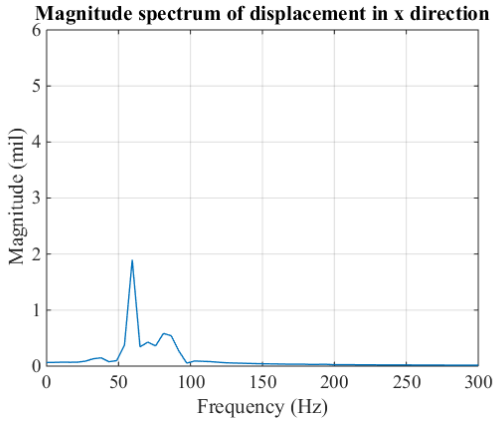

(d) Magnitude spectrum (10.63 g-in)

Figure 4-13 FSI simulation results of 6 mils bearing

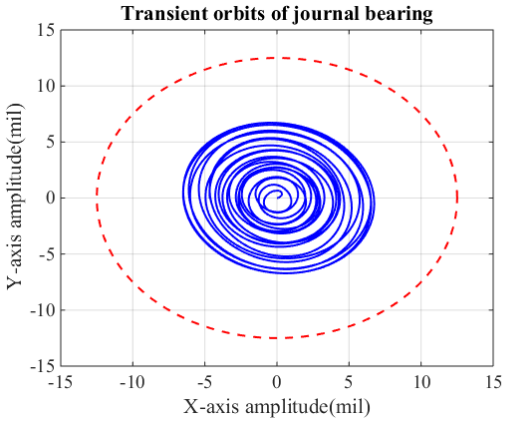

(a) Transient orbits (2.13 g-in)

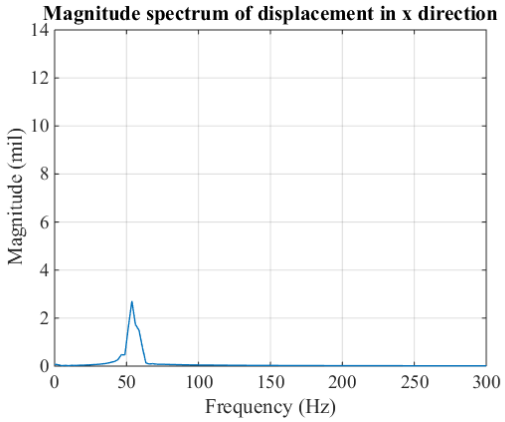

(b) Magnitude spectrum (2.13 g-in)

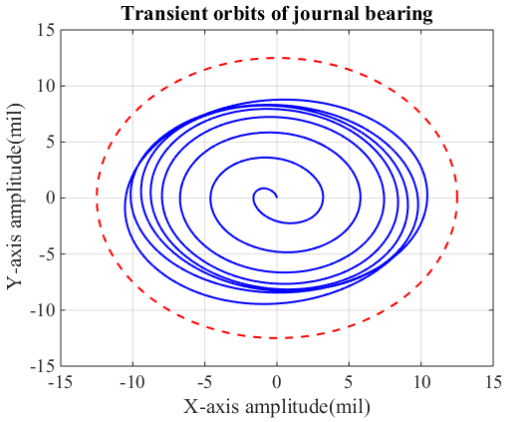

(c) Transient orbits (5.32 g-in)

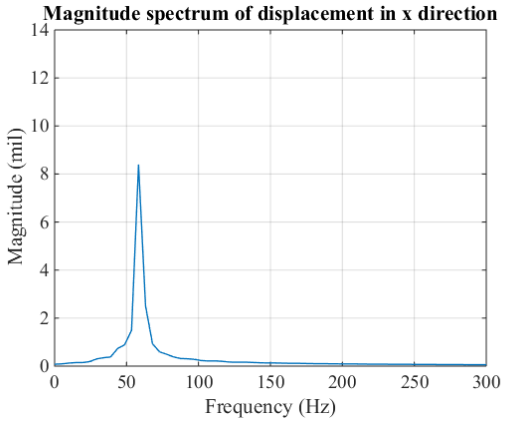

(d) Magnitude spectrum (5.32 g-in)

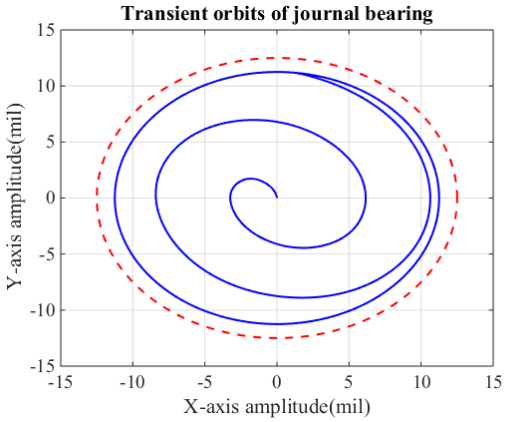

(e) Transient orbits (10.63 g-in)

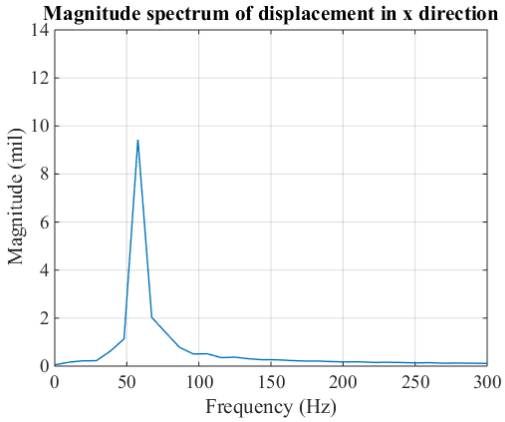

(f) Magnitude spectrum (10.63 g-in)

Figure 4-14 FSI simulation results of 12.5 mils bearing

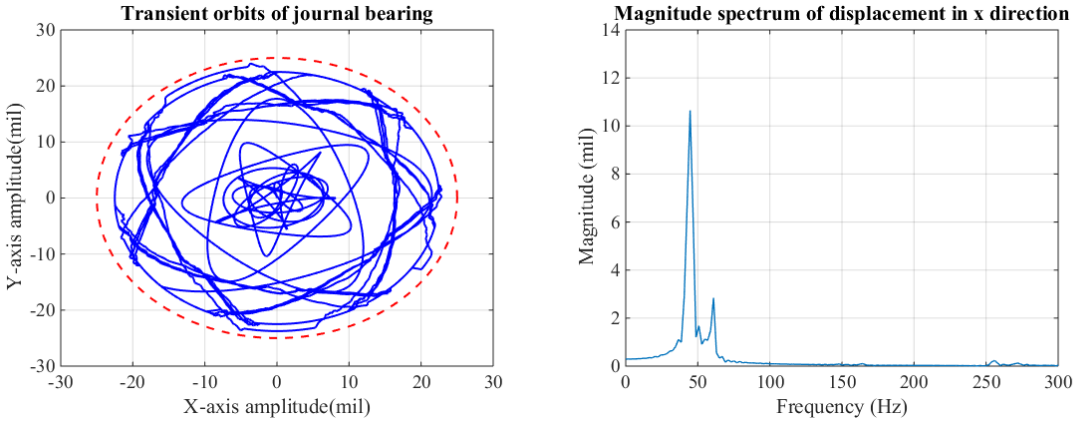

(a) Transient orbits (10.63 g-in) (b) Magnitude spectrum (10.63 g-in)

Figure 4-15 FSI simulation results of 25 mils bearing

Table 4-12 FSI simulation spectral data

Disk mass imbalance (g-in)		Bearing clearance (mil)		
		6	12.5	25
2.13	Frequency (Hz)	NA	53.7	--
	Magnitude (mil)	Too small	2.7	--
5.32	Frequency (Hz)	--	58.3	--
	Magnitude (mil)	--	8.4	--
10.63	Frequency (Hz)	59.5	57.7	44.7; 60.9
	Magnitude (mil)	1.9	9.4	10.7; 2.8

The simulation results show that:

1) For the simulation with 6 mils bearing, the orbits are small (radius=0.8 mils) with 2.13 g-in mass imbalance. The radius of the orbits increases to 4 mils with 10.63 g-in mass imbalance, and the harmonic vibration at 59.5 Hz dominates the spectrum.

2) For the simulation with 12.5 mils bearing, the transit orbit of the bearing is stable with 2.13 g-in mass imbalance at an amplitude of 6 mils (radius). The speed of the journal approaching to the boundary increases with increasing mass imbalance. The spin frequency dominates the vibration as shown in the spectrum. Since the hydraulic force generated by the fluid film bearing increases with increases in eccentricity, the orbit is stable at a certain orbit when the hydraulic force and the mass imbalance force are balanced.
3) For the 25 mils bearing, only the simulation with 10.63 g-in mass imbalance is conducted. The orbits stay in an elliptical locus (backward whirl) resulting in a dominating subharmonic frequency at 44.7 Hz.
4) Generally, the radius of the orbits increases with increasing mass imbalance, which is consistent with the real experimental data shown in Chapter 3. The subharmonic vibration occurs with increasing bearing clearance.

The FSI simulation using Fluent and MATLAB predicts the transient motion of the rotor-bearing system, and the occurrence of subharmonic vibrations. It can be used to analyze the effect of the imbalance force, and the bearing clearance on the dynamic behavior of the rotor-bearing system. It can conduct simulations with multi-phase flow in the bearing clearance. However, the update of the hydraulic force at each time step resulting in a low time efficiency for the simulation. It takes couples of days for a simulation. Since the frequency resolution is proportional to the number of samples, when the spectrum analysis is required, the time consumption of the simulation is not

unacceptable. Thus, an optimized FSI simulation method is proposed, which improves the efficiency significantly.

4.2.5 Optimized FSI Simulation

To improve the calculation efficiency of the FSI simulation, an optimized FSI simulation using a pre-built bearing model and MATLAB code is proposed. The hydraulic force generated by the fluid film bearing is related to journal's eccentricity ratio, spin speed, and the whirl speed. If the whirl effect is ignored, the hydraulic forces are related to the eccentricity ratio and spin speed. The reason of the low time efficiency of the Fluent based method is that the hydraulic forces are calculated at each time step. In the optimized FSI method, the hydraulic forces are calculated by Fluent steady-state simulations with different eccentricities and spin speeds. Then a six-order polynomial equation that represents the forces is obtained by curve fitting. In this way, the bearing model doesn't need to be updated until the bearing's geometry or working conditions are changed. In addition, the interval of the eccentricity when building the bearing model can be set as a relative large value, e.g. eccentric ratio interval = 0.05.

4.2.5.1 Bearing modeling

The hydraulic forces with full Sommerfeld and half Sommerfeld boundary conditions of the bearing with 6, 12.5, 25 mils bearing are calculated based on the quasi-steady CFD simulation method described in section 4.1. The force equation is obtained by curve fitting using a six-order polynomial equation. To evaluate the method of pre-built bearing model, comparisons of the calculated hydraulic forces in x and y directions among

the Fluent-MATLAB-based FSI, the quasi-steady simulation, and the fitted curve are shown in Figure 4-16, Figure 4-17, and Figure 4-18. The quasi-steady forces calculated with Full-Sommerfeld boundary conditions means all the pressure calculated by the quasi-steady simulation is used to obtain the force. While, the Half-Sommerfeld boundary conditions means the negative gauge pressures are forced to be ambient gauge pressure (0) when calculating the force.

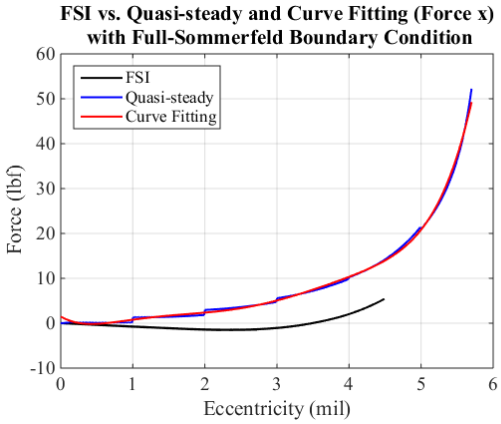

(a) Force in x direction

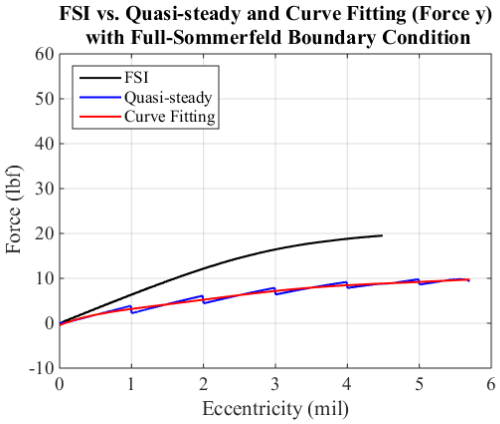

(b) Force in y direction

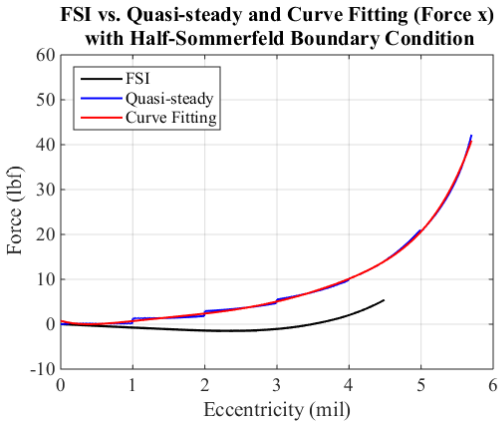

(c) Force in x direction

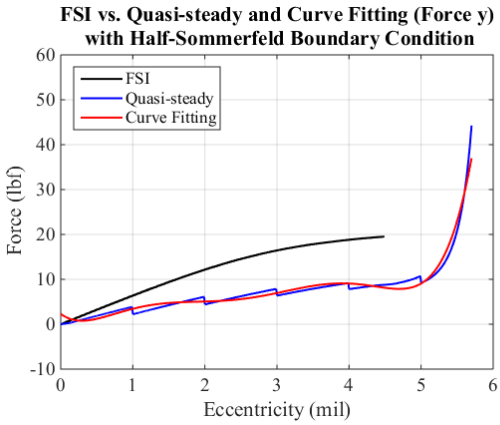

(d) Force in y direction

Figure 4-16 Comparison among FSI, quasi-steady, and fitted curve (6 mils)

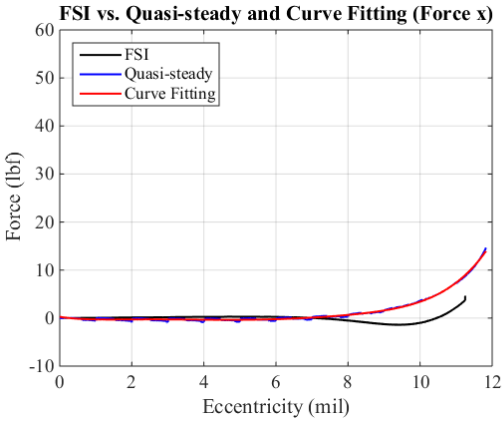

(a) Force in x direction

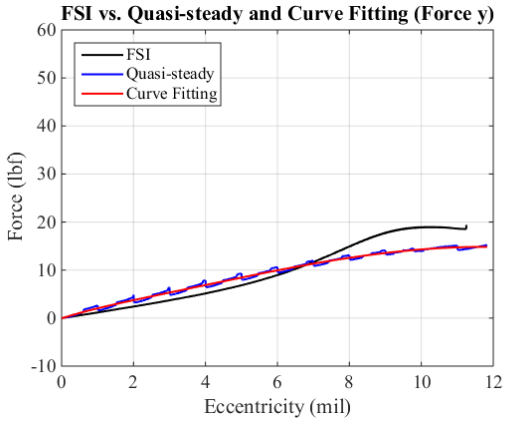

(b) Force in y direction

Figure 4-17 Comparison among FSI, quasi-steady, and fitted curve (12.5 mils)

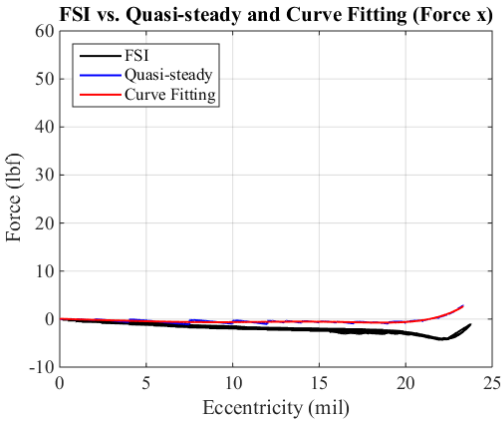

(a) Force in x direction

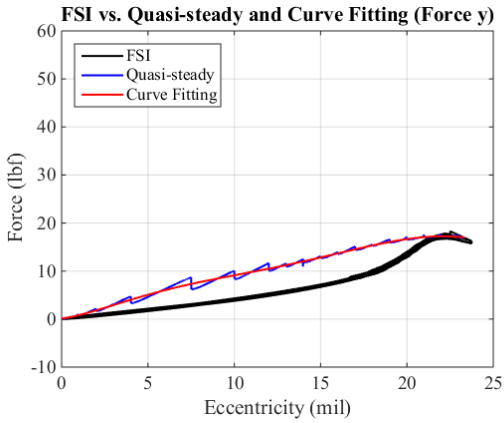

(b) Force in y direction

Figure 4-18 Comparison among FSI, quasi-steady, and fitted curve (25 mils)

In the comparison figures, the black lines are the force obtained by the Fluent-MATLAB based simulation, the blue lines are the quasi-steady simulation results, and the red lines are the force calculated by the force equation. The maximum eccentric ratio of the journal is 0.95 except for the 6 mils bearing, since lacking related FSI data. As shown in Figure and Figure , the low-pressure zone is not obvious for the bearings with 12.5 mils and 25 mils radial clearance, resulting in the small difference between the forces calculated

with Full Sommerfeld and Half Sommerfeld boundary conditions. Thus, only the forces calculated with Full-Sommerfeld boundary condition are shown in the figure.

Figure 4-16, Figure 4-17, and Figure 4-18 show that:

1) The six-order polynomial equation fits the force curve obtained by the quasi-steady simulation well.
2) It shows that the radial velocity of the rotor play a more significant role in the bearing with 6 mils radial clearance than in the other two bearings, which results in a greater relative error between the FSI data and quasi-steady data.
3) The relative error between the force of the old FSI method and that of the quasi-steady simulation is acceptable, especially for the 12.5 mils, and 25 mils bearings.

To make it consistent with the FSI simulation, the forces calculated with Full Sommerfeld boundary conditions are used in the optimized FSI simulation. The time step (0.0001s) and rotor model are same as the FSI simulation, which is shown in Table 4-10.

4.2.5.2 Force conversion

As shown in Section 4.1 and Figure 4-19 (a), the constant eccentricity is set in negative y direction. Figure 4-19 (b) shows a general position of the journal, where force F_x and F_y in global $x-y$ coordinate are required by the optimized FSI simulation. Since f_x and f_y in $x'-y'$ coordinate shown in Figure 4-19 (b) are obtained by the force equation based on the quasi-steady simulation, F_x and F_y could be obtain by Equation (4.11).

$$\begin{aligned} F_x &= f_x \cos\alpha - f_y \sin\alpha \\ F_y &= f_x \sin\alpha + f_y \cos\alpha \end{aligned} \tag{4.11}$$

where α is the angle between x axis and x' axis.

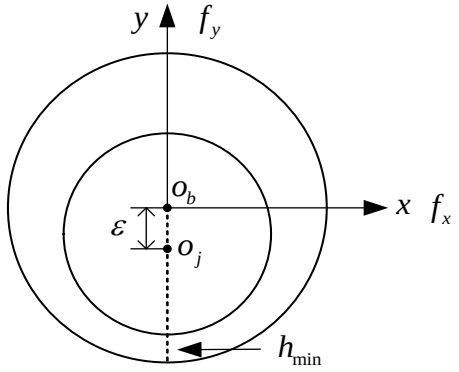

(a) Coordinate in Quasi-steady simulation

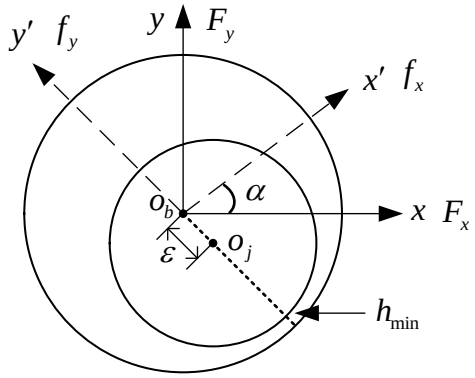

(b) General coordinate in optimized FSI simulation

Figure 4-19 Diagram of force conversation

4.2.6 Optimized FSI Simulation Results

The simulation was conducted on the bearing with 6, 12.5, and 25 mils with 2.13 g-in mass imbalance respectively. For the 12.5mils and 25 mils bearing, additional simulations were conducted with a mass imbalance of 10.63 g-in. The transient orbits and the corresponding magnitude spectra are shown in Figure 4-20, Figure 4-21, and Figure 4-22.

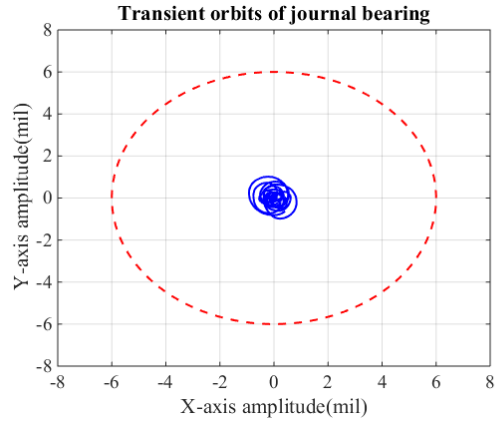

(a) Transient orbits (2.13 g-in)

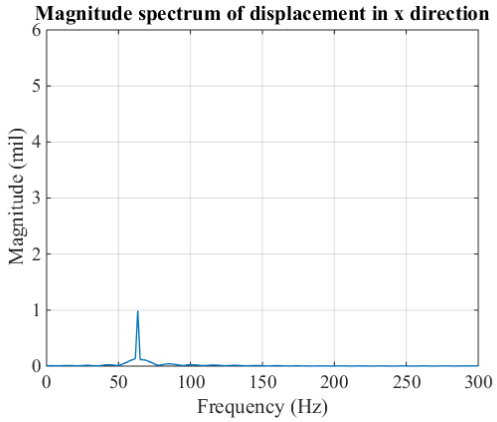

(b) Magnitude spectrum (2.13 g-in)

Figure 4-20 Optimized FSI simulation result of 6 mils bearing

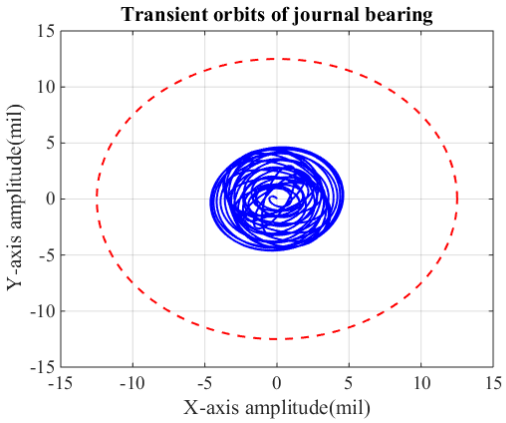

(a) Transient orbits (2.13 g-in)

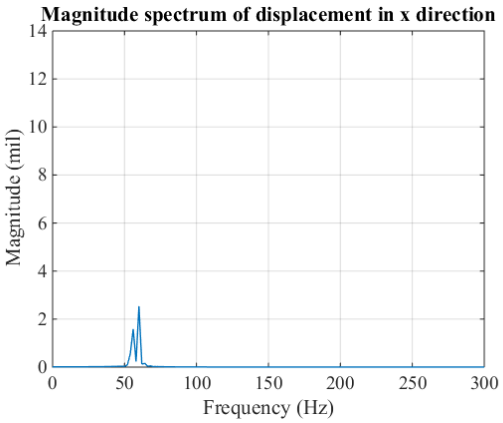

(b) Magnitude spectrum (2.13 g-in)

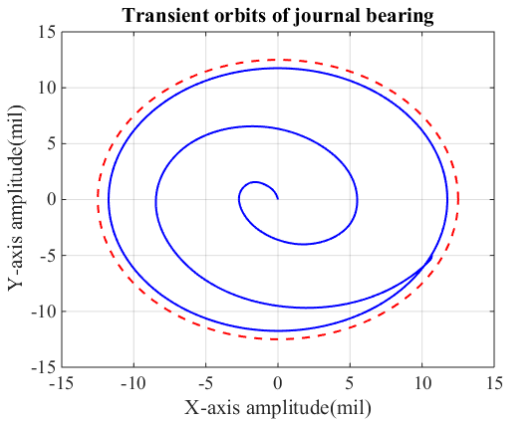

(c) Transient orbits (10.63 g-in)

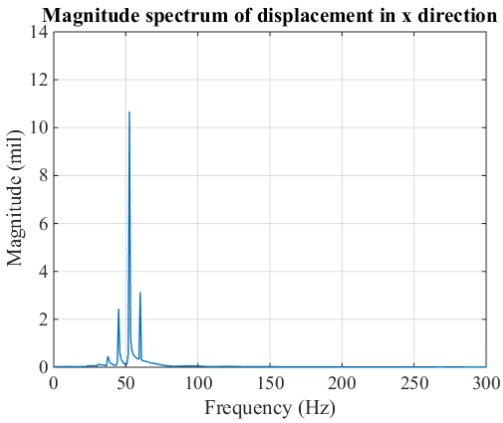

(d) Magnitude spectrum (10.63 g-in)

Figure 4-21 Optimized FSI simulation result of 12.5 mils bearing

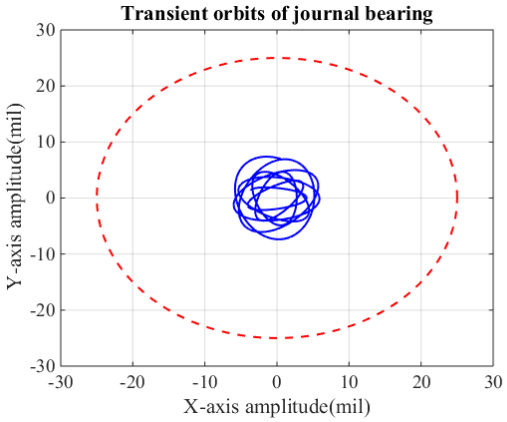

(a) Transient orbits (2.13 g-in)

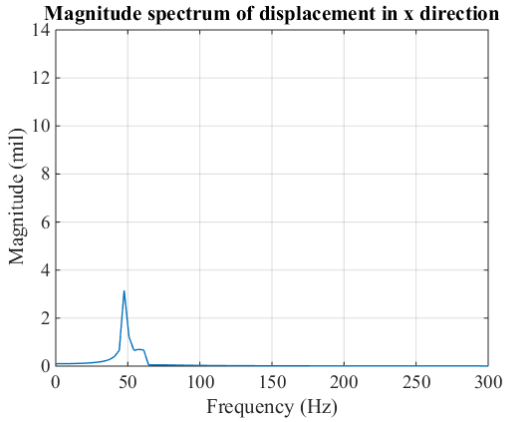

(b) Magnitude spectrum (2.13 g-in)

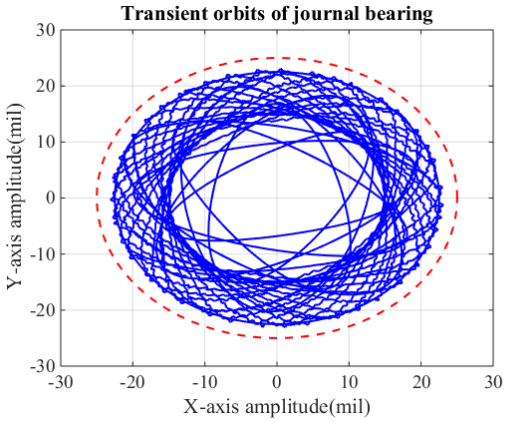

(c) Transient orbits (10.63 g-in)

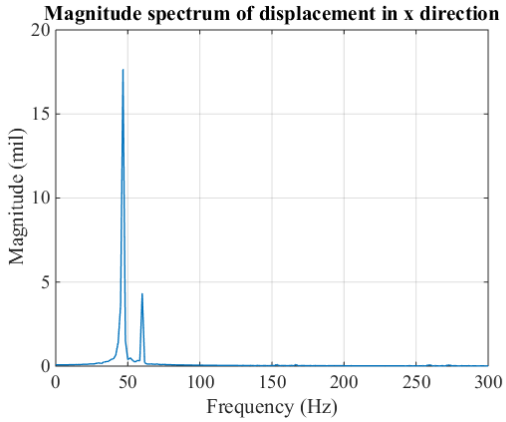

(d) Magnitude spectrum (10.63 g-in)

Figure 4-22 Optimized FSI simulation result of 25 mils bearing

The simulation results show that:

1) For the simulation of 6 mils bearing with 2.13g-in mass imbalance, the transient orbit is small and the 60Hz harmonic component dominates the vibration.

2) For the simulation of 12.5 mils bearing with 2.13g-in mass imbalance, its orbit radius is greater than that of the 6 mils bearings. The subharmonic vibration occurs. For the simulation with 10.63 g-in, the shaft approaches to the

boundary, which is consistent with the FSI simulation result. Subharmonic vibration at 52.5Hz dominates the vibration.

3) For the simulation of 25 mils bearing with 2.13g-in mass imbalance, its orbit radius is greater than that of the 6 mils, and 12.5 mils bearings. The subharmonic component at 47.5Hz dominates the vibration.
4) For the simulation of 25 mils bearing with 10.63 g-in mass imbalance, the subharmonic at around 46.7Hz occurs and dominates the vibration. It is consistent with the FSI simulation result.
5) Generally, the radius of the orbits increases with increases in bearing clearance, when they have the same mass imbalance. It is consistent with the real experimental data shown in Chapter 3. The subharmonic vibration occurs and dominates the vibration with increasing bearing clearance.

Compared with the FSI simulation, the optimized FSI simulation has many advantages. Firstly, it reduces the simulation time significantly. The FSI based Fluent and MATLAB takes couple of days to conduct a 12000 points simulation. But the optimized FSI simulation only takes couple of hours. Secondly, modeling the fluid film bearing takes 80% of the simulation time for the optimized FSI simulation. Once the bearing model is built, it doesn't need to be rebuilt unless the bearing geometry or working conditions are changed. It means that the simulation can be conducted with different rotor models without rebuilding the bearing model. However, for the FSI simulation, the simulation needs to be reconducted even only the rotor model changes, because the hydraulic forces need to be calculated in real time.

5. CONCLUSIONS AND RECOMMENDATIONS

In this study, a vertical bearing/seal test rig is designed and built to test the rotordynamic behavior of bearings/seals in ESP systems based on the erosion experiments of a WJE-100 ESP. The vertical test rig can simulate the motion and erosion of rotating components in the WJE-100 ESP under multi-phase conditions (water, air, and sand). It reduces the time consumption and cost for erosion experiments on the bearings/seals significantly.

Experiments on plain journal bearings with different radial clearances, mass imbalances, and multi-phase flows are conducted using the bearing/seal test rig. The radial clearances of journal bearings are 6 mils, 12.5 mils, and 25 mils respectively, which are chosen based on the erosion experiments of a WJE-100 ESP. The experimental results not only verify the design of the test rig, but also show that:

1) The load capacity of the bearing decreases with increasing bearing clearance.
2) The air breaks the fluid film in the clearance resulting in the load capacity reduction, and increasing in vibration.
3) The effects of imbalance forces, and GVFs on the phase difference changes among the displacement, force, and pressure.

A FSI simulation method based on Fluent and MATLAB is proposed to predict the transient motion of the vertical rotor-bearing system. In the simulation, a grid motion updating method using Fluent UDF is proposed. It reduces the time consumption of updating the gird for the plain journal bearing model, compared with the built-in dynamic mesh method in Fluent. The advantages of the proposed FSI method are as follows:

1) Predict transient motion of the vertical rotor-bearing system in real time.
2) Simulate the sub-harmonic vibrations of the rotor-bearing system.
3) Combine the advantages of the Fluent and MATLAB, which has the capacity to simulate the bearing/seal under multi-phase flow.
4) Verify the design of bearing/seal without conduct real experiments efficiently.

To further improve the calculation efficiency of the FSI simulation, an optimized FSI simulation using pre-built bearing model and MATLAB is proposed. Firstly, the bearing is modeled by a Fluent quasi-steady simulation. The equation of hydraulic forces generated by the bearings are obtained by a six-order polynomial curving fitting. In this way, the bearing model doesn't not need to be rebuilt and the hydraulic forces can be obtained by the equation during the simulation. The time consumption of the FSI simulation is reduced from couple of days to couple of hours. The proposed optimized FSI simulation method also predicts subharmonic vibrations of the vertical rotor-bearing system successfully.

This study provides a direct way to study the bearings/seals in the field of rotordynamics and materials, which is important for the reliability study of ESPs. Meanwhile, the proposed FSI simulation methods predict the transient behaviors of the rotor-bearing system, which provides important reference for the design and modification of bearings/seals.

Future work needs to be done to study the bearings/seals with different geometries under multi-phase flows. The optimized FSI simulation method needs to be improved in accuracy and efficiency further.

REFERENCES

[1] Steve Breit, and Neil Ferrier. "Electric submersible pumps in oil and gas industry." *Pumps & Systems*, Web. 2008.

[2] Brown, Kermit E. "Overview of artificial lift systems." *Journal of Petroleum Technology* 34.10 (1982): 2-384.

[3] "Electrical submersible pumps." *Petrowiki.org.* Web.

[4] Rick Von Flatern. "The Defining Series: Electrical Submersible Pumps." *Oilfield Review, Schlumberger*.

[5] Takács, Gábor. *Electrical submersible pumps manual: design, operations, and maintenance*. Gulf Professional Publishing, 2009.

[6] Stepanoff, A. J. "Centrifugal and axial flow pumps." *John Wiley & Sons*, New York, 1947.

[7] Barrios, Lissett, and Mauricio Gargaglione Prado. "Experimental Visualization of Two-Phase Flow Inside an Electrical Submersible Pump Stage." *Journal of Energy Resources Technology* 133.4 (2011): 042901.

[8] Murakami, Mitsukiyo, and Kiyoshi Minemura. "Effects of Entrained Air on the Performance of a Centrifugal Pump: 1st Report, Performance and Flow Conditions." *Bulletin of JSME* 17.110 (1974): 1047-1055.

[9] Pessoa, Rui, and Mauricio Prado. "Experimental investigation of two-phase flow performance of electrical submersible pump stages." *SPE Annual Technical Conference and Exhibition.* Society of Petroleum Engineers, 2001.

[10] Kirkland, Klayton Edward. *Design and Fabrication of a Vertical Pump Multiphase Flow Loop*. Diss. Texas A&M University, 2012.

[11] Khalid, Y. A., and S. M. Sapuan. "Wear analysis of centrifugal slurry pump impellers." *Industrial Lubrication and Tribology* 59.1 (2007): 18-28.

[12] Sharma, Abhineet Kumar. *Numerical Study of Erosion Wear on a Centrifugal Slurry Pump*. Diss. Thapar University Patiala, 2008.

[13] Roco, M. C., P. Nair, G. R. Addie, and J. Dennis. "Erosion of concentrated slurry in turbulent flow." *ASME FED* 13 (1984): 69-77.

[14] Pagalthivarthi, K. V., et al. "CFD prediction of erosion wear in centrifugal slurry pumps for dilute slurry flows." *The Journal of Computational Multiphase Flows* 3.4 (2011): 225-245.

[15] Gertzos, K. P., et al. "Wear identification in rotor-bearing systems by measurements of dynamic bearing characteristics." *Computers & Structures* 89.1 (2011): 55-66.

[16] Adams, Dan L. "Parameters to Analyze When Determining Abrasive Wear in an Electrical Submersible Pump System." *In SPE Bergen One Day Seminar. Society of Petroleum Engineers*, 2015.

[17] Ligterink, D. J., and A. W. J. De Gee. "Measurement of wear in radial journal bearings." *Tribotest* 3.1 (1996): 45-54.

[18] Papadopoulos, Chris A., Pantelis G. Nikolakopoulos, and George D. Gounaris. "Identification of clearances and stability analysis for a rotor-journal bearing system." *Mechanism and Machine Theory* 43.4 (2008): 411-426.

[19] Wang, Junguo, Jianzhong Zhou, Dawei Dong, Bin Yan, and Chunrong Huang. "Nonlinear dynamic analysis of a rub-impact rotor supported by oil film bearings." *Archive of Applied Mechanics* 83.3 (2013): 413-430.

[20] Yoon, Se Young, Zongli Lin, and Paul E. Allaire. *Control of Surge in Centrifugal Compressors by Active Magnetic Bearings: Theory and Implementation*. Springer Science & Business Media, 2012.

[21] Rankine, W. A. "On the centrifugal force of rotating shafts." *Engineer* 27 (1869): 249.

[22] Dunkerley, Stanley. "On the whirling and vibration of shafts." *Philosophical Transactions of the Royal Society of London*. A 185 (1894): 279-360.

[23] Jeffcott, Henry Hoffman. "XXVII. The lateral vibration of loaded shafts in the neighborhood of a whirling speed-The effect of want of balance." *The London, Edinburgh, and Dublin Philosophical Magazine and Journal of Science* 37.219 (1919): 304-314.

[24] Stodola, Aurel. *Steam and Gas Turbines Vols 1 and 2*. Peter Smith, 1945.

[25] Rankine, W. A. "On the centrifugal force of rotating shafts." *Engineer* 27 (1869): 249.

[26] Newkirk, B. L. "Shaft whipping." *General Electric Review* 27.3 (1924): 169-178.

[27] Hori, Yukio. "A theory of oil whip." *ASME J. Appl. Mech* 26 (1959): 189-198.

[28] Tondl, Aleš. *Some problems of rotor dynamics*. Publishing House of the Czechoslovak Academy of Sciences, 1965.

[29] Ehrich, Fredric F. "Subharmonic vibration of rotors in bearing clearance." *Mechanical Engineering* 88.8 (1966): 345.

[30] Tiwari, Rajiv, and N. Dharmaraju. "Development of a condensation scheme for transverse rotational degrees of freedom elimination in identification of beam crack parameters." *Mechanical Systems and Signal Processing* 20.8 (2006): 2148-2170.

[31] Someya, Tsuneo, et al. *Journal-bearing databook. Ed. Tsuneo Someya*. Springer Science & Business Media, 2013.

[32] Childs, D. W., and Chang-Ho Kim. "Analysis and testing for rotordynamic coefficients of turbulent annular seals with different, directionally-homogeneous surface-roughness treatment for rotor and stator elements." *Journal of Tribology* 107.3 (1985): 296-305.

[33] Childs, Dara W. *Turbomachinery rotordynamics: phenomena, modeling, and analysis*. John Wiley & Sons, 1993.

[34] Eshleman, Ronald L. "Detection, diagnosis and prognosis: An evaluation of current technology." *Current Practices and Trends in Mechanical Failure Prevention*, complied by He & Se Pusey, Vibration Institute, Willowbrook, Illinois (1990): 33-42.

[35] Prohl, M. A. "A general method for calculating critical speeds of flexible rotors." *Journal of Applied Mechanics-Transactions of the ASME* 12.3 (1945): A142-A148.

[36] Myklestad, N. O. "A new method of calculating natural modes of uncoupled bending vibration of airplane wings and other types of beams." *Journal of the Aeronautical Sciences* 11.2 (1944): 153-162.

[37] Taplak, Hamdi, and Mehmet Parlak. "Evaluation of gas turbine rotor dynamic analysis using the finite element method." *Measurement* 45.5 (2012): 1089-1097.

[38] Bungartz, Hans-Joachim, and Michael Schäfer. *Fluid-structure interaction: modelling, simulation, optimisation. Vol. 1.* Springer Science & Business Media, 2006.

[39] Haase, Werner. "Unsteady aerodynamics including fluid/structure interaction." *Air & Space Europe* 3.3 (2001): 83-86.

[40] Grigoriadis, D. G. E., S. C. Kassinos, and E. V. Votyakov. "Immersed boundary method for the MHD flows of liquid metals." *Journal of Computational Physics* 228.3 (2009): 903-920.

[41] Dowell, Earl H., and Kenneth C. Hall. "Modeling of fluid-structure interaction." *Annual Review of Fluid Mechanics* 33.1 (2001): 445-490.

[42] Michler, C., et al. "A monolithic approach to fluid–structure interaction." *Computers & Fluids* 33.5 (2004): 839-848.

[43] Hou, Gene, Jin Wang, and Anita Layton. "Numerical methods for fluid-structure interaction—a review." *Commun. Comput. Phys* 12.2 (2012): 337-377.

[44] Morand, Henri J-P., and Roger Ohayon. *Fluid structure interaction*. John Wiley, 1995.

[45] Shyy, Wei, et al. *Computational fluid dynamics with moving boundaries*. Courier Corporation, 2012.

[46] Khonsari, M. M., and S. H. Wang. "On the fluid-solid interaction in reference to thermoelastohydrodynamic analysis of journal bearings." *Journal of Tribology* 113.2 (1991): 398-404.

[47] Meruane, V., and R. Pascual. "Identification of nonlinear dynamic coefficients in plain journal bearings." *Tribology International* 41.8 (2008): 743-754.

[48] Palazzolo, A., *Vibration Theory and Applications with Finite Elements and Active Vibration Control*. 2016: Wiley.